

LN-39

51760

505340

NASA Contractor Report 187199

# Probabilistic Structural Analysis Methods (PSAM) for Select Space Propulsion Systems Components (5th Annual Report)

*Southwest Research Institute  
San Antonio, Texas*

(NASA-CR-187199) PROBABILISTIC STRUCTURAL  
ANALYSIS METHODS (PSAM) FOR SELECT SPACE  
PROPULSION SYSTEMS COMPONENTS Annual Report  
No. 5, Oct. 1989 (Southwest Research Inst.)  
95 p

N92-12307

Unclassified  
CSCL 20K G3/39 0051760

November 1991

Prepared for  
Lewis Research Center  
Under Contract NAS3-24389

## 1 EXECUTIVE SUMMARY

This report summarizes the overall five-year effort in developing the NESSUS system for Probabilistic Structural Analysis Methods through a collection of code documentation reports for the various NESSUS software modules. Appendix A summarizes Rocketdyne's verification studies in FY'89 involving an HPOT discharge duct.

The team for this past year's effort included the following individuals and organizations:

*SwRI:*

Dr. T.A. Cruse  
Dr. A.F. Fossum  
Dr. Y.-T. Wu  
Dr. S.V. Harren  
Dr. R.C. McClung  
H.R. Millwater  
B.H. Thacker  
J.P. Buckingham

*Consultant:*

J.B. Dias

*Rocketdyne:*

Dr. K.R. Rajagopal  
Dr. A. Debchaudhury  
Dr. D.P. Mondkar  
J. Cunniff

*University of Arizona:* Prof. P.H. Wirsching

## 2 SUMMARY OF DOCUMENTATION INCLUDED IN THIS REPORT

### 2.1 NESSUS/FEM User's Manual

This manual provides detailed instructions on the usage of the NESSUS finite element code. The NESSUS finite element code employs innovative finite element technology and solution strategies. It is the purpose of this manual to acquaint the user with some of the fundamental notions and basic background material needed to effectively use this code and to provide a detailed summary.

### 2.2 NESSUS/PRE User's Manual

This manual provides detailed instructions on the usage of the NESSUS random field pre-processor. This program may be used to perform many of the data manipulations needed to express the uncertainties in a random field as a set of *uncorrelated* random variables. The resulting random variables may be input as Level 2 perturbation variables into the NESSUS finite element code, and used as the primitive variables for the fast probability integration program.

## **2.3 NESSUS/Level 1 User's Manual**

This manual provides detailed instructions on the usage of the NESSUS Level 1 post-processor. The Level 1 strategy is based on the simplifying assumption that the uncertainties in the problem can be adequately modeled as a set of *global scalings* of the applied force, stiffness, mass and damping matrices. The Level 1 post-processor may sometimes be used to estimate the effects of these uncertainties by performing a series of very simple post-processing operations.

## **2.4 FPI User's Manual**

This manual provides detailed instructions on the usage of the NESSUS Fast Probability Integration module. Fast Probability Integration is an approximate technique to compute the cumulative distribution function. This technique is very computationally efficient and provides information about the probabilistic sensitivity of the random variables.

## **2.5 FPI Theoretical Manual**

This manual provides an overview of the theoretical background of the NESSUS Fast Probability Integration module. The theoretical algorithms and concepts on which FPI are based are discussed in detail.

## **2.6 NESSUS/EXPERT User's Manual**

This manual provides detailed instructions on the usage and installation of the NESSUS expert system code. A sample runtime session is provided.

## **2.7 NESSUS/EXPERT System Manual**

This manual provides detailed instructions on the expert system code format and structure.

## **APPENDIX A**

---

### **Uncertain Random Vibration Analysis of HPOT Discharge Duct**

**Dr. K.R. Rajagopal**  
**Dr. Amit Debchaudhury**  
**Mr. John Cunniff**  
**Dr. D.P. Mondkar**  
**Rocketdyne Division**  
**Rockwell International Corporation**

# 1. UNCERTAIN RANDOM VIBRATION ANALYSIS OF HPOT DISCHARGE DUCT

## 1.1.1 Introduction

The NESSUS verification studies in FY'89 for the dynamic analysis of linear systems, were restricted to conventional random vibration and harmonic analysis. That is, the PSD's of random excitation or amplitudes and frequencies of harmonic excitation were treated as deterministic. In reality, however, the amplitude and frequencies (1N, 2N, 3N, 4N etc., where N is the shaft speed) of the harmonic excitation change as the power level changes within the same test (duty cycle effect). Changes are also observed from one test to the next for the same engine and same power level, and mostly from one engine to another. Similar uncertainties are also associated with the parameters of random excitation. In general, the PSD of random base excitation (which itself is a random process) can be modelled as a random process defining the uncertainties associated with the shape and power of the excitation. This will, however, make the problem very complex. Instead, that random process can be modelled by a sequence of random variables each representing the power contained in a small frequency band over a time period for which the process remains stationary (i.e., power level or the inlet conditions do not change). In general those random variables will be highly correlated. At present no statistics are available for such random variables, even though the data base is available to produce such statistics. In the present studies, only the uncertainties associated with the total power of excitation are considered and the spectral shapes are assumed to be deterministic. In the future, once such statistics are available, it will be interesting to investigate the effect of uncertainties associated with the spectral shapes as well.

## 1.1.2 Duct Finite Element Model Details

A NESSUS model of a high pressure oxidizer turbopump discharge duct was generated in FY'89. The model, as shown in Figure 1.1.1, was generated using the two-noded linear isoparametric beam element (Type 98) available in NESSUS. Figure 1.1.2 is another visual representation of the same duct showing the duct radius, flange radius and the valve attachment sizes. The statistics of the finite element model and typical features were presented in the PSAM 4th Annual Report.

The duct is supported at three points, two of them on the high pressure oxidizer pump and the third one on the main injector dome. The model was analyzed using the constrained penalty mass approach. The natural frequencies are presented in Table 1.1.1. Only the first twenty modes were included for the dynamic analysis of the duct. The details of the modal analysis of the duct were presented in the 4th annual report.

## 1.1.3 NESSUS Capabilities for Uncertain Random and Harmonic Analysis

The NESSUS code has the capability of handling the variations in harmonic frequencies, amplitude and phase angles.

For uncertain random excitation, a general variation in PSD (both power and shape) is available in NESSUS. The shape variation, however, will require a set of partially correlated random variables defining the power contained in disjoined frequency bands. In the present analysis, only the total power is considered as a random variable.

Among system parameters, variations in beam cross-sectional properties and material properties can be handled in a consistent manner. However, the only system parameter that is considered uncertain in the present analysis is the modal damping.

#### 1.1.4 Random Variables Considered in the Analysis

The duct model is subjected to excitation at multiple support points, some uncorrelated and some fully correlated. The excitations are considered fully correlated when identical PSD's are specified for the same translational direction at different support points. The envelope PSD's for the pump and the injector dome environment are presented in Figures 1.1.3a through 1.1.3e. It should be noted at this point that these figures represent envelope PSD's and not average PSD's. At present, average spectral shapes are not available. Statistics are available only for the total power of excitation (i.e., area under the PSD curves). Consequently, the envelope PSD's are scaled down to represent the average spectral shapes. The basic random variables considered in the present probabilistic analysis, representing the uncertainties of excitation parameters, are the six mean square base accelerations, the two pump speeds and the amplitudes of the harmonics. Modal damping is the only system parameter that is considered uncertain in the present analysis. A brief description and various statistics of all the random variables considered are presented in Table 1.1.2.

#### 1.1.5 Load Variations Modelling Strategies

The load modelling strategies came primarily from the composite load spectra contract work. The statistical data for pump speeds were obtained from the engine models and the uncertainties in PSD and sinusoidal amplitude were obtained from test data.

The frequencies of harmonic excitation are related to the pump speeds - the high pressure oxidizer turbopump and the high pressure fuel turbopump, that are considered as the two basic random variables. The change in shaft speed affects all harmonics (synchronous and its multiples e.g., 1N, 2N, 3N, & 4N). There is a deterministic change in the amplitude of all harmonics which vary with the change in speed (e.g., speed 2).

In addition to this deterministic part of speed dependent variation, there is a component to component variation observed for all harmonic amplitudes. That amplitude variation for each frequency (1N, 2N,...etc.) is treated as an independent random variable. These two types of variations for harmonic loads is illustrated in Figure 1.1.4a-b.

The six mean square base accelerations (area under PSD curves) at the two support environment are treated as six independent random variables. The statistics presented in Table 1.1.2 include component to component variation as well as the duty cycle effect.

#### 1.1.6 Posing the Problem to NESSUS

In the present form 'NESSUS' cannot conveniently handle a single random variable that affects more than one spectral case. This problem, however, can be overcome by defining pseudo-random variables having the same statistics as the original random variables and perturbing all of them simultaneously in 'NESSUS' and ignoring those pseudo-random variables in FPI evaluations. In the present, studies there are only 38 true random variables, but 27 additional pseudo-random variables needed to be defined to model the load properly.

### 1.1.7 Number of Spectral Cases

The probabilistic analysis procedure used in this study made use of the mean value first order method as well as advanced mean-value-first-order-method implemented in NESSUS/FPI. For the first-order reliability method, a total of 1330 perturbed spectral solutions had to be evaluated, of which only a small subset were unique and needed to be recalculated. This is true because some spectral cases are not at all affected by the perturbation and some others can be obtained by simple linear scaling. In the present analysis only 99 separate cases need to be computed and saved. An additional 35 cases can be obtained by linear scaling and the rest need only pointers. Based on the recommendation made after this study, NESSUS now has better built-in intelligence to avoid some superfluous calculations or storage of perturbation data involving spectral cases.

### 1.1.8 NESSUS-POST Enhancements: Spectral Combinations

For the final probabilistic response calculation, all spectral cases need to be combined to get one single response for each perturbation. The combination rules are not unique, but in general there are only a finite number of acceptable combination rules to determine the peak value of response or to determine the R.M.S value of response.

The load combination values are obtained using a code 'NESSUS POST' written at Rocketdyne. The results reported in this study used a combination of manual effort and "NESSUS POST" routines to create the FPI deck.

### 1.1.9 NESSUS/FPI Results

The FPI results are obtained for a typical node (Node #265) as shown in Figure 1.1.1. Only the stress resultants (not stress components) are available in 'NESSUS' for beam type elements. The complete CDF and the statistics of the responses at the typical node are obtained using the mean value first order (MVFO) method as implemented in NESSUS/FPI. They are presented in Table 1.1.3. The PDF and the CDF for the response  $M_y$ , using 20 probability levels are presented in Figures 1.1.5a - b respectively, where  $M_y$  is the bending moment in the y direction.

The sensitivity factors for the first four dominant random variables on the response  $M_y$  at node 265 are presented in Figures 1.1.6a-b. It shows that the sensitivity of various random variables varies along the CDF.

Qualitatively speaking, at the lower tail end of the CDF, the random variable 'damping' is more important than the PSD of excitation. At the upper tail end, the PSD becomes the dominant random variable.

A few points are computed and plotted on the CDF curve (Figure 1.1.5b) using the advanced mean-value-first-order method obtained using the 'MOVE' option (AMVFO). It can be observed that at the upper tail end, where PSD power level dominates, that has linear effect on the mean square response, the MVFO and AMVFO give almost the same value. The two approaches differ significantly at the lower tail where damping is more important and has nonlinear effect on the mean square response. Table 1.1.4 shows the computational statistics for the probabilistic analysis of the HPOTP discharge duct.

### 1.1.10 Summary Remarks

This verification study demonstrated the use of the NESSUS/FEM/FPI code in conducting conventional as well as uncertain random vibration and harmonic analysis. The methodology used here considering systematically the variation has very good potential for comparing well with the experimental data. The results from the NESSUS code could have been compared with experimental data if strain output from the finite element model in the form of PSD were available. It must be mentioned that the results from conventional random vibration analysis using peak power on shape is generally over conservative and does not compare well with experimental data.

## **1.2 Probabilistic Material Nonlinear Analysis: Verification Of The Lox Post**

### 1.2.1 Introduction

A liquid-oxygen (LOX) post of a space propulsion system on the outside edge of the main combustion chamber near the interpropellant plate was considered for this NESSUS verification analysis. The LOX post and the axisymmetric finite element model studied are shown in Figure 1.2.1. The LOX post controls the mixing of the cold (-195/ R) liquid oxygen with the hot (1500/ R) hydrogen-rich steam. Hot hydrogen-rich steam impinges on the outer surface of the post while the cold liquid oxygen flows through the inside of the post from the LOX dome in the injector before being mixed with the hydrogen-rich steam in the combustion chamber. Figure 1.2.1 details the local axisymmetric finite element model of the nickel-based-superalloy (Inconel 718) interpropellant plate and the cobalt-based (Haynes 188) post, joined by an inertia weld, used in this analysis. The model consists of 237 nodes and 194 four-node assumed-strain axisymmetric (NESSUS type 153) elements. The model is constrained from rigid-body motion along the axial direction at one node (node 1) in Figure 1.2.1.

### 1.2.2 Scope of the Probabilistic Material Nonlinear Analysis

The probabilistic material nonlinear analysis considered, as random variables, yield stress of the material, and the following eight variables, influencing the temperature distribution on the post:

1. Hot-gas temperature
2. Coolant temperature
3. Hot-gas flowrate
4. Coolant flowrate
5. Mixture ratio
6. Heat-shield-gap factor
7. Hot-gas heat-transfer film coefficient
8. Coolant heat-transfer film coefficient

Table 1.2.1 summarizes statistics of these eight component-level random variables influencing the temperature distribution of the post. The objective of this analysis was to generate a probability distribution on the response variable: effective strain range, which is important in designs which consider low-cycle fatigue.

This analysis models both isotropic materials with temperature-dependent material properties (using user-subroutine UTEMP) and bilinear kinematic-hardening (using user-subroutine WKSLP). The material properties for Inconel 718 and Haynes 188 are shown in Table 1.2.2, and the temperature-dependent stress-strain curves are shown in Figures 1.2.2 and 1.2.3, respectively.

Variability in yield stress of the materials was considered in the interests of investigating its influence on the hysteresis loop of the stress-strain response generated by the engine start-up, steady-state, and cutoff phases during the duty cycle of the engine. An estimate of the variability of the yield stress of Inconel 718 was obtained from limited test data and confirmed by expert opinion. Since the load caused by temperature is a major driver of the effective strain range, identifying sensitivity of the response to each random variable influencing temperature is of interest. The Composite Load Spectra (CLS) program provided the changes in the load caused by temperature due to variations in the eight component-level random variables influencing the temperature distribution on the post. The CLS program supplied a correlation field, used to perform perturbation analysis in the NESSUS code, for the nodes of the finite element model of the LOX post (Figure 1.2.1). Marginal distributions were used to assess the influence of each of the eight random variables. Correlations among the eight component-level random variables is considered weak; however, correlation among different nodal locations on the LOX post is perfectly correlated for each given random variable.

Of the eight random variables influencing temperature, hot-gas temperature, hot-gas flowrate, coolant flowrate, and the mixture ratio, all vary throughout the duty cycle of the engine, as demonstrated in Figure 1.2.4. The four random variables are scaled from their values at steady state over the deterministic temperature profile. The perturbed temperature profiles of the transient are linearly scaled from the deterministic temperature profile of the transient. Experimental data support such an approach; also, the engine parameters are closely controlled by the computer controller of the engine.

### 1.2.3 Verification of the Work-Hardening Algorithm

During engine firing, both the Inconel 718 and the Haynes 188 materials in the LOX post experience plastic deformation. User-subroutine WKSLP models the slope of the stress-strain curve beyond the yield point of the material. Initial tests of this user-subroutine revealed limitations for the case of reverse yielding of multilinear (beyond bilinear) models. Reverse yielding does occur in the LOX post during the cutoff phase of the duty cycle of the engine.

A single four-node plane-stress element was used to test the WKSLP user-subroutine (see Figure 1.2.5). The axial stress-strain response for a multilinear kinematic-hardening model is shown in Figure 1.2.6. The four-node element was incrementally stretched and contracted at room temperature as shown in the figure. As can be seen from the stress-strain response, the hardening model employed in NESSUS recalls only the last slope of the stress-strain curve encountered. Note how Slopes 1 and 2 are lost under reverse yielding and during subsequent reloading. Since such model behavior is not generally accepted, the material model employed in the verification analysis of the LOX post was a bilinear temperature-dependent stress-strain model.

The four-node plane-stress element was also tested for temperature changes under a constant mechanical load using a temperature-dependent, bilinear kinematic-hardening model. The two examples shown in Figure 1.2.7 demonstrate acceptable performance of the material model employed in NESSUS.

#### 1.2.4 Deterministic Analysis

As an initial check, NESSUS (version 3.5) elastic-response results were compared with APSA, a Rocketdyne in-house finite element code, and PAAM results for the temperature loading condition at steady-state. Figure 1.2.8 shows the temperature distribution of the LOX post at steady-state. The results from the mixed-iterative algorithm employed in NESSUS for the axial, hoop, radial, and effective stresses are shown in Figures 1.2.9 through 1.2.12. The NESSUS mixed-iterative and displacement-based solution algorithms are compared with APSA and PAAM results in Figures 1.2.13 through 1.2.15 for the axial, hoop, and radial stresses, respectively, along the cross-section between nodes 78 and 84 (Figure 1.2.1), and similarly for the cross section between nodes 117 and 122 (Figure 1.2.1) in Figures 1.2.16 through 1.2.18. Considering the differences in analytical approximations between the mixed-iterative and displacement-based solution algorithms employed in NESSUS, and the displacement-based solution algorithm employed in APSA, the results are in reasonable agreement. Nevertheless, note the large radial stresses on the inner surface of the LOX post from the NESSUS mixed-iterative algorithm which violate equilibrium. Large tolerances in the maximum allowable error in the residuals were required for the NESSUS mixed-iterative solution.

In general, the largest refinements in equilibrium of stresses among elements are achieved in the first few iterations, as can be seen in Figure 1.2.19. The mixed-iterative results discussed for these two cross sections were taken from the sixth iteration.

The LOX post model was exercised for the deterministic duty cycle of the engine before the perturbation analysis on the random variables. A bilinear kinematic-hardening material model was programmed into the WKS LP user-subroutine. An incorrect stress-strain curve was chosen for Inconel 718 at this stage in the analysis: electron-beam-welded Inconel 718, shown in Figure 1.2.20. A correct stress-strain curve for Inconel 718 (as shown in Figure 1.2.2) was used during the probabilistic analysis described in the next section. Temperatures during the start-up, steady-state, and cutoff phases of the duty cycle of the engine are shown for four nodes in Figure 1.2.21. For the purposes of this analysis, durations of time the engine spent at any given state (i.e., durations of time the LOX post experienced any given temperature state) of 500 seconds or more were compressed into a time span of 1 second, which here corresponds to one time step. Temperatures on the LOX post ranged from about 200/ to 1600/ Rankine. Time is a dummy parameter in the transient structural analysis; however, time plays a role in the heat-transfer analysis which supplied the temperature distribution of the post.

The mixed-iterative solution method is required when using the work-hardening user-subroutine WKS LP. For the large temperature gradient across the coarse mesh of the LOX post, the mixed-iterative solution generates large maximum errors in the residuals. The reduction in the maximum error in the residuals for increasing iterations on the solution is shown in Figure 1.2.22 for three increments of the temperature load. Little improvement in the accuracy of the

solution is gained after 10 to 20 iterations. In the analysis of the LOX post, the limit on the maximum error in the residuals was set at 500 lbs., i.e., the mixed-iterative algorithm will iterate until the maximum error in the residuals falls below this limit.

The stress-strain hysteresis loops of the effective and axial components for four nodes of the LOX post subjected to six duty cycles of the engine are shown in Figures 1.2.23 through 1.2.30. A small ratcheting effect, i.e., translational drift of the hysteresis loop beyond the second duty cycle, decreasing with each additional duty cycle, can be observed in the figures. Because of the thermally driven nature of the LOX post problem, and based on past performance of the LOX post, ratcheting of the LOX post is not expected. Nevertheless, the effective strain range generated from NESSUS does satisfactorily stabilize after the second duty cycle. Thus, for the probabilistic analysis considering material and temperature variability, simulations of two duty cycles of the engine prove sufficient. Ratcheting was not observed in a LOX post analysis over six duty cycles conducted using the APSA code, as can be seen in Figure 1.2.31.

### 1.2.5 Probabilistic Analysis

In the probabilistic analysis of the LOX post, engine-to-engine variation is modeled, neglecting possible mission-to-mission variation. Measurements indicate engine-to-engine variation to be of more concern than mission-to-mission variation. Thus, the perturbation analysis of the random variables here simulates engine-to-engine variation by perturbing a random variable and rerunning the load simulation of two duty cycles of the engine.

Variation in the yield stress of the Inconel 718 material was initially studied. Analysis of test data of the yield stress of Inconel 718 showed a 5 percent coefficient of variation at room temperature. The coefficients of variation of the yield stresses at other temperatures were assumed to be the same as at room temperature. The temperature loading over two duty cycles was run for +1, -1, +2, and -2 standard-deviation changes in yield stress of Inconel 718. The response variable of interest, the effective strain range, was computed from the effective strain of differences in the Cartesian strain components between the first and steady-state load steps during the second duty cycle, identified as A and B, respectively, in Figure 1.2.32. The negligible effect of variability of the yield stress on effective strain range is shown for four nodes in Figures 1.2.33 and 1.2.34. The thermally driven nature of the model of the LOX post employed here, analogous to a displacement-controlled problem (note: no mechanical loads were considered in this analysis), may explain the observed lack of sensitivity of the effective strain range to changes in yield stress.

Variability in the yield stress of the material was not considered in the study of the temperature variation on the LOX post because of its negligible influence on the effective strain range. The eight independent component-level random variables influencing the LOX post temperature distribution (Table 1.2.1) were studied in detail, separate from the perturbation analysis which considered variability in the yield stress of the material. Each of the eight random variables were perturbed separately, and the sensitivity was assessed of the response of the effective strain range to individual random variables. Also, the cumulative density function (CDF) of the response variable was calculated for several critically stressed nodes (see Figure 1.2.1). The CDF's of the response were obtained by fitting both linear and quadratic curves to the response function, and using both the fast-probability-integration and the Monte Carlo

methods in the probability calculation. Common to all of these methods was the construction of an approximate response function using results, which were considered valid for the entire range of the response, from the perturbation analysis of the finite element model.

Several perturbations of the finite element model were conducted: +1, -1, +2, -2 standard-deviation perturbations of the eight random variables, one at a time. Mixed terms, i.e., combined random-variable perturbations, were not considered in the construction of the approximate response function. Thus, 32 solutions from the finite element model were obtained. Note that each solution from the finite element model was calculated from an incremental nonlinear analysis involving 34 load steps, or two duty cycles of the engine. In preliminary deterministic analyses of the model, two duty cycles proved sufficient to obtain a stable effective strain range.

The UPERT user-subroutine, installed in NESSUS version 4.0, was used to perform the perturbations of the random variables. The sensitivity of the random variables to nodal temperatures changed from increment to increment. The UPERT user-subroutine read in the temperature sensitivity factors for each random variable during each load increment from a file separate from the NESSUS computer program.

Two types of response functions were constructed from the 32 solutions from the finite element model: linear and quadratic with no mixed terms. The polynomial coefficients were determined using an IMSL least-squares algorithm separate from the NESSUS code. Once the coefficients were determined, the approximate response function was coded into the FPI user-function. The CDF's of the response variable were obtained using the first-order reliability and Monte Carlo methods in the FPI code. Figure 1.2.35 compares one CDF of the response variable from one node (node 56) for three solution methods: first-order-reliability solution with a linear response surface, a Monte Carlo solution with a linear response surface, and a Monte Carlo solution with a quadratic surface. The similarity in the CDF's of the response variable calculated from the linear and quadratic response surfaces indicates that only mild nonlinearities exist in the response surface. Thus, the sensitivity factors obtained using first-order reliability methods are meaningful. Monte Carlo solutions using quadratic response surfaces of several other nodes of the LOX post are shown in Figures 1.2.36 through 1.2.38. Tables 1.2.3 and 1.2.4 summarize the response results for all examined nodes.

The sensitivity factors at various nodes (see Figure 1.2.1) are tabulated in Table 1.2.4. Hot-gas temperature plays a dominant role in the variability of strains regardless of whether the nodes are on the coolant or hot-gas side of the LOX post, as expected since the gradient of the temperature influences strain and the variation in the coolant temperature is relatively small. Furthermore, the node at the gap in the heat shield (node 56) shows highest sensitivity to variability in the size of the gap. Cracks have been observed at this location after repeated loadings. The gap of the heat shield is the most difficult random variable to estimate analytically. Thus, this study reinforces the need for assessing actual variability of the width of the gap in the heat shield.

## 1.3 Transfer Tube Liner Verification Analysis

### 1.3.1 Hardware Function And Load Description

The engine packaging concept used in SSME is shown in Figure 1.3.1 and in Figure 1.3.2. In Figure 1.3.1 the engine manifold configuration is shown. In Figure 1.3.2 the component integration is shown. Hot gas from preburners is ducted directly to high pressure turbines which then discharges the gas to a toroidal manifold. The high pressure, high flowrate, high temperature hydrogen rich gas then enters the hot gas transfer ducts. The gas is then routed to main injector torus where it is radially directed into hot gas cavity of the main injector. The hot gas manifold used in this study is the two duct configuration that is under development testing.

The manifold design uses the cooled structural shell concept. This is achieved by having a structural liner which forms an annular passage between the liner and the outer casing. The coolant, in this case gaseous hydrogen, flows through the annular passage. To protect the structural liner from hot gas impingement a scrub liner is provided. This verification study is concerned with the structural liner of the transfer tube together with portions of the fuel pump bowl inlet manifold.

The major loads on the structural liner are the temperature and pressure loads. The temperature loads are due to temperature gradient across the thickness and due to increase in its bulk temperature. The bulk temperature increase introduces large axial loads. This is because the liner is welded at the ends of the comparatively cool outer structural shell. In contrast, the scrub liner which has a much higher bulk temperature increase is cantilevered out to freely expand on one side. The pressure loads are due to pressure differential between the coolant and the hot gas. The structural integrity of the liner is crucial to the safety of the system. A leak and adverse pressure differential can cause the hot gases to be driven into the cooling system. Complete details of the transfer tube liner design are given in the initial survey reported in the first annual report.

One of the primary design requirements for the liner is an adequate factor of safety against buckling failure. Consistent with the philosophy of applying several types of probabilistic structural analysis with each component's primary design requirement in mind, the liner verification analysis considered probabilistic buckling analysis.

### 1.3.2 Deterministic Verification Analysis

Initial deterministic verification studies considered linear eigen value buckling analysis and nonlinear small strain large deflection analysis. The linear elastic analysis, frequency extraction analysis, linear dynamic harmonic and random vibration analysis, and material nonlinear analysis were considered as part of the earlier other verification studies considering other components. The results of these studies were reported in the earlier and the current annual reports. The earlier exercises however did not use the shell element that is being used in this study.

The deterministic verification analyses used in the transfer duct study were tailored first to compare the results already available from earlier runs done a few years ago using ANSYS finite element analysis software. This provided a check for reasonableness of the NESSUS results without having to rerun earlier ANSYS models. The earlier runs were for an old geometry (not the final design) where smaller thicknesses were used in the critical shall region. Further,

the finite element model contained minimum thicknesses as opposed to mean thicknesses that will be needed as a base for the probabilistic analysis. Additionally, there were assumptions in the earlier ANSYS runs about the possible worst case temperatures that were not appropriate in the context of probabilistic analysis. However, the NESSUS model was run using identical conditions for a valid comparison. The finite element model used in this study is shown in Figure 1.3.3, along with its statistics.

Since NESSUS/FEM is a nodally based code there are several issues that need to be addressed when an existing model from another code is converted. It is necessary to introduce duplicate nodes at the common junction if two finite elements meeting at a node have differing thicknesses (step change) or material types or any other differing element attribute. Further, in the case of 3 dimensional surface representation shell element, if there are abrupt changes in the shell normals then duplicate nodes are to be defined to obtain different shell normals. The particular finite element model that is used in this study has many duplicate nodes (Figure 1.3.3).

A linear buckling analysis of the shell was conducted to determine the buckling pressure load without the thermal loads present. This was accomplished by assuming the coefficient of thermal expansion to be zero. However, the user subroutine 'UTEMP' was utilized to evaluate the other material properties at the appropriate temperature.

The ANSYS linear buckling analysis results for the first five modes are compared with NESSUS results for the buckling pressure in Table 1.3.1. The NESSUS results were 9.9% to 16.9% higher than the corresponding ANSYS results. The differences can be due to different element types and formulations used. In ANSYS, triangular elements were used and in NESSUS assumed strain quadrilateral elements were used. Additionally, there are different initial stress fields in NESSUS when compared to ANSYS. The nodally based mixed formulation in NESSUS tries to obtain a smoother stress field when compared to displacement method finite element formulation. From a practical usage point of view, it is realized that linear buckling pressures are unconservative and in practice they are knocked down by a large factor. Thus, the differences are not considered significant.

Next, the small strain but large deflection analysis results were compared. The shell thermal loads were considered by assuming an appropriate temperature dependent coefficient of thermal expansion. The differential pressures on the shell were incremented in steps of 100 psi until the analysis procedure showed large deflections and nonconvergence of the numerical algorithms. The ANSYS and NESSUS results both indicated a collapse load of between 900 psi and 1000 psi. The large difference between the linear buckling analysis and the large deflection analysis is consistent with analysis experience when nonlinear effects due to geometry and plasticity are considered.

The NESSUS/FEM large deflection elastic plastic analysis results are shown in Figure 1.3.4 through Figure 1.3.8 at 900 psi which was the last converged equilibrium state. The deformed shape of the shell is very similar to the first pressure buckling mode.

Once the reasonableness of the NESSUS results was established, the NESSUS finite element model was then modified to reflect the mean temperature state (as opposed to worst case) as well as the actual final design thicknesses at the critical regions of the shell. The new buckling pressures for the first five modes are shown in Table 1.3.2 which reflect increased

values from Table 1.3.1 due to increases in thickness. The buckling modes corresponding to the first three modes are shown in Figures 1.3.9 through 1.3.11 wherein the contour values reflect the total displacements.

As part of developing the strategy for a probabilistic analysis for the transfer tube liner, a nonlinear collapse load analysis with the new thicknesses (actual design geometry) was completed. The new collapse pressure was calculated to be between 1500 and 1600 psi. The deformed shape of the liner shell as well as effective strains and stresses in the top and bottom faces are shown in Figure 1.3.12 through Figure 1.3.16. The exercise indicated that a probabilistic collapse load analysis of the shell will be extremely computationally intensive. A single deterministic collapse load analysis of the shell required 15 hours of CPU time on a Convex C-2 machine. The solution strategy used was a modified Newton-Raphson method with line search. The relative residual tolerance used was .15 which results in relatively high residuals when compared to a displacement method analysis. The iteration count residual history is shown in Table 1.3.3. It was shown earlier that use of identical strategy had given comparable results to the ANSYS software package. It was realized that any attempt to perform a probabilistic collapse load analysis would have to consider 200 to 300 hours of CPU time which was not practicable within the resources available at that time. This should be compared with a linear buckling analysis which took approximately 2 hours of CPU time for one incremental solution followed by eigen value extraction. The deformation pattern near the collapse further indicates a gross overload type of failure as opposed to an instability type of failure. Thus, it was concluded that the initial study should consider first a probabilistic linear buckling analysis of the shell. Consequently, the verification analysis conducted during this base contract was limited to probabilistic linear buckling analysis.

### 1.3.3 Probabilistic Liner Linear Buckling Analysis

Unlike the previous verification analyses done for other components this application of probabilistic analysis deals with estimation of the strength or resistance variable in the failure model. That is, if the distribution of the buckling strength of the shell can be determined, then considering the distribution of the differential pressure the probability of buckling failure considering the linear buckling analysis can be computed.

A number of physical parameters that affect the buckling load capacity of the shell can be considered in a probabilistic analysis. The particular configuration of the structural liner considered in this analysis has the following characteristics. It is a doubly curved shell in the inlet region (Figure 1.3.3). It has five zones of thickness. The transfer tube portion of the model itself is of single curvature with an elliptical shape. The parameters that could be considered as random variables in the context of linear buckling analysis are:

- 1) Nodal thicknesses
- 2) Nodal coordinates
- 3) Elastic material properties
- 4) Boundary conditions.

In this study, nodal thicknesses alone were considered as random. The variations in nodal coordinates may not be as significant as in a perfectly symmetric structure such as a perfect cylinder. The liner analyzed in this study is a doubly curved complex shell with no symmetry lines. The boundary conditions assumed at the ends of the shell can have a significant influence on the buckling loads of the shell but this was not investigated in this study. The variations in elastic properties were considered small and, thus, were considered deterministic. The variations in nodal thicknesses were modelled as independent random variables at each zone of the five zones of the shell. This also reflects the way the liner is manufactured and welded. Therefore, it is assumed in the model that the thickness variation in each zone of the shell is perfectly correlated but variations in thickness between the zones were considered independent.

The probabilistic analysis followed a strategy of response surface approach. In this approach several large perturbations of the random variable were conducted and a linear hyperplane response surface that was valid for the entire range was constructed through a regression analysis. The response surface function was then used in probability prediction calculations using either Monte Carlo or fast probability methods.

The assumed statistics of the random variables are shown in Table 1.3.4. A total of twenty-four perturbations was conducted to construct a linear response surface as shown in Table 1.3.5. Perturbations of all five random variables were conducted one at a time. In addition, the mixed terms were also considered by simultaneous perturbation of the random variables. It was observed that the random variable five, which was away from the buckling zone had minimal sensitivity to the buckling pressure. Hence, it was not considered in the construction of the response surface. That is, the thickness in zone five was considered deterministic. Further, it was observed that the random variables one and two representing the thicknesses of the shells in the region where the first buckling mode occurs had the greatest sensitivity. Consequently, the perturbations with mixed terms considered only the two random variables one and two. The results of the first buckling mode pressure are tabulated in Table 1.3.6 for all twenty-four perturbations.

The history of the number of iterations for convergence for all perturbations is shown in Table 1.3.7. It is to be noted that the first increment is a linear static analysis to obtain the correct initial stresses and increment two is the eigenvalue buckling analysis. The perturbed solutions for increment one were obtained by iteration from the deterministic state while the solutions for increment two were obtained by resolution.

The multivariate regression analysis to obtain the coefficients for the linear response surface was conducted external to NESSUS/FPI using IMSL routines. The basic data and the results are tabulated in Table 1.3.8. The CDF was obtained by first-order reliability and also by the Monte Carlo method which is available as an option in NESSUS/FPI. The results are tabulated in Table 1.3.9 and shown in Figure 1.3.17.

The sensitivity analysis results as well as the probability calculations using the FPI first order reliability method, indicates that the buckling pressure is nearly related linearly to thicknesses. Analytical buckling formulas also indicate the linear dependence of the buckling pressure to the shell thickness. The sensitivity factors of the random variables one through four are shown in Table 1.3.10 as a function of the response level. The results are consistent with the physical realities of the problem.

#### 1.3.4 Suggested Follow-On Work On The Liner Verification Analysis

The linear liner buckling analysis conducted in this base contract could be extended to include the following effects in the probabilistic buckling pressure load calculations.

1. Nodal coordinate variations in each zone with a distance dependent correlation model. The NESSUS/PRE module can be used to reduce the number of correlated random variables to a few independent random variables. Each zone of the liner consistent with the production methods can be treated as independent.
2. The boundary conditions can be considered uncertain. In the analysis conducted in the base contract, a conservative hinged connection was assumed at support of the shell. However, somewhere between a fully hinged and a fully fixed boundary condition exists. This uncertainty could be considered in the buckling analysis.
3. An estimate of the variation in differential pressure between the coolant and hot gas should be obtained from the Composite Load Spectra contract. Considering the differential pressure (Load Variable) and linear buckling pressure load (strength variable), the reliability of the shell for a linear buckling load analysis can be computed. However, it must be cautioned that estimates will have to be understood in the context of the unconservative prediction of buckling using linear eigenvalue analysis.
4. The verification studies can then be extended to include a true probabilistic collapse load analysis. The additional random variables to be considered in the probabilistic nonlinear collapse load analysis include:
  - a) Material property variation (both elastic and inelastic)
  - b) Temperature variation

Before this full-scale analysis can be attempted, the NESSUS/FEM code capabilities in the area of small strain or large strain with large deflection options needs to be improved. This is necessary to reduce the computational time per perturbation as well as to improve the accuracy of the code. But with the necessary improvements, the objectives can be met.

Table 1.1.1 Natural Frequencies of HPOT Duct.

MODE	NESSUS	
	Constrained Big Mass Approach	Free-Free Model With Shift Option **
1.	.050*	.01639*
2.	.060	.0524*
3.	.071*	.0612*
4.	.074	.1888
5.	.081	.1907
6.	.087*	.3269
7.	.097	.40211
8.	.107	.6052
9.	.119	.8525
10.	61.66	61.11
11.	97.96	97.96
12.	134.06	134.07
13.	140.21	140.22
14.	175.35	175.35
15.	197.32	197.32
16.	251.71	251.72
17.	275.36	275.37
18.	299.50	299.50
19.	380.15	380.15
20.	422.99	422.99
21.	516.41	516.42
22.	555.71	555.72
23.	575.21	575.21
24.	635.26	635.27
25.	694.71	694.72
26.	768.29	768.29

\* Rigid Body Modes

\*\* Modes in Free-Free Model are Extracted in Random Order

TABLE 1.1.6  
HPOTP DISCHARGE DUCT ANALYSIS  
RANDOM VARIABLE STATISTICS

SEQUENTIAL NO.	RANDOM VARIABLE DESCRIPTION	MEAN	ST. D.	COV
1)	ZONE 6 - X AXIS, PSD POWER	222.0	163.0	0.73
2)	ZONE 6 - Y AXIS, PSD	73.5	59.4	0.808
3)	ZONE 6 - Z AXIS, PSD	73.5	59.4	0.808
4)	ZONE A - X AXIS, PSD	22.5	4.5	0.20
5)	ZONE A - Y AXIS, PSD	54.0	10.8	0.20
6)	ZONE A - Z AXIS, PSD	69.5	13.9	0.2
7)	OXIDIZER PUMP SPEED	2940.53	41.167	0.014
8)	FUEL PUMP SPEED	3707.08	37.07	0.01
9)	ZONE A MAIN INJECTOR DAMPING	0.033	.005	0.15
10)	OXIDIZER PUMP SINE AMPLITUDES X DIRECTION 1N	.30	.120	0.4
11)		0.30	.045	0.15
12)	Y DIRECTION 4N	1.5	.45	0.3
13)		0.60	0.30	0.5
14)	Z DIRECTION 4N	2.6	.28	.40
15)		0.5	.78	.3
16)	Z DIRECTION 1N	0.5	.225	0.45
17)		0.70	.140	0.20
18)	FUEL PUMP SINE AMPLITUDES X DIRECTION 4N	0.70	.140	.20
19)		.35	1.050	.3
20)	Y DIRECTION 1N	0.80	0.280	0.35
21)	Z DIRECTION 1N	1.20	0.96	0.3
22)	ZONE 6 - OXIDIZER TURBOPUMP OXIDIZER PUMP SINE AMPLITUDES X DIRECTION 1N	1.35	1.35	1.0
23)		1.50	0.75	0.5
24)	3N	1.10	0.495	0.45
25)	4N	11.0	2.75	0.25
26, 27)	Y&Z DIRECTION 1N	1.9	1.71	0.9
28, 29)		1.6	0.96	0.6
30, 31)	2N	0.75	0.225	0.3
32, 33)	3N	5.5	3.30	0.6
34)	FUEL PUMP SINE AMPLITUDES X DIRECTION 1N	0.65	0.2275	0.35
35, 36)	Y&Z DIRECTION 1N	0.45	1.35	.3
37, 38)	Y&Z DIRECTION 2N	0.45	0.180	.4

NOTE:  
 1) POWER UNITS ARE IN  $\text{G}^2$   
 2) PUMP SPEED UNITS ARE IN RADIAN/SECOND  
 3) SINUSOIDAL AMPLITUDE UNITS ARE IN GRMS

Table 1.1.3

HPOTP DISCHARGE DUCT ANALYSIS  
MVFO RESULTS

COMPONENT RMS RESPONSE	FIRST ORDER		BASED ON COMPLETE CDF	
	MEAN	STD. DEVIATION	MEAN	STD. DEVIATION
1 - Shear Y	221.32	31.4	217.96	30.28
2 - Shear Z	206.16	40.13	203.77	39.51
3 - Axial	373.13	44.07	369.95	43.77
4 - Bending Y	1859.69	211.12	1840.8	210.37
5 - Bending Z	1969.38	250.23	1942.8	242.34
6 - Torsion	1026.05	114.56	1015.0	112.28

Table 1.1.4

HPOTP DISCHARGE DUCT ANALYSIS  
COMPUTATIONAL STATISTICS

NO	COMPUTATIONAL STEP	CPU TIME VAX 11/750	MODEL:
1	MODAL ANALYSIS	7,200 SECS. (2 HRS.)	300 NO. OF NODES:
2	1 P.S.D. RANDOM	620 SECS.	40 NO. OF DUP. NODES:
3	ONE HARMONIC ANALYSIS	30 SECS.	188 NO. OF ELEMENTS:
4	TOTAL DETERMINISTIC ANALYSIS	11,820 SECS. (3.82 HRS.)	NO. OF ACTIVE D.O.F.
4	TOTAL PERTURBATION ANALYSIS TIME FOR MWFO (NESSUS 3.1 RELEASE) (35 SPECTRAL CASES)	77,370 SECS. (21.49 HRS.)	AVERAGE PROFILE HEIGHT: 13
5	TOTAL PERTURBATION TIME IF ALL SUGGESTED INTELLIGENCE IS BUILT IN (ESTIMATE)	5,680 SECS.	
6	FPI PROCESSING FOR ONE NODE ONE COMPONENT	890 SECS.	

Table 1.2.1: Statistics of Independent Random Variables Influencing Temperature Distribution on the LOX Post

Random Variable	Mean	Standard Deviation	Distribution
Hot-Gas Temperature (R)	1654.70	26.6407	Normal
Coolant Temperature (R)	191.643	4.21019	Normal
Hot-Gas Flowrate (lbm/sec)	167.249	1.0928	Normal
Coolant Flowrate (lbm/sec)	929.918	4.31211	Normal
Mixture Ratio	0.948012	0.0184211	Normal
Heat-Shield-Gap Factor	0.47	0.235	Lognormal
Hot-Gas Film Coefficient	1.0	0.1	Normal
Coolant Film Coefficient	1.0	0.08	Normal

Table 1.2.2.: Inconel 718 and Haynes 188 Temperature-Dependent Material Properties

Inconel 718

Temperature*	Elastic Modulus**	Poisson's Ratio	Thermal Coef. of Exp. †	Shear Modulus**
60.0	30.2	.240	5.1064E-06	12.2
160.0	30.1	.250	6.2162E-06	12.0
560.0	29.5	.290	6.6667E-06	11.4
960.0	28.1	.282	7.9070E-06	10.9
1360.0	25.9	.278	8.0723E-06	10.1
1760.0	23.2	.299	8.7805E-06	8.9
2160.0	17.4	.338	9.3252E-06	6.5

Haynes 188

Temperature*	Elastic Modulus**	Poisson's Ratio	Thermal Coef. of Exp. †	Shear Modulus**
60.0	36.5	.305	5.1063E-06	14.0
160.0	35.9	.310	5.4054E-06	13.7
560.0	33.5	.318	6.6667E-06	12.7
960.0	30.5	.322	6.2791E-06	11.5
1360.0	28.1	.330	6.9880E-06	10.6
1760.0	25.5	.332	7.8862E-06	9.6
2160.0	22.9	.339	8.5276E-06	8.6

\* Temperature in Rankine.

\*\* Moduli in Msi.

† Thermal coefficient of expansion in units of in/in\*Rankine.

Table 1.2.3: Summary Statistics of the Effective Strain Range for the LOX Post

Node	Median	Mean	Standard Deviation	Coef. of Variation
56	0.004143	0.004821	0.0002613	0.054
78	0.006759	0.008360	0.0002275	0.027
84	0.002114	0.004175	0.0001661	0.040
117	0.002990	0.004757	0.0001454	0.031
122	0.001186	0.003831	0.0001473	0.038
175	0.002949	0.005135	0.0001430	0.028
181	0.002296	0.002401	0.00006408	0.027

Table 1.2.4: Sensitivity Factors\* of the Effective Strain Range for the LOX Post

Random Variable	Node 56	Node 78	Node 84	Node 117	Node 122	Node 75	Node 181
Hot-Gas Temp.	.455	.796	.771	.802	.793	.860	.786
Coolant Temp.	.014	.026	.024	.023	.023	.019	.022
Hot-Gas Flowrate	.062	.075	.111	.070	.074	.045	.108
Coolant Flowrate	.000	.003	.002	.002	.002	.001	.003
Mixture Ratio	.022	.034	.034	.035	.034	.028	.031
Shield-Gap Fctr	.793	.115	.071	.028	.003	.011	.017
Hot-Gas Film Coef	.399	.587	.620	.590	.603	.507	.605
Coolant Film Coef	.002	.031	.042	.024	.026	.005	.052

\* Range between 0 and 1. Larger values indicate a greater influence of the random variable on the response.

TABLE 1.3.1. LINEAR BUCKLING ANALYSIS COMPARISON  
MINIMUM THICKNESS OLD GEOMETRY CASE

MODE	NESSUS	ANSYS	% DIFFERENCE WITH REFERENCE TO ANSYS
1	1945.75 psi	1709.88	+ 13.8%
2	2052.79 psi	1797.81	+ 14.2%
3	2442.45 psi	2097.42	+ 16.5%
4	2474.69 psi	2117.73	+ 16.9%
5	2731.77 psi	2485.76	+ 9.9%

0085b

TABLE 1.3.2

Mode	Buckling Pressure PSI
1	2363.09
2	2567.09
3	2800.05
4	2824.15
5	3424.28

0085b

TABLE 1.3.3 ITERATION COUNT AND RESIDUAL HISTORY FOR THE COLLAPSE LOAD ANALYSIS

INCREMENT NO.	NUMBER OF ITERATION	RELATIVE ERROR IN RESIDUALS	ABSOLUTE ERROR IN RESIDUALS	MEAN SQUARE ERROR IN DISPLACEMENT	MEAN SQUARE ERROR IN ENERGY
0	14	0.14903	1293.8	0.012775	.088398
1	9	0.1449	1313.6	0.021606	.098715
2	7	0.14596	1404.9	0.02169	0.11552
3	9	0.14077	1439.2	0.01703	0.11695
4	12	0.13681	1485.1	0.011806	0.10593
5	17	0.14058	1629.1	0.0075049	0.11310
6	28	0.14373	1775.4	0.0051768	0.097934
7	32	0.14889	1956.5	0.003731	0.094365
8	39	0.14559	2028.7	.0032037	0.085201
9	27	0.14263	2092.5	.0050411	0.088802
10	15	0.14860	2274.8	.018733	0.10512
11	2	0.092906	1438.0	1.1666	0.11505
12	35	0.14956	2447.2	.013282	0.085175
13	4	0.11805	1942.3	1.3652	0.13772
14	3	0.14378	2395.2	1.3716	0.1588

TABLE 1.3.4: Definition of Random Variables

RV No.	Mean Thickness	Standard Deviation	Distribution
1	0.1800	0.005	Normal
2	0.1800	0.005	Normal
3	0.2250	0.0025	Normal
4	0.1250	0.0025	Normal
5	0.1150	0.005	Normal

TABLE 1.3.5: Definition of Perturbations

Perturb	RV 1	RV 2	RV 3	RV 4	RV 5
0	0	0	0	0	0
1	- $2\sigma$	0	0	0	0
2	- $1\sigma$	0	0	0	0
3	+ $1\sigma$	0	0	0	0
4	+ $2\sigma$	0	0	0	0
5	0	- $2\sigma$	0	0	0
6	0	- $1\sigma$	0	0	0
7	0	+ $1\sigma$	0	0	0
8	0	+ $2\sigma$	0	0	0
9	0	0	- $2\sigma$	0	0
10	0	0	- $1\sigma$	0	0
11	0	0	+ $1\sigma$	0	0
12	0	0	+ $2\sigma$	0	0
13	0	0	0	- $2\sigma$	0
14	0	0	0	- $1\sigma$	0
15	0	0	0	+ $1\sigma$	0
16	0	0	0	+ $2\sigma$	0
17	+ $1\sigma$	+ $1\sigma$	0	0	0
18	+ $1\sigma$	+ $2\sigma$	0	0	0
19	+ $2\sigma$	+ $1\sigma$	0	0	0
20	+ $2\sigma$	+ $2\sigma$	0	0	0
21	- $1\sigma$	+ $1\sigma$	0	0	0
22	+ $1\sigma$	- $1\sigma$	0	0	0
23	- $2\sigma$	+ $2\sigma$	0	0	0
24	+ $2\sigma$	- $2\sigma$	0	0	0

0085b

TABLE 1.3.6: Linear Eigenvalue Buckling Perturbation Analysis Results

Perturb. No.	1	Eigenvalues (Pressure Psi)		4	5
		2	3		
0	2363.09	2567.09	2800.65	2824.15	3424.28
1	2169.57	2352.45	2799.33	2822.75	3423.01
2	2267.80	2458.39	2799.91	2823.38	3423.64
3	2459.40	2681.17	2801.69	2825.23	3424.89
4	2559.72	2794.77	2808.83	2829.84	3425.42
5	2244.80	2414.61	2789.47	2813.10	3413.24
6	2303.31	2489.46	2795.05	2818.62	3418.77
7	2424.58	2647.93	2806.28	2829.70	3429.72
8	2488.10	2731.93	2812.15	2835.41	3435.04
9	2362.73	2566.79	2794.82	2818.19	3417.82
10	2361.91	2566.94	2797.74	2821.18	3421.06
11	2363.28	2567.25	2803.55	2827.11	3427.48
12	2363.46	2567.41	2806.43	2830.06	3430.65
13	2354.55	2541.69	2561.38	2571.90	3103.80
14	2359.36	2563.89	2670.86	2692.49	3260.44
15	2366.41	2569.94	2936.97	2962.08	3595.81
16	2369.52	2572.72	3079.86	3106.45	3775.51
17	2523.83	2763.86	2808.18	2831.43	3430.25
18	2589.98	2811.20	2832.28	2859.20	3435.55
19	2624.80	2807.77	2830.08	2893.62	3430.78
20	2689.95	2815.05	2837.40	2981.74	3436.08
21	2330.96	2539.07	2805.34	2828.73	3429.00
22	2396.93	2600.82	2795.92	2819.57	3419.46
23	2297.77	2513.87	2810.01	2833.28	3433.64
24	2434.09	2642.97	2791.18	2815.02	3414.53

0085b

TABLE 1.3.7 Iteration History for the Perturbed Eigenvalue Problem

Pert No.	Increment = 0 Static Analysis	Increment = 1 Subspace Iteration
0	22	21
1	17	15
2	9	15
3	9	15
4	15	15
5	3	15
6	2	15
7	2	15
8	3	15
9	1	15
10	1	15
11	1	15
12	1	15
13	1	15
14	1	15
15	1	15
16	1	15
17	10	15
18	11	15
19	16	15
20	16	15
21	8	15
22	8	15
23	14	15
24	13	15

0085b

TABLE 1.3.8 Multivariate Regression Analysis Results

$$r = a_0 + a_1 x_1 + a_2 x_2 + a_3 x_3 + a_4 x_4 + a_5 x_1 x_2$$

Observations

Data Set	r	x1	x2	x3	x4	x1x2
0	2363.09	0.1800	0.1800	0.2250	0.1250	0.0324
1	2169.57	0.1700	0.1800	0.2250	0.1250	0.0306
2	2267.80	0.1750	0.1800	0.2250	0.1250	0.0315
3	2459.40	0.1850	0.1800	0.2250	0.1250	0.0333
4	2559.72	0.1900	0.1800	0.2250	0.1250	0.0342
5	2244.80	0.1800	0.1700	0.2250	0.1250	0.0306
6	2303.31	0.1800	0.1750	0.2250	0.1250	0.0315
7	2424.58	0.1800	0.1850	0.2250	0.1250	0.0333
8	2488.10	0.1800	0.1900	0.2250	0.1250	0.0342
9	2362.73	0.1800	0.1800	0.2200	0.1250	0.0324
10	2362.91	0.1800	0.1800	0.2225	0.1250	0.0324
11	2363.28	0.1800	0.1800	0.2275	0.1250	0.0324
12	2363.46	0.1800	0.1800	0.2300	0.1250	0.0324
13	2354.55	0.1800	0.1800	0.2250	0.1200	0.0324
14	2359.36	0.1800	0.1800	0.2250	0.1225	0.0324
15	2366.41	0.1800	0.1800	0.2250	0.1275	0.0324
16	2369.52	0.1800	0.1800	0.2250	0.1300	0.0324
17	2523.83	0.1850	0.1850	0.2250	0.1250	0.034225
18	2589.98	0.1850	0.1900	0.2250	0.1250	0.03515
19	2624.80	0.1900	0.1850	0.2250	0.1250	0.03515
20	2689.95	0.1900	0.1900	0.2250	0.1250	0.0361
21	2330.96	0.1750	0.1850	0.2250	0.1250	0.032375
22	2396.93	0.1850	0.1750	0.2250	0.1250	0.032375
23	2297.77	0.1700	0.1900	0.2250	0.1250	0.0323
24	2434.09	0.1900	0.1700	0.2250	0.1250	0.0323

0085b

TABLE 1.3.8 Continued

## Computed Coefficients of the Polynomial

$a_0 =$	-.3245	5111	3694	0016	E + 04
$a_1 =$	.1748	0788	6837	7155	E + 05
$a_2 =$	.1053	8401	5869	9801	E + 05
$a_3 =$	.7320	0000	0006	1238	E + 02
$a_4 =$	.1479	6000	0000	0203	E + 04
$a_5 =$	.1126	5263	3144	4107	E + 05

0085b

TABLE 1.3.9 Cumulative Distribution Function Obtained from First Order Reliability Method and Monte Carlo

Pressure Psi	Probability %	
	FPI	Monte Carlo
2150	3.03	3.27
2200	7.66	7.76
2250	16.20	16.98
2300	29.24	29.75
2350	45.55	45.91
2400	62.49	62.49
2450	77.15	77.74
2500	87.79	87.56
2550	94.32	94.61
2600	97.70	97.59
2650	99.19	99.18
2700	99.75	99.81

0085b

TABLE 1.3.10 Sensitivity Factors a Random Variables to the First Buckling Mode

Random Variable Number	Sensitivity Factors of Random Variables							
	2150psi	2200psi	2250psi	2300psi	2350psi	2400psi	2450psi	2500psi
$x_1$	.8375	.8381	.8388	.8395	.8401	.8407	.8414	.8420
$x_2$	.5455	.5444	.5435	.5425	.5414	.5405	.5395	.5385
$x_3$	.0016	.0016	.0017	.0016	.0015	.0016	.0015	.0015
$x_4$	.0332	.0329	.0326	.0322	.0319	.0316	.0313	.0310

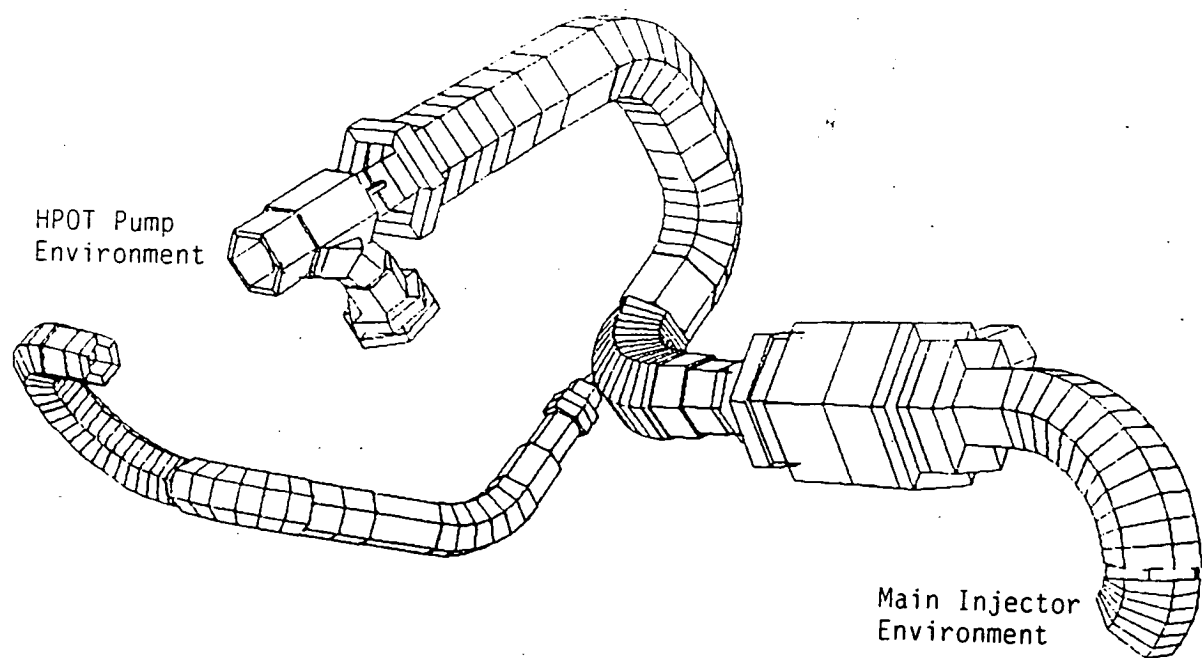


Fig. 1.1.2

Schematic Representation of High Pressure duct model with radii, Flange and Valve attachments.

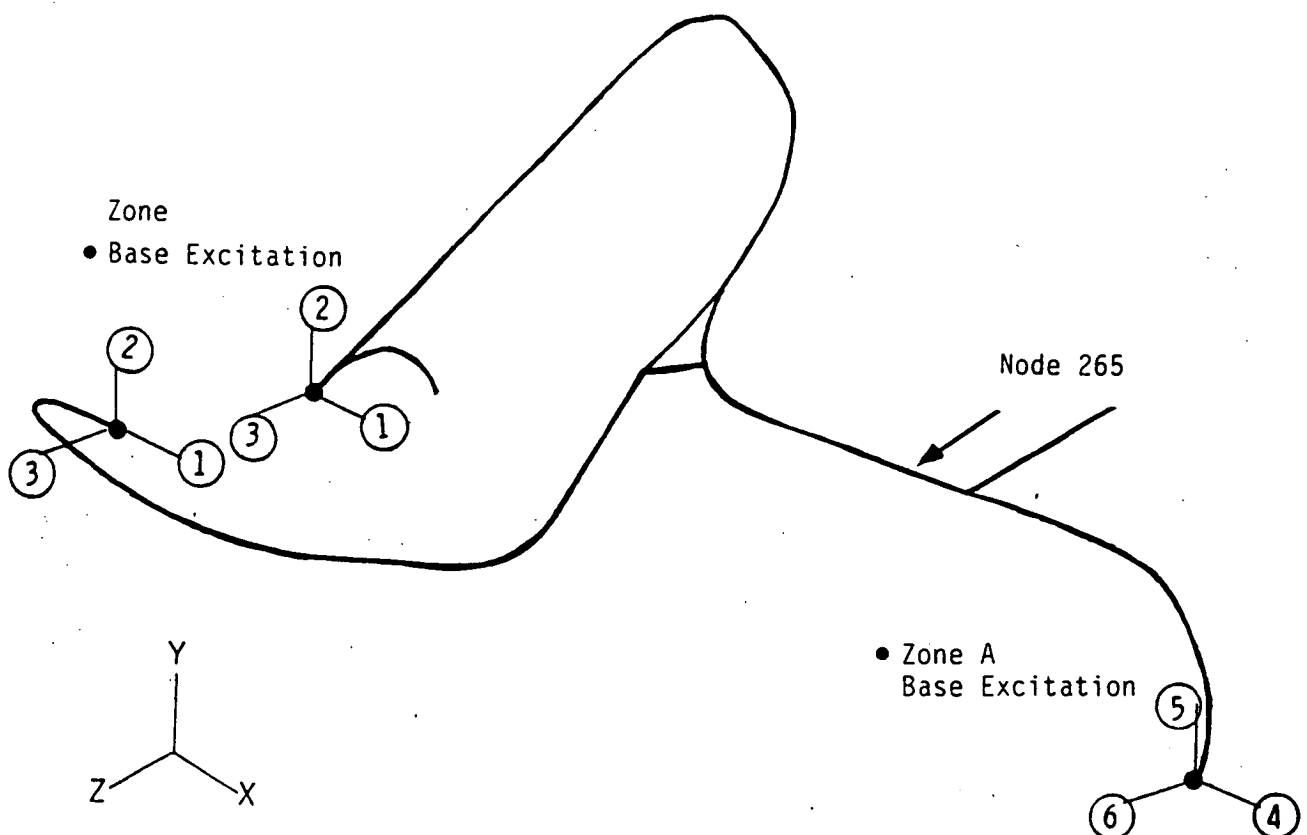


Fig. 1.1.1

HPOTP Discharge Duct Finite Element Model

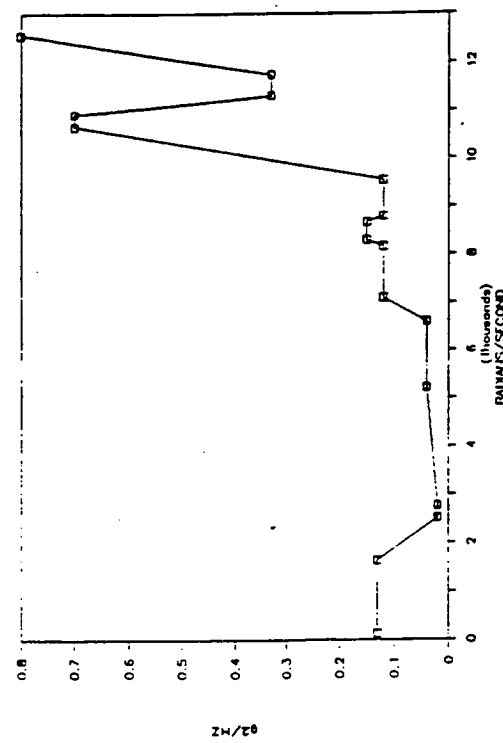


Fig. 1.1.3a Pump x-axis vibration  
Environment

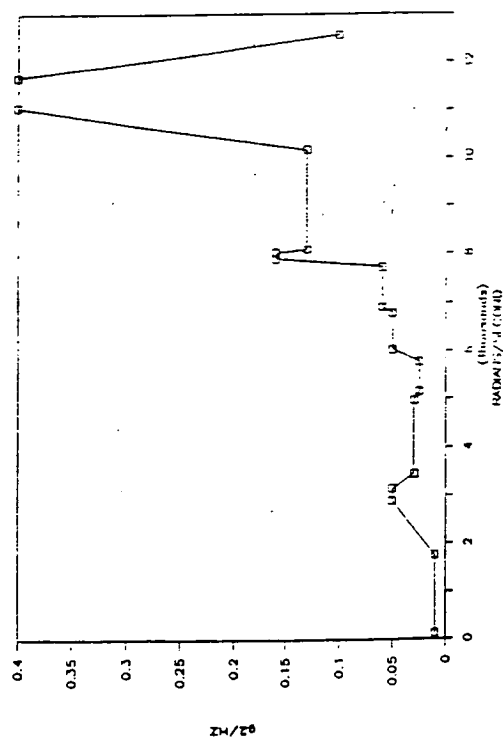


Fig. 1.1.3b Pump y & z-axis vibration  
Environment

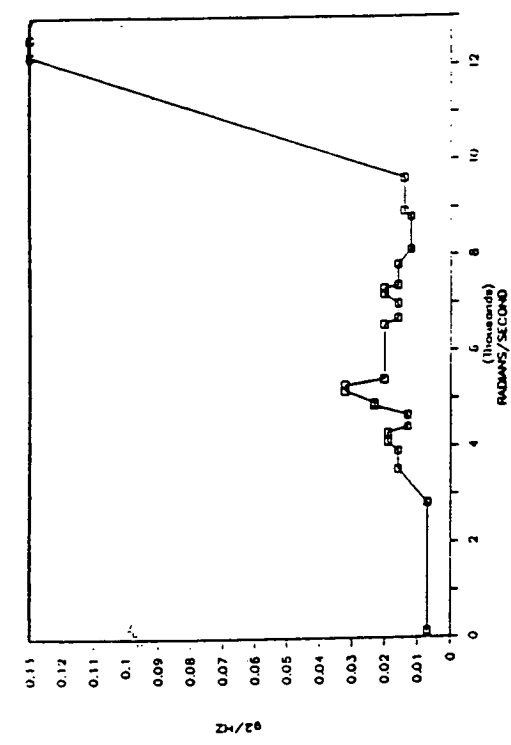


Fig. 1.1.3c Main Injector x-axis Vibration Environment

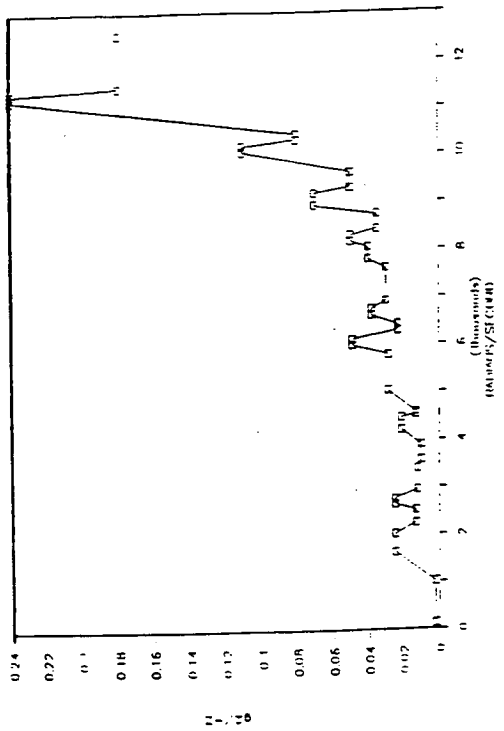


Fig. 1.1.3e Main Injector z-axis Vibration Environment

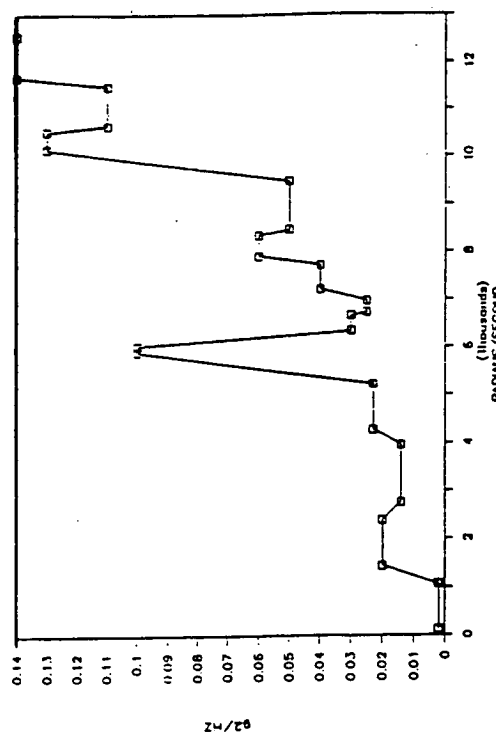


Fig. 1.1.3d Main Injector y-axis Vibration Environment

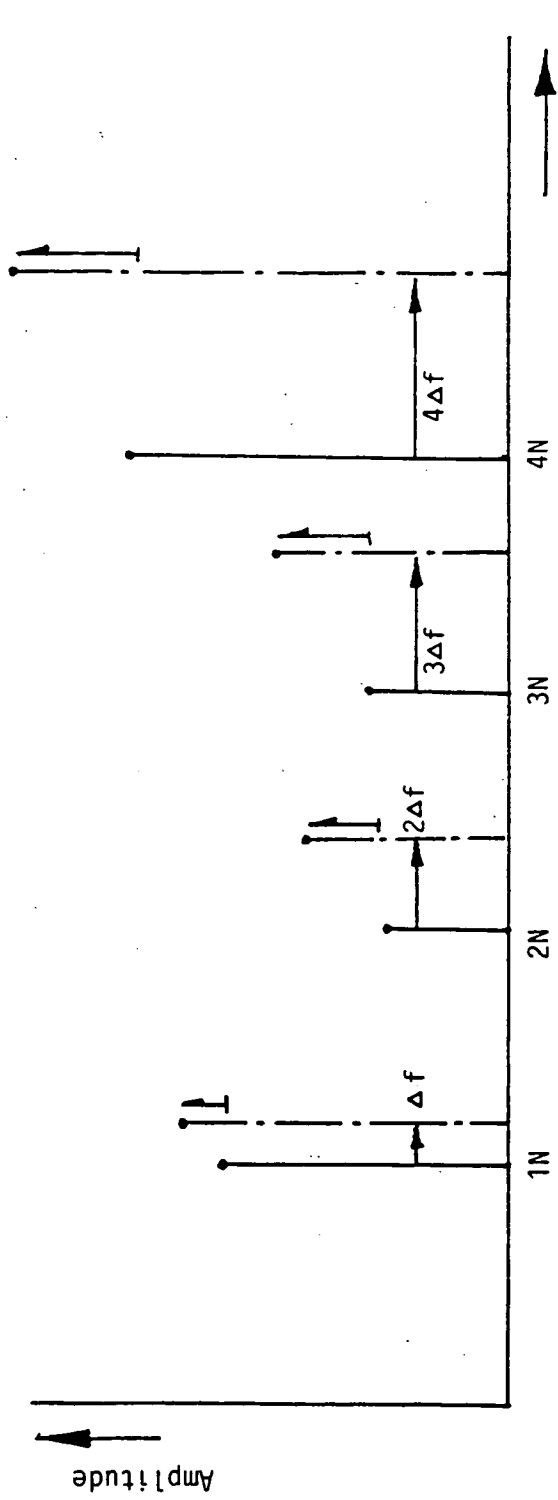


Fig. 1.1.4a Effect of pump speed variation on harmonic excitation

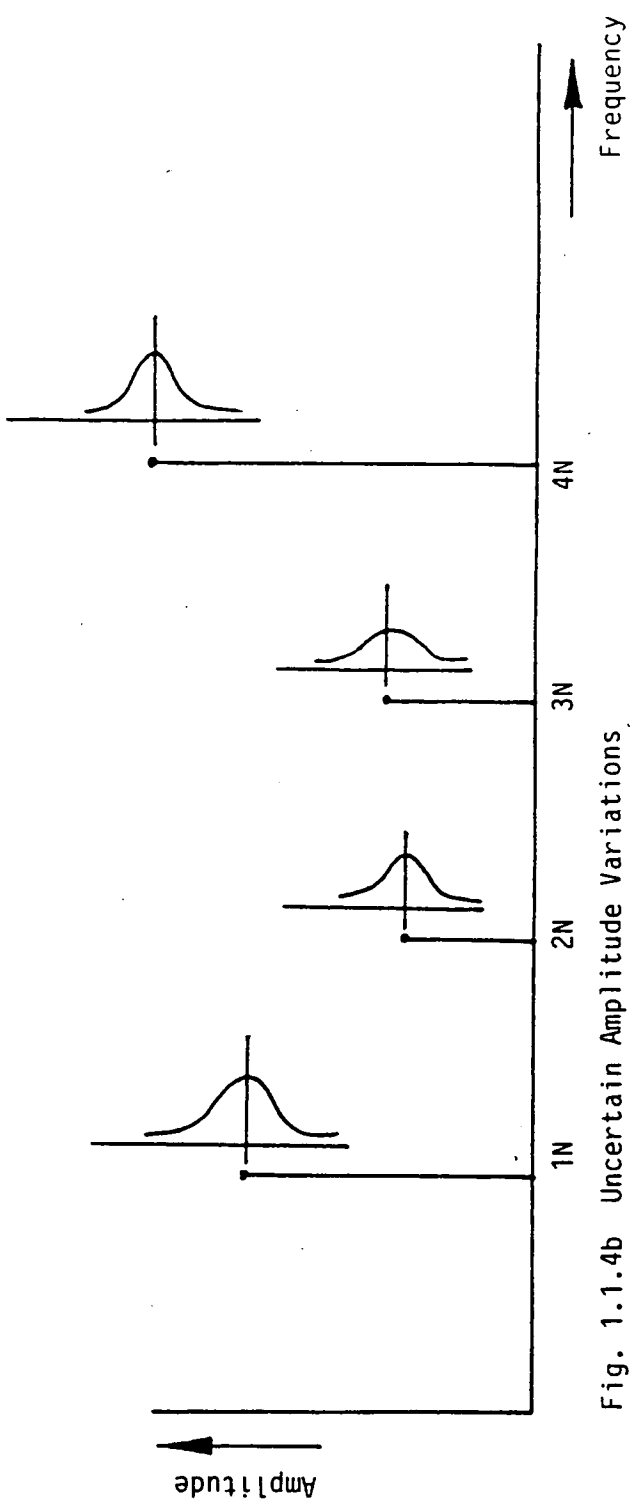


Fig. 1.1.4b Uncertain Amplitude Variations

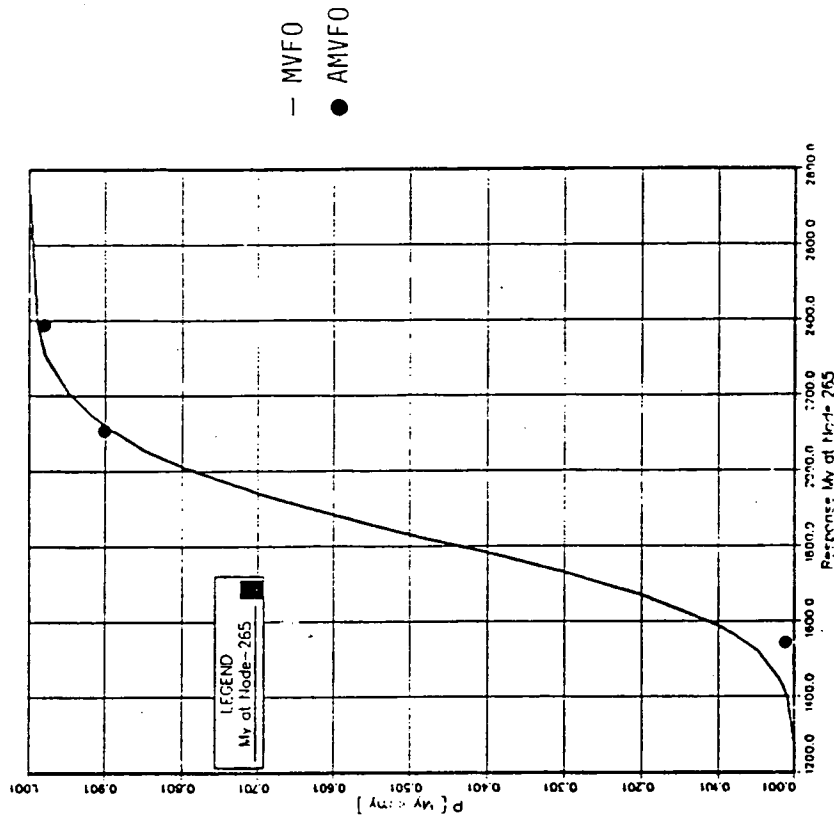


Fig. 1.1.5b CDF of Response based on MVFO and AMVFO methods

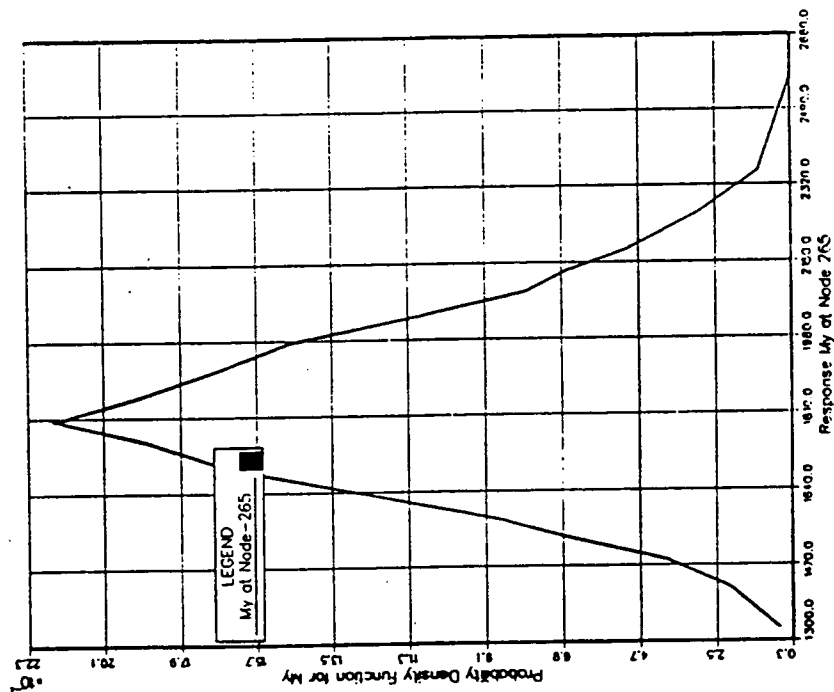


Fig. 1.1.5a PDF of Response Based on MVFO analysis

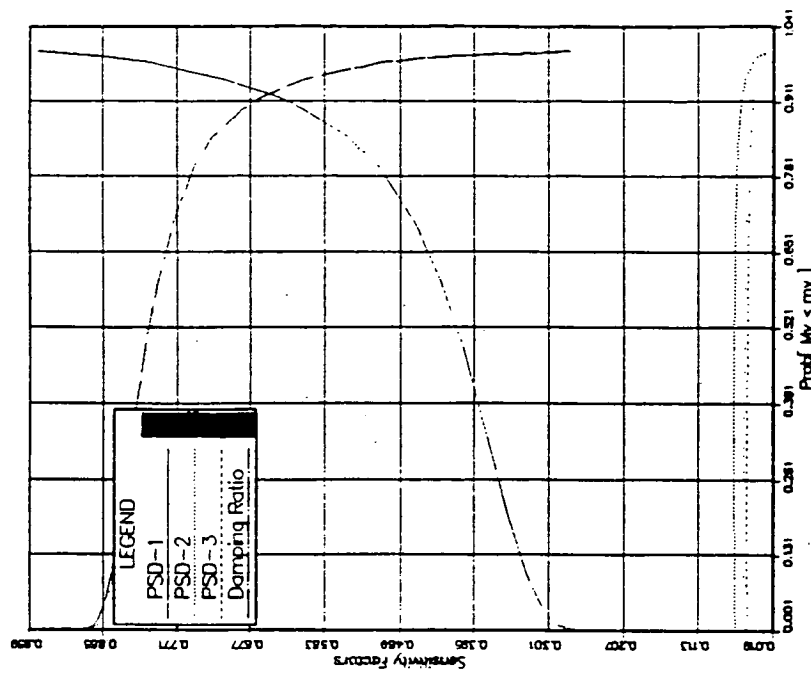


Fig. 1.1.6a Sensitivity factor as a function of response level.

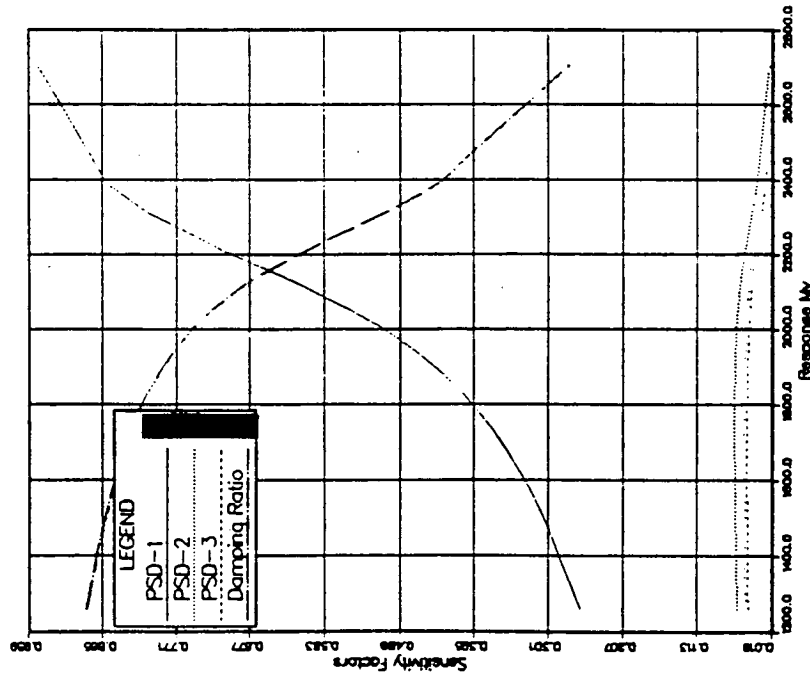
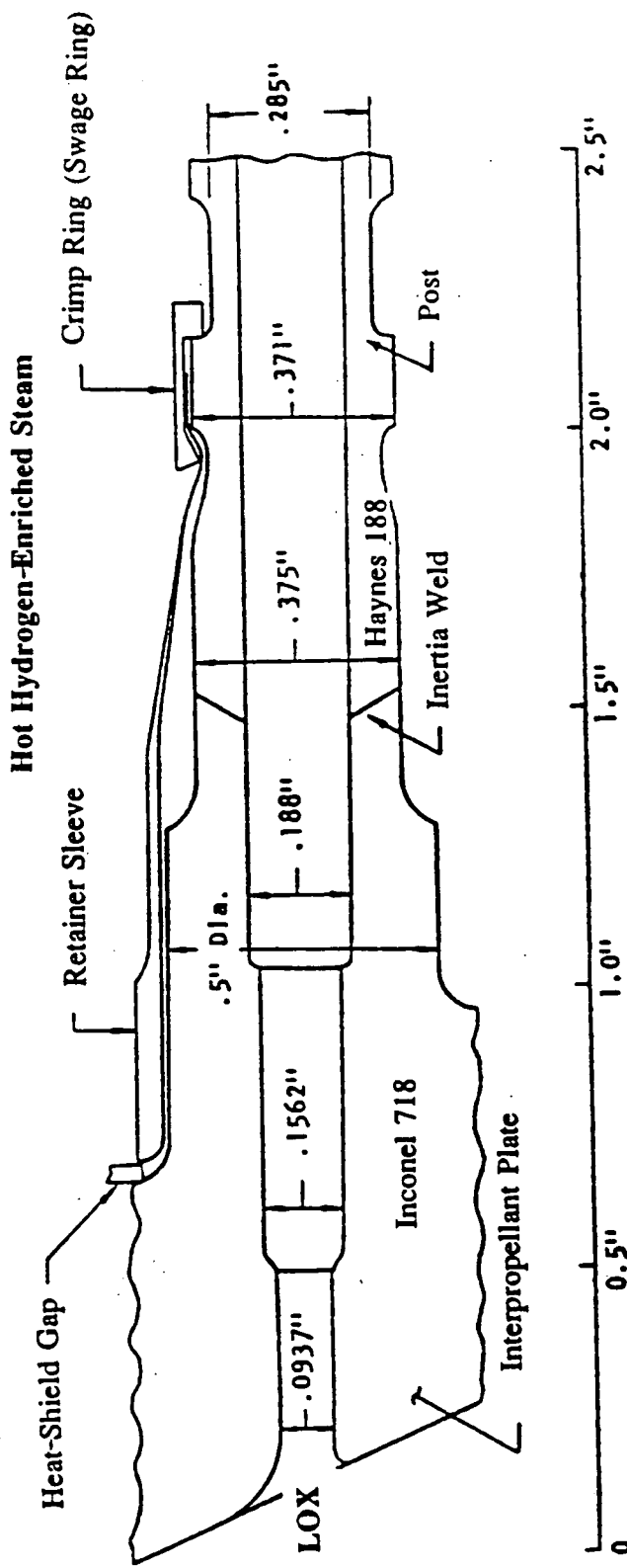


Fig. 1.1.6b Sensitivity factor as a function of probability level in CDF.



### LOX Post Axisymmetric Model

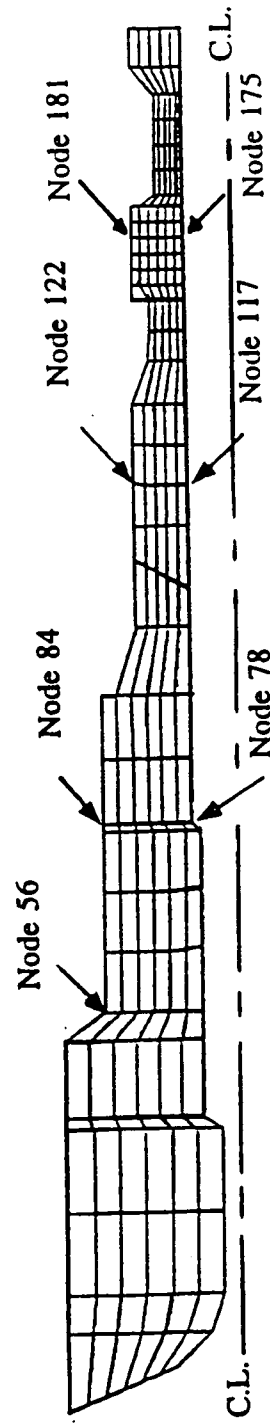


Figure 1.2.1: LOX post and its axisymmetric finite element model.

MATERIALS  
PROPERTIES  
MANUAL

TYPICAL (PREDICTED)

STA-1 OR STA-2

DATE-01-14-87

REFERENCE-6105-60 (MPR 85-0028)

3RD EDITION PAGE-6105.27.10.70-01

6105.27.10.70-01A

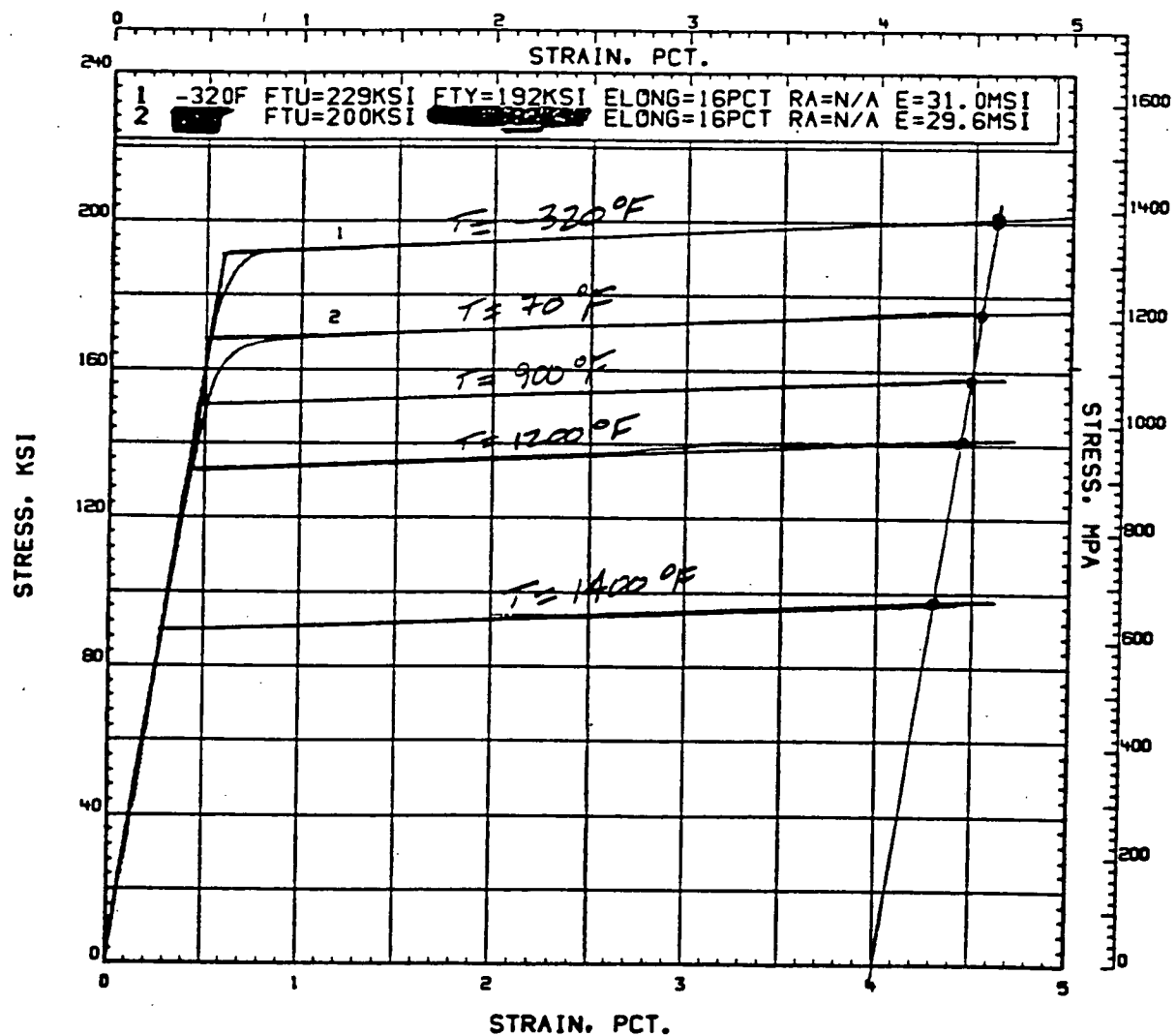
INCONEL 718

STRESS-STRAIN DIAGRAM

THROUGH CONVENTIONAL

TEST

SPEC R80170-153.15



4th Edition

1-31-87

Figure 1.2.2: Temperature-dependent stress-strain curves of Inconel 718.

MATERIALS  
PROPERTIES  
MANUAL

TYPICAL

8002.27.10.74-01

HAYNES 188

STRESS-STRAIN DIAGRAM

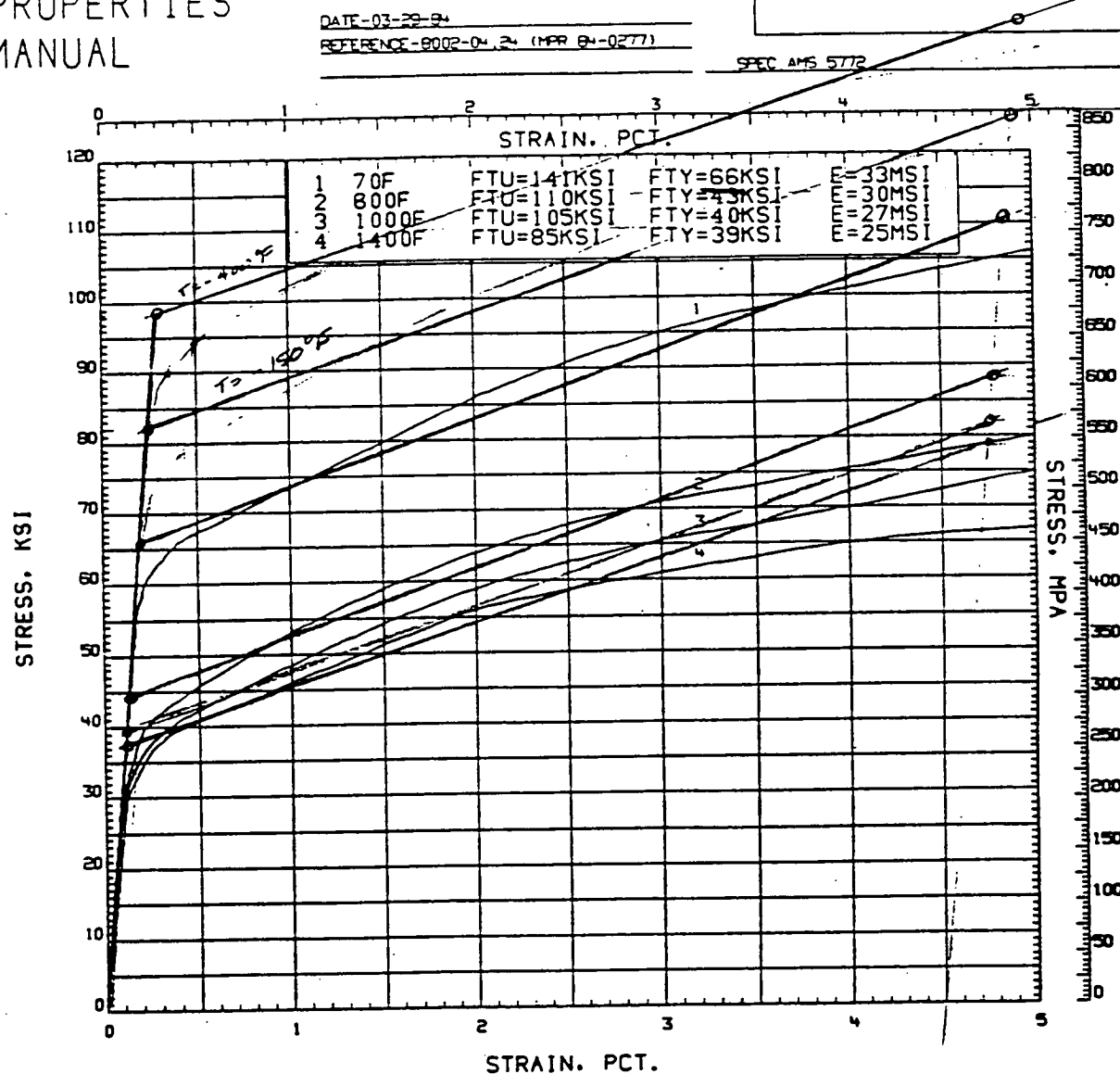
WROUGHT, CONVENTIONAL

718 STA-1

SPEC AMS 5772

DATE-03-29-94

REFERENCE-8002-04-24 (MPR B4-0277)



4th Edition  
10-30-87

Figure 1.2.3: Temperature-dependent stress-strain curves of Haynes 188.

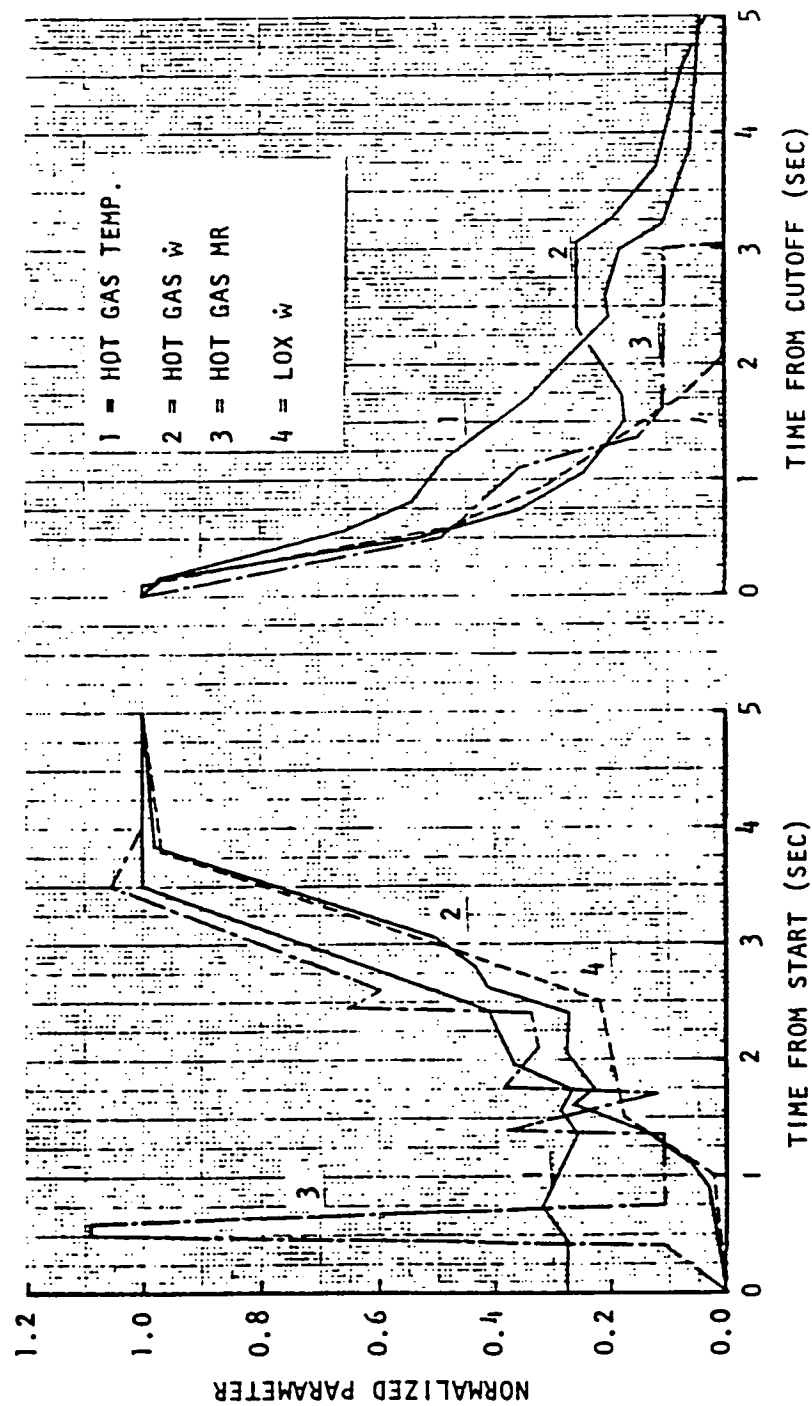


Figure 1.2.4: Variability of the hot-gas temperature, the hot-gas flowrate, the mixture ratio, and the coolant flowrate affecting the temperature distribution on the LOX post over a duty cycle of the engine.

FOUR-NODE PLANE STRESS ELEMENT

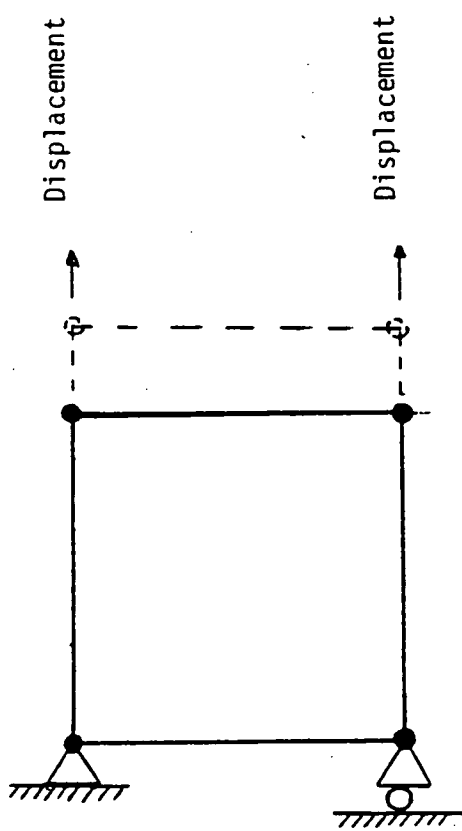


Figure 1.2.5: Four-node plane-stress element.

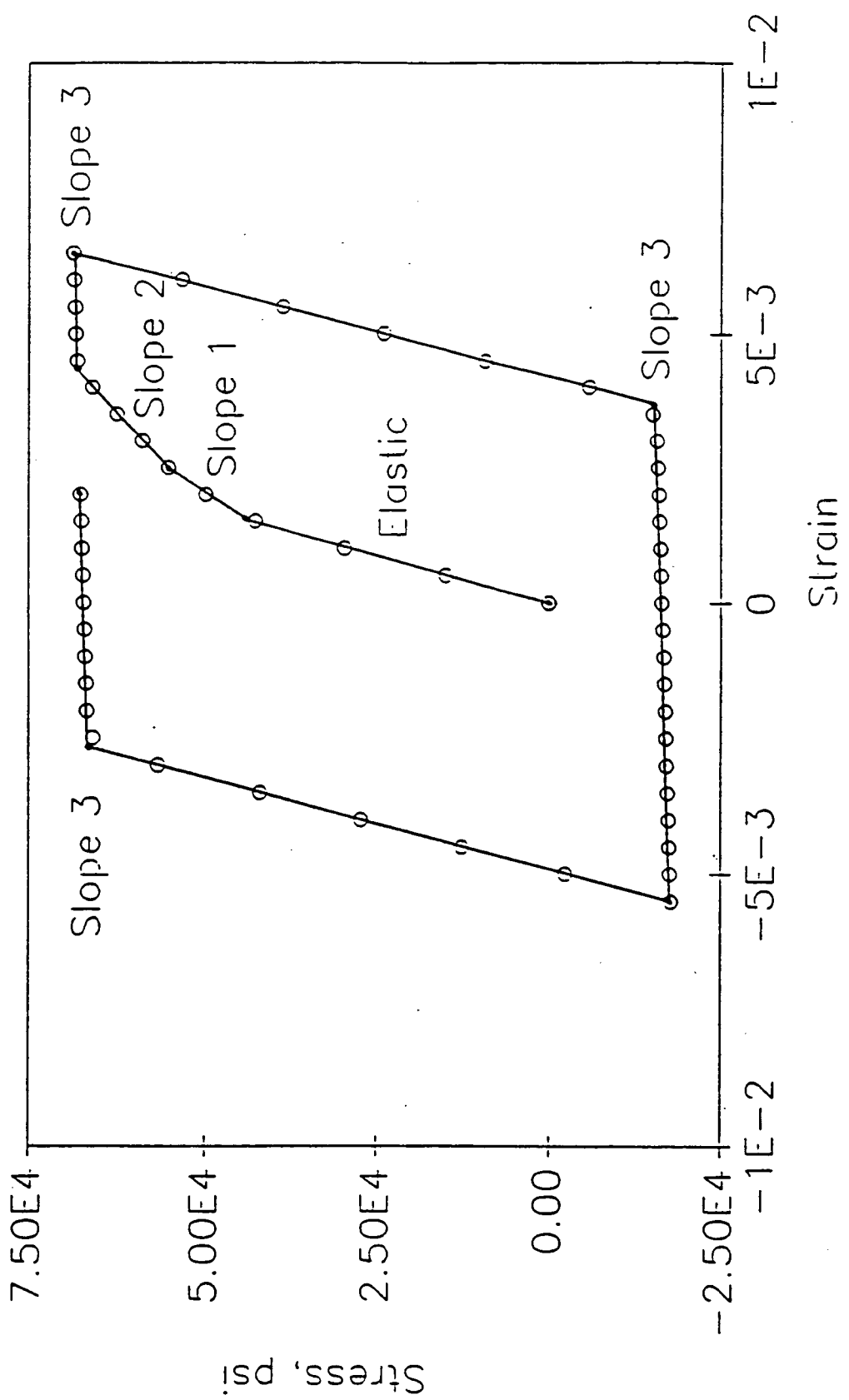
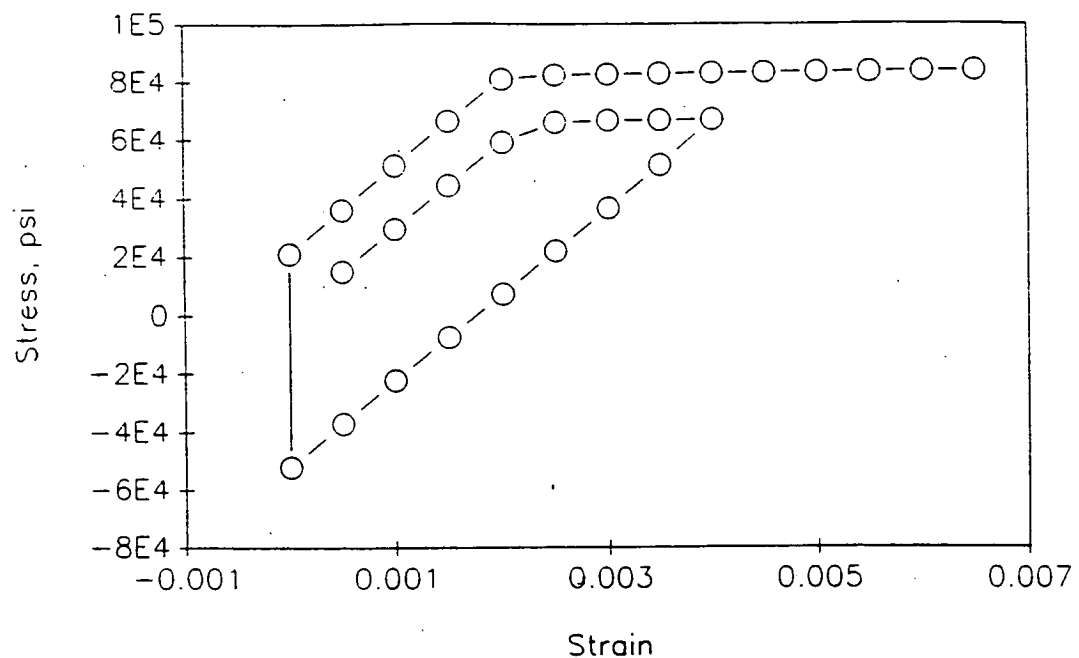


Figure 1.2.6: Axial stress-strain response of the four-node plane-stress model using a multilinear kinematic-hardening rule.

One Element Model  
Temperature Decrease Before Reloading



One Element Model  
Temperature Increase Before Reloading

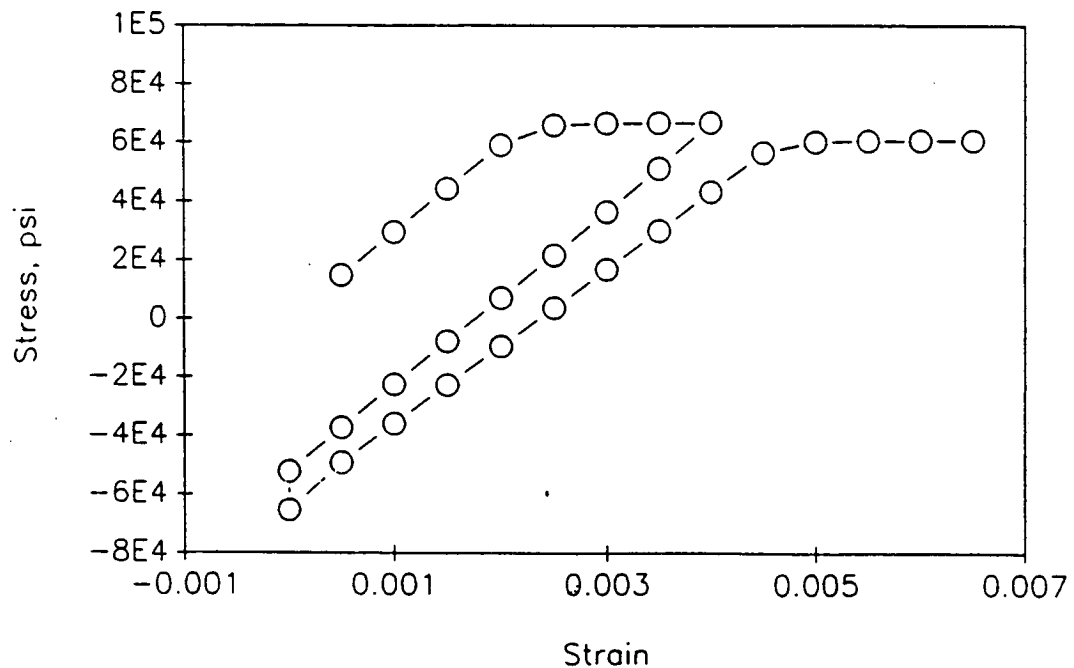
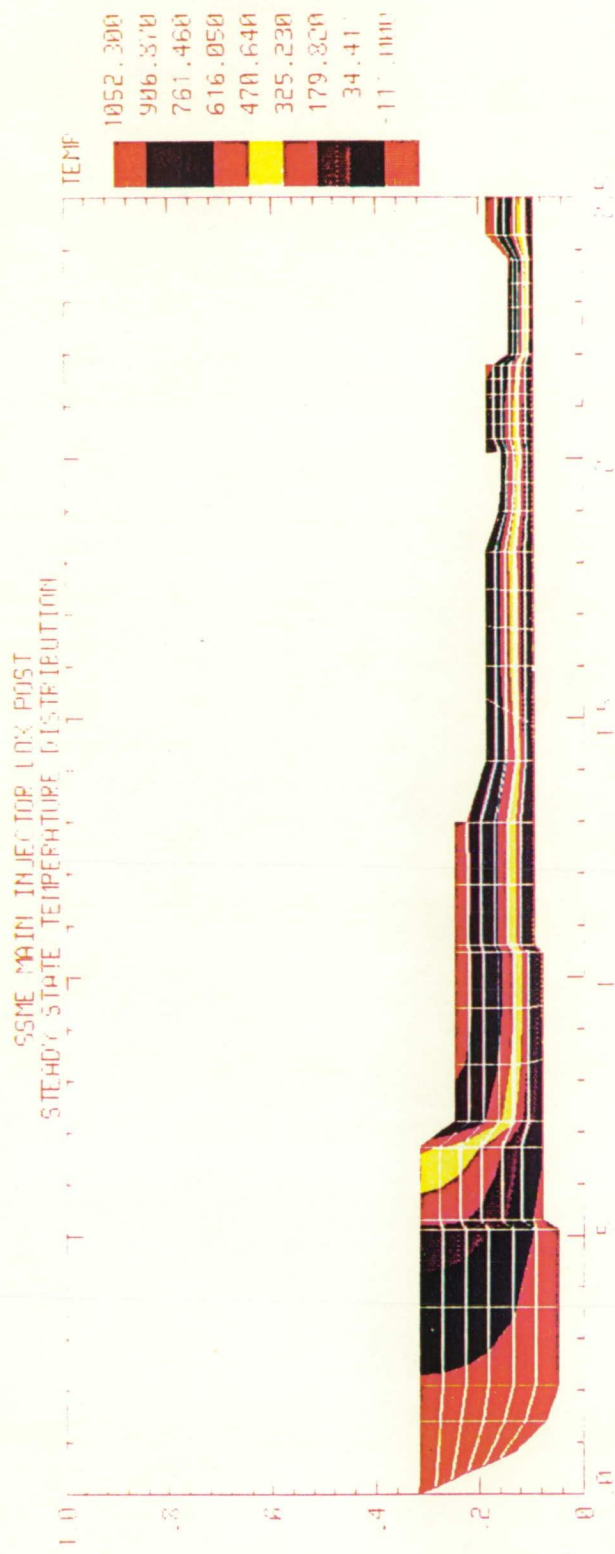


Figure 1.2.7: Axial stress-strain response of the four-node plane-stress model subject to mechanical loading coupled with sudden changes in temperature.



ORIGINAL PAGE  
COLOR PHOTOGRAPH

ORIGINAL PAGE IS  
OF POOR QUALITY

Figure 1.2.8: Temperature distribution on the LOX post at steady state, in °F.

306479.

275130.

243780.

212431.

181082.

149732.

118383.

87034.

55684.

24335.

-7015.

-38364.

-69713.

-101063.

-132412.

-163762.

100P0, STRS

X

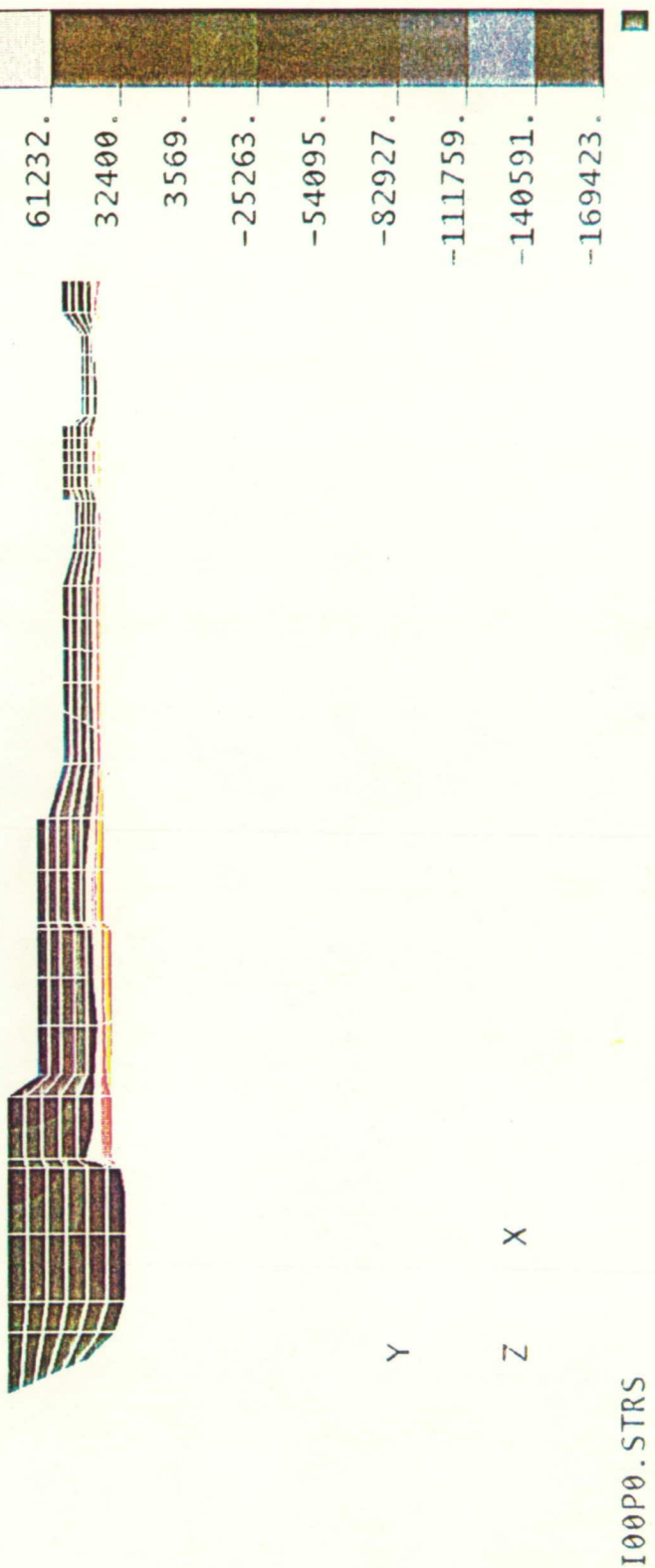
Z

Y

Figure 1.2.9: Axial stresses on the L0x post at steady state for an elastic model (psi).



Figure 1.2.10: Hoop stresses on the 1.0X post at steady state for an elastic model (psi).



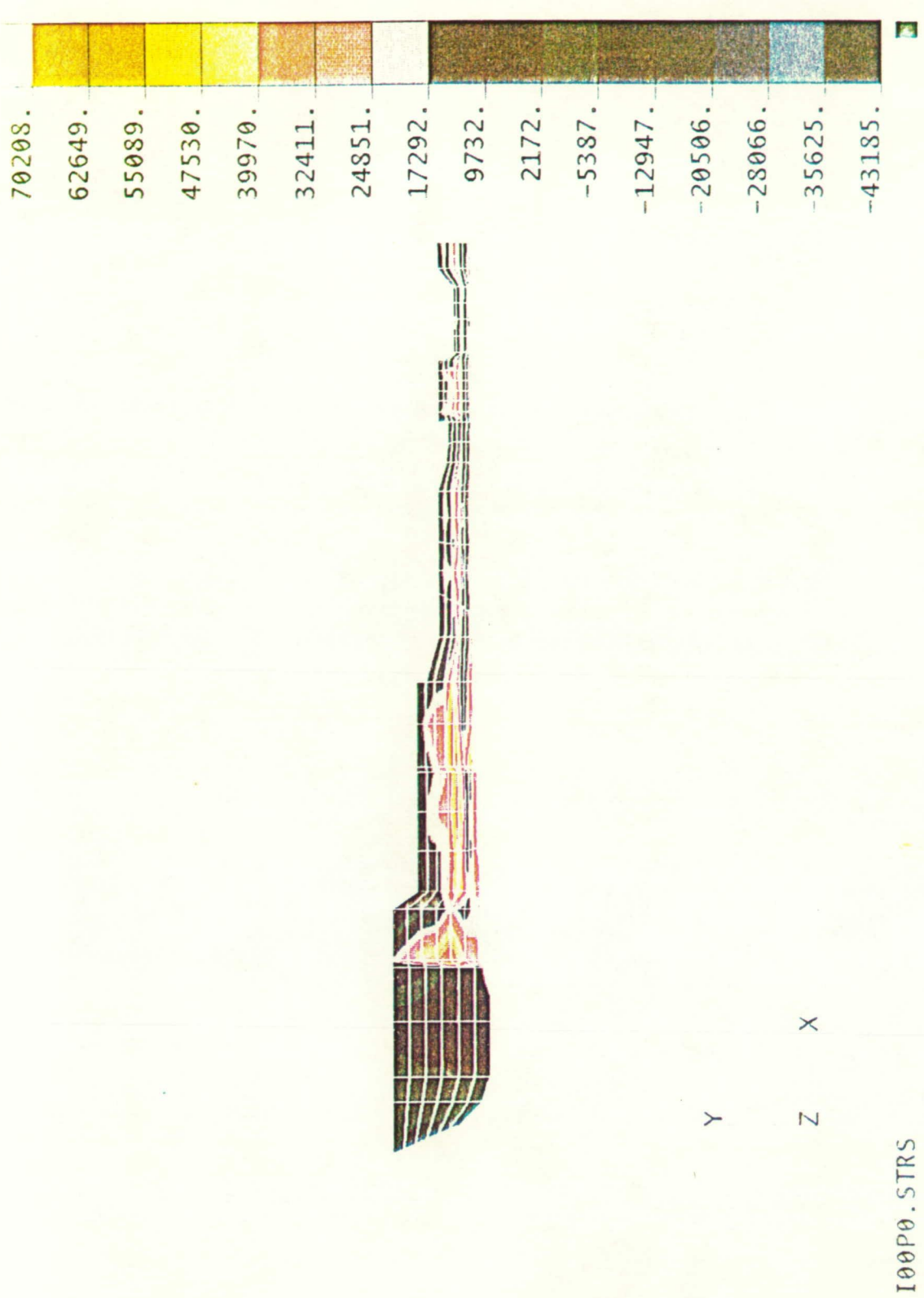


Figure 1.2.11: Radial stresses on the LOX post at steady state for an elastic model (psi).

Figure 1.2.12: Effective stresses on the lux post at steady state for an elastic model (psi).

X  
Y  
Z

231441.

216448.

201454.

186461.

171467.

156473.

141480.

126486.

111493.

96499.

81506.

66512.

51518.

36525.

21531.

6538.

## AXIAL STRESS

Nodes 78 - 84

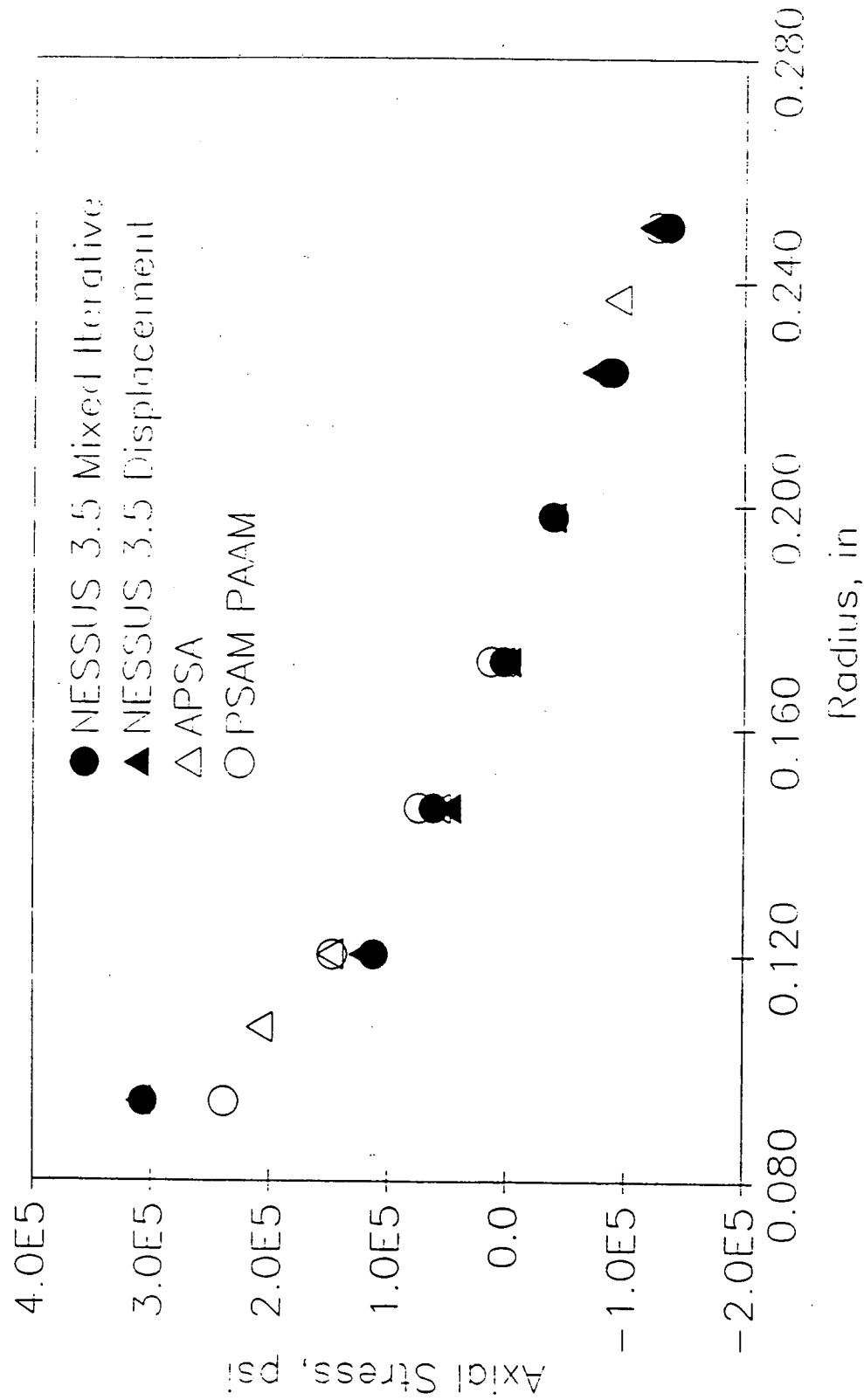


Figure 1.2.13: Comparison among the axial stresses of the LOX post at steady state calculated from NESSUS, APSA, and PAAAM along the cross section between nodes 78 and 84.

## HOOP STRESS

Nodes 78 – 84

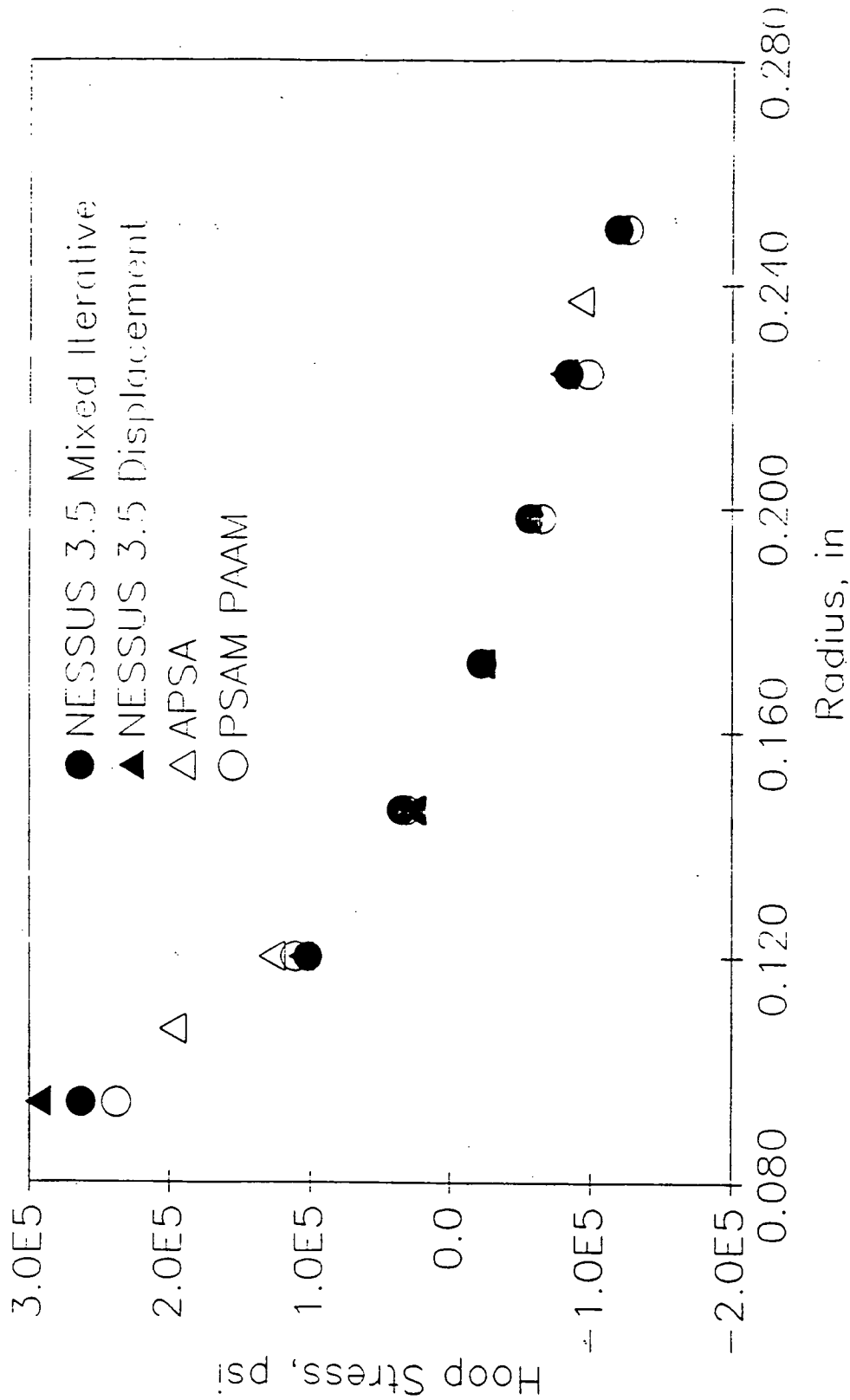


Figure 1.2.14: Comparison among the hoop stresses of the LOX post at steady state calculated from NESSUS, APSA, and PAM along the cross section between nodes 78 and 84.

## RADIAL STRESS

Nodes 78 84

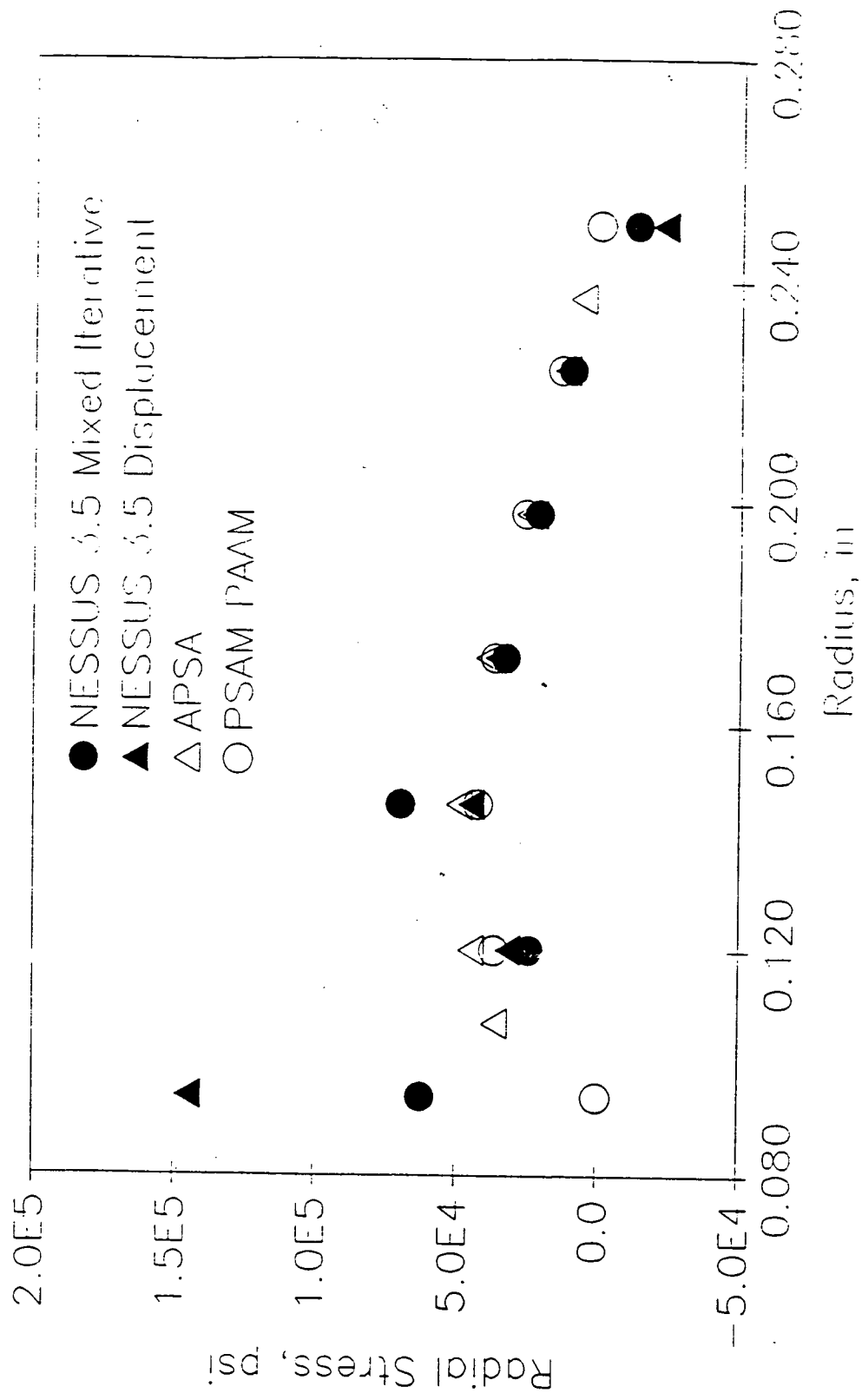


Figure 1.2.15: Comparison among the radial stresses of the LOX post at steady state calculated from NESSUS, APSA, and PAAM along the cross section between nodes 78 and 84.

AXIAL STRESS  
Nodes 117 - 122

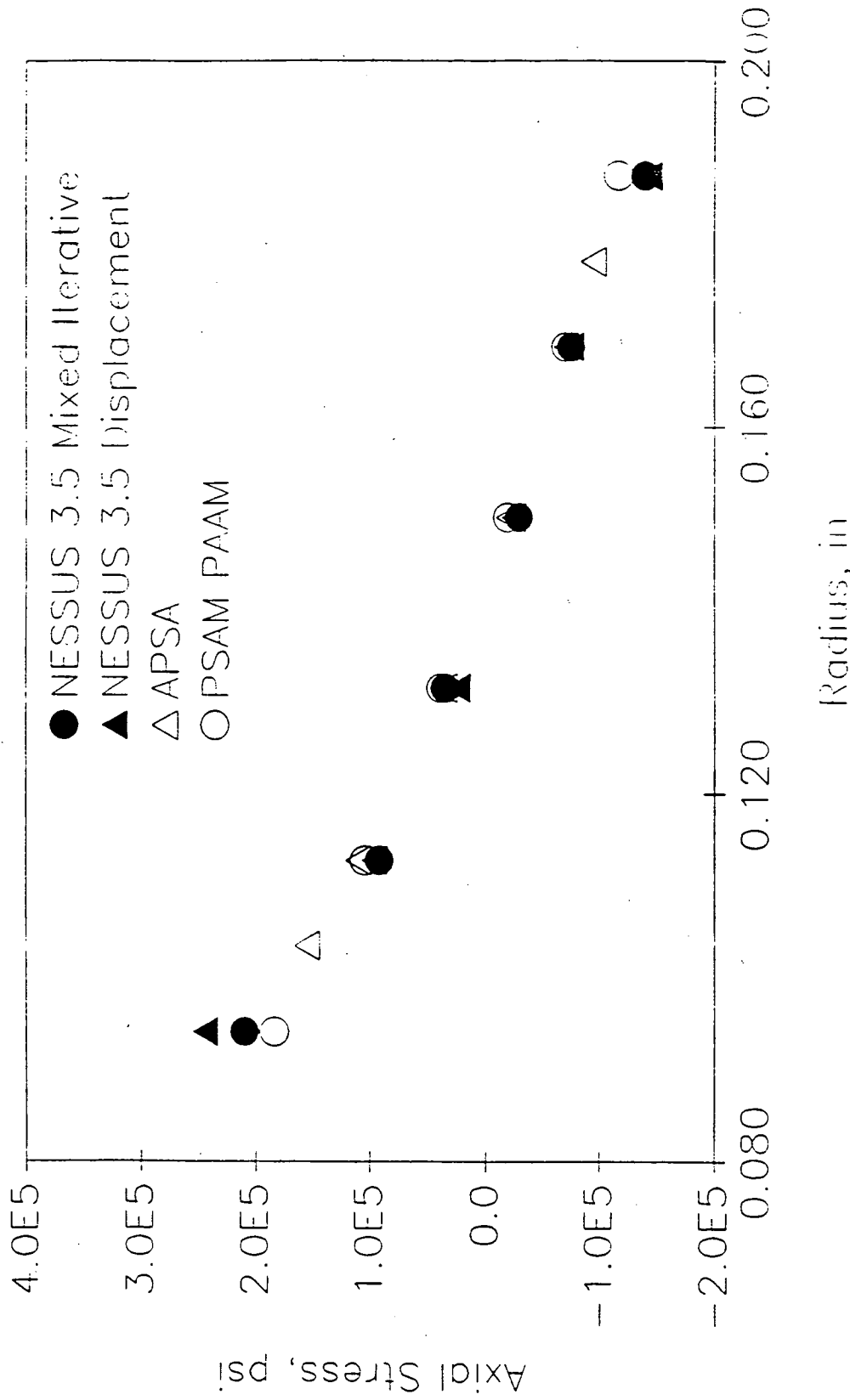


Figure 1.2.16: Comparison among the axial stresses of the LOX post at steady state calculated from NESSUS, APSA, and PAAAM along the cross section between nodes 117 and 122.

## HOOP STRESS

Nodes 117 - 122

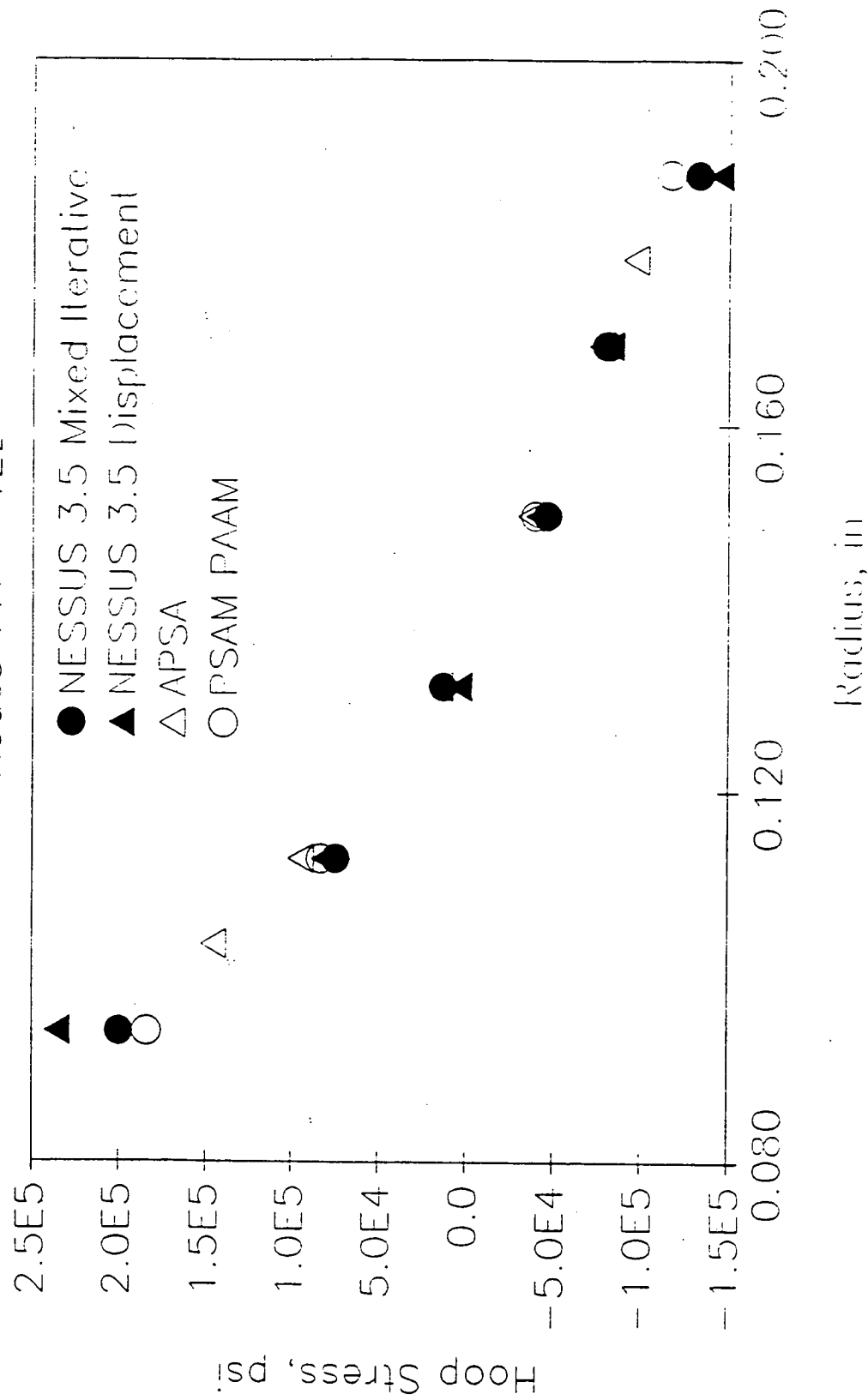


Figure 1.2.17: Comparison among the hoop stresses of the LOX post at steady state calculated from NESSUS, APSA, and PAAM along the cross section between nodes 117 and 122.

## RADIAL STRESS

Nodes 117 - 122

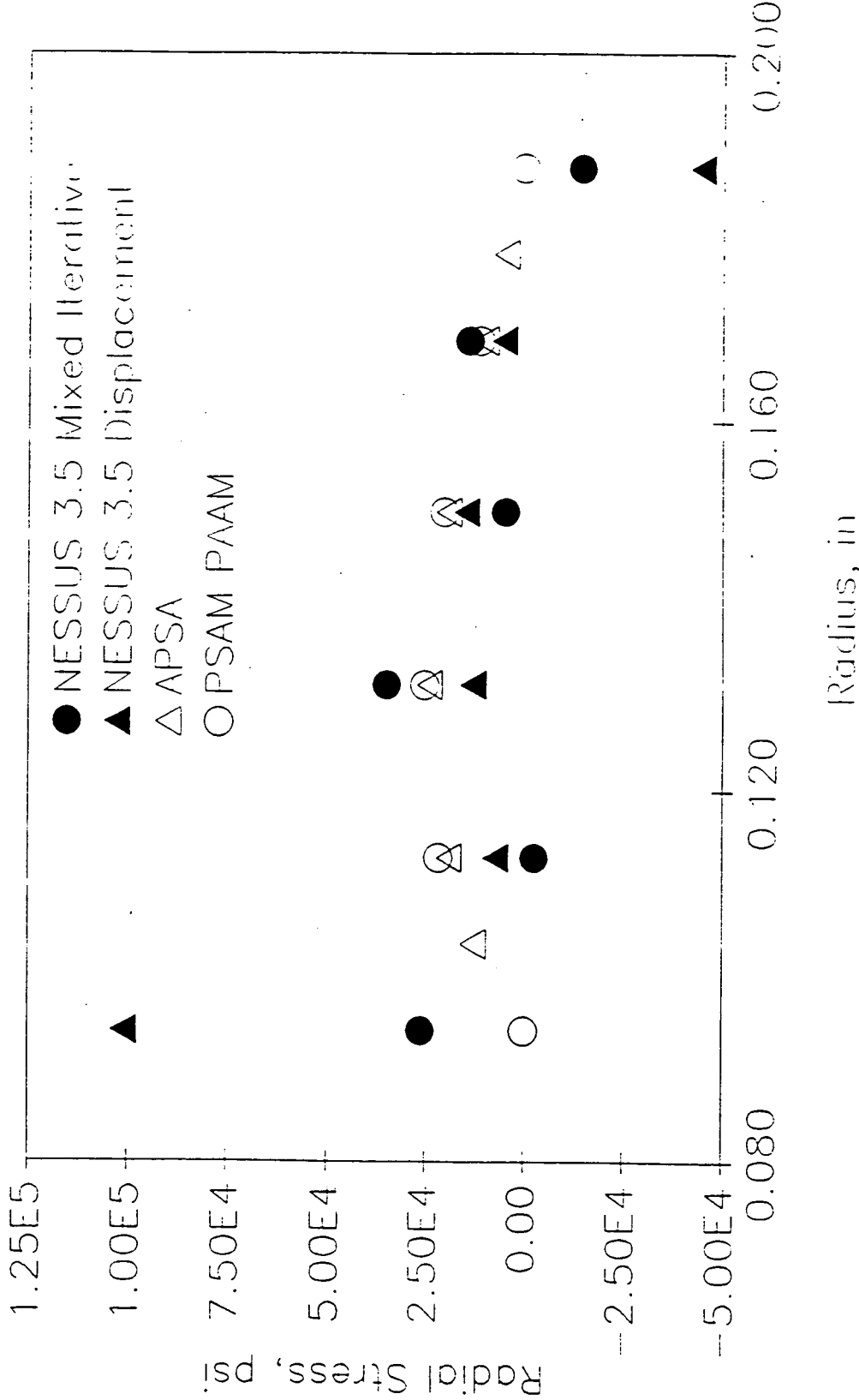


Figure 1.2.18: Comparison among the radial stresses of the 10x post at steady state calculated from NESSUS, APSA, and PAM along the cross section between nodes 117 and 122.

## Maximum Absolute Error in the Residuals

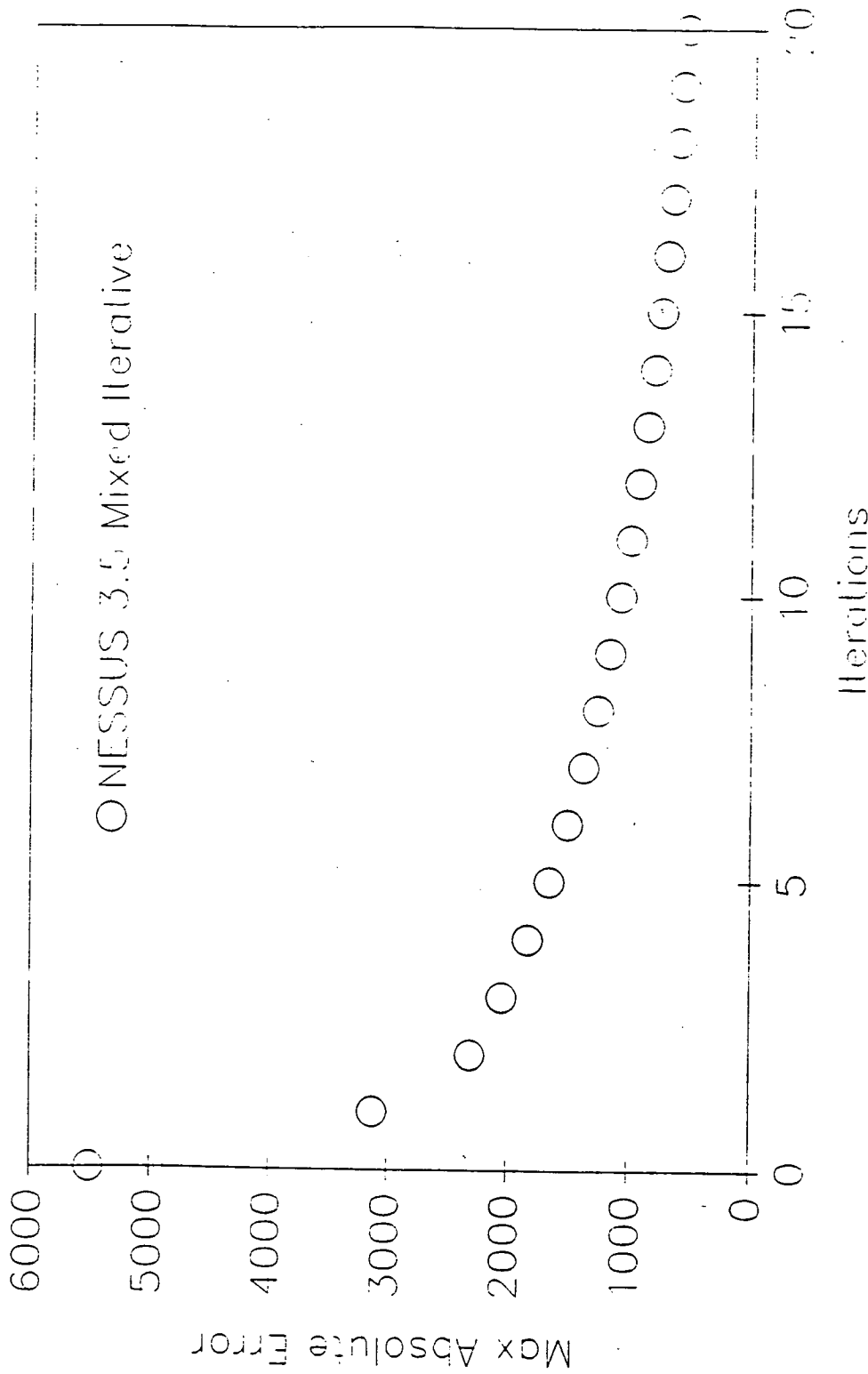


Figure 1.2.19: Maximum error in the residuals versus number of solution iterations for the elastic model of the 10X post at steady state.

ROCKWELL  
INTERNATIONAL  
STRUCTURAL DIVISION

MATERIALS  
PROPERTIES  
MANUAL

TYPICAL (PREDICTED)

H2

DATE-09-20-85

REFERENCE-6105-55 (MPR 85-0525)

6105.27.41.30-01

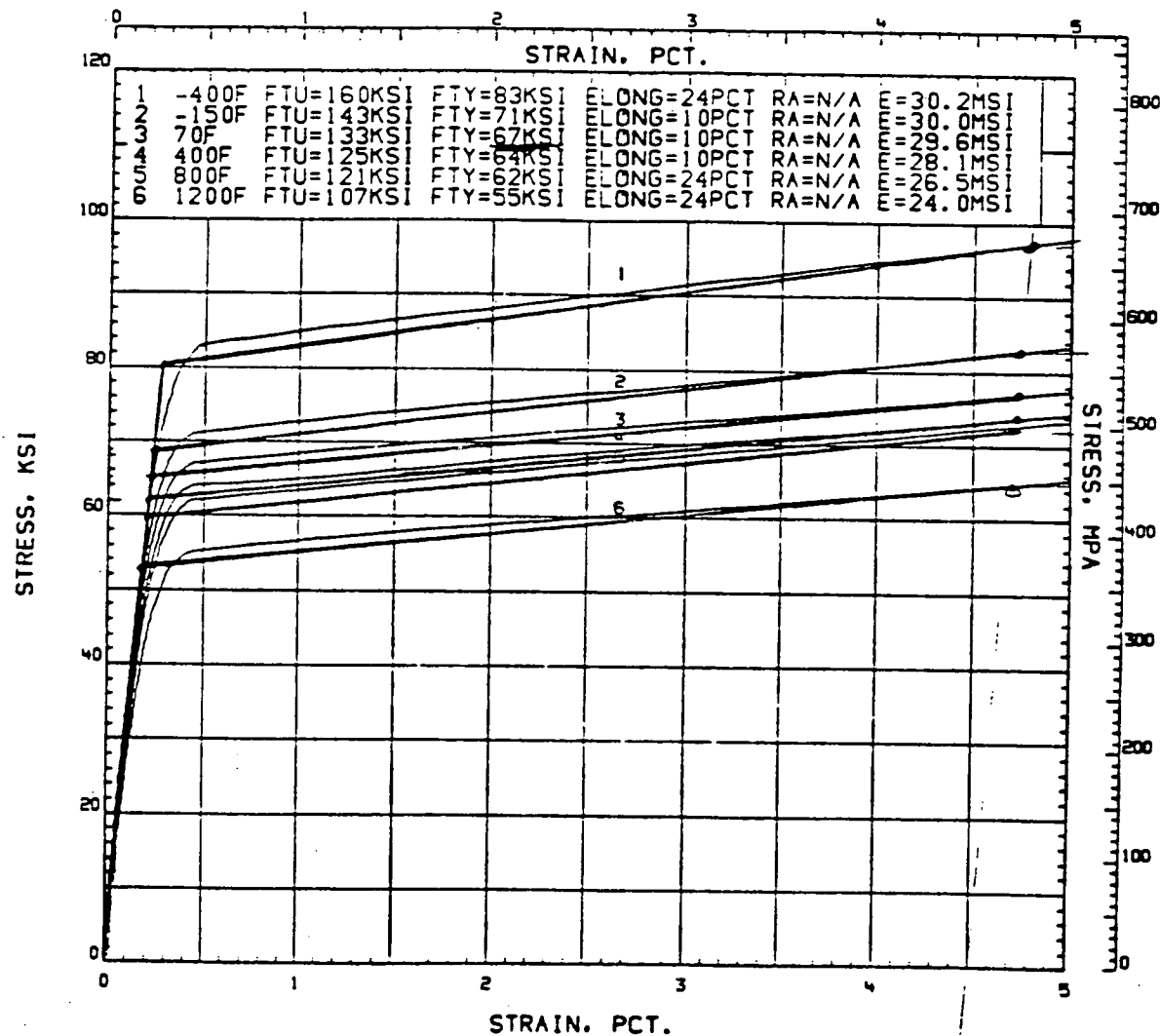
INCONEL 718

STRESS-STRAIN DIAGRAM

EBW, WROUGHT

AS-WELDED

SPEC. R80170-153.154



4th Edition

1-31-87

Figure 1.2.20: Temperature-dependent stress-strain curves for electron-beam-welded Inconel 718.

## Nodal Temperatures Over Engine Duty Cycle

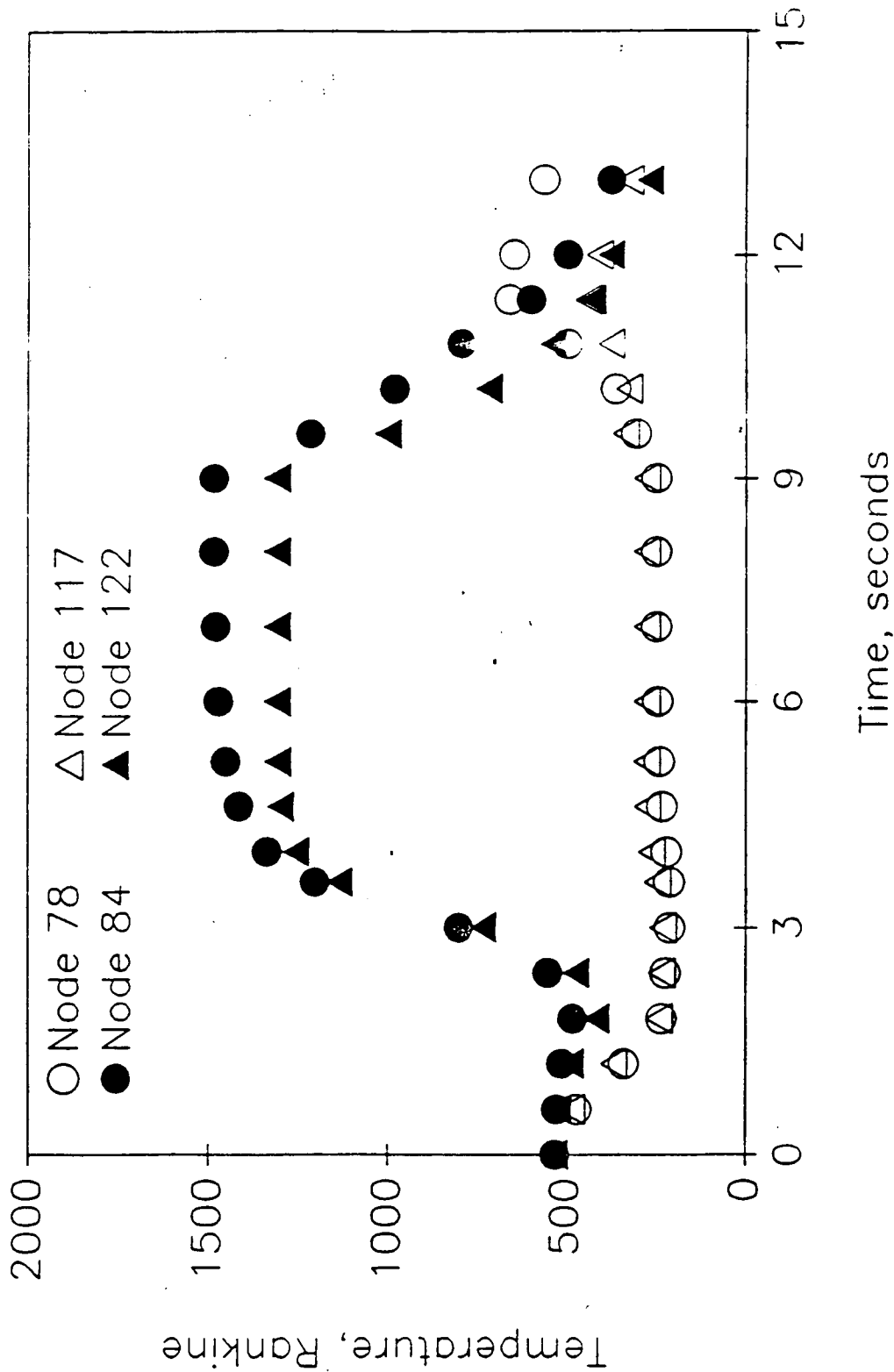


Figure 1.2.21: Temperatures of four nodes of the 1.0X post over the period of the duty cycle of the engine.

# LOX POST TRANSIENT DETERMINISTIC RESULTS

## Maximum Error in the Residual

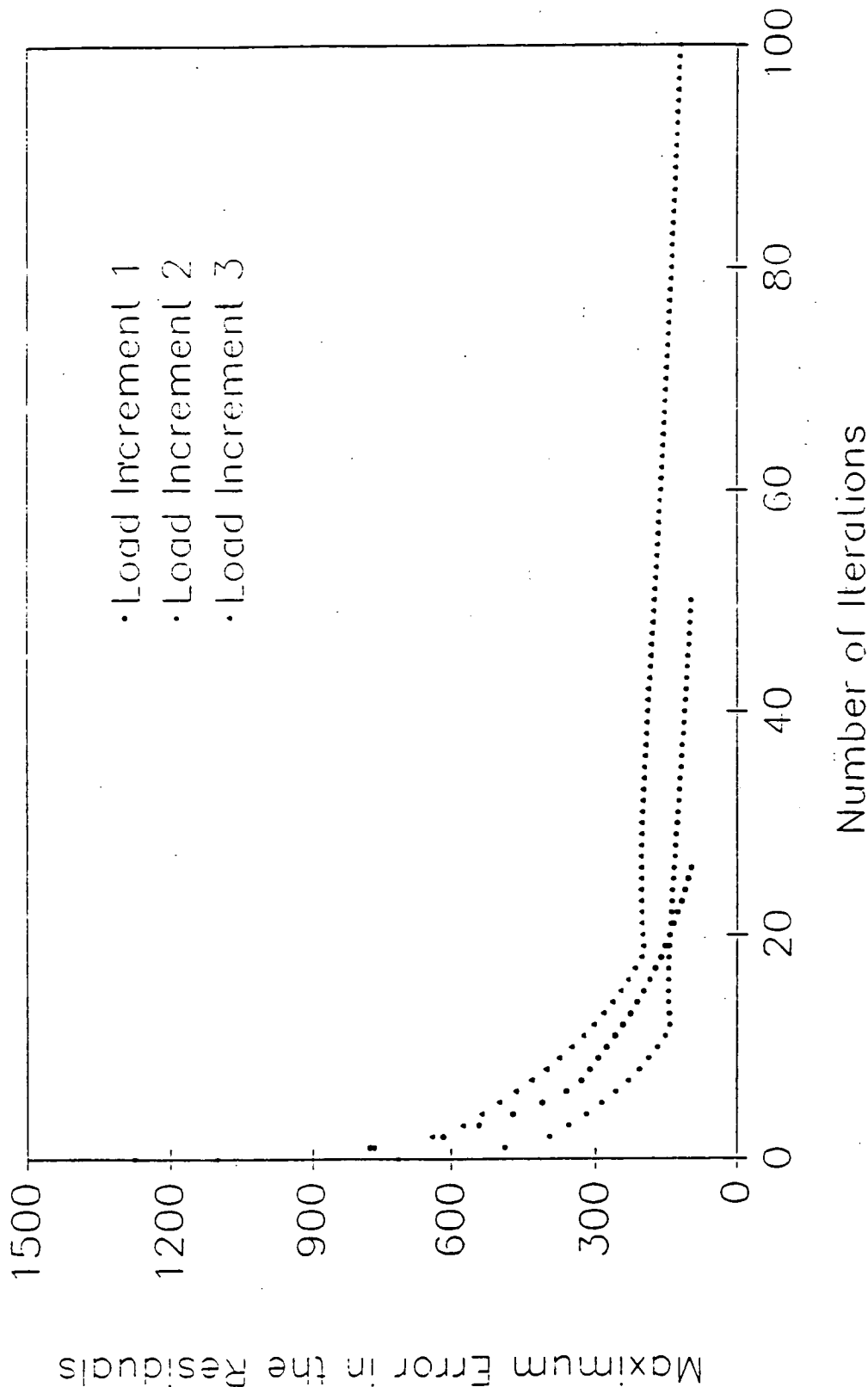


Figure 1.2.22: Maximum error in the residuals versus number of solution iterations for the LOX post at three load increments.

LOX Post Transient Deterministic Results  
Six Duty Cycles  
Node 78

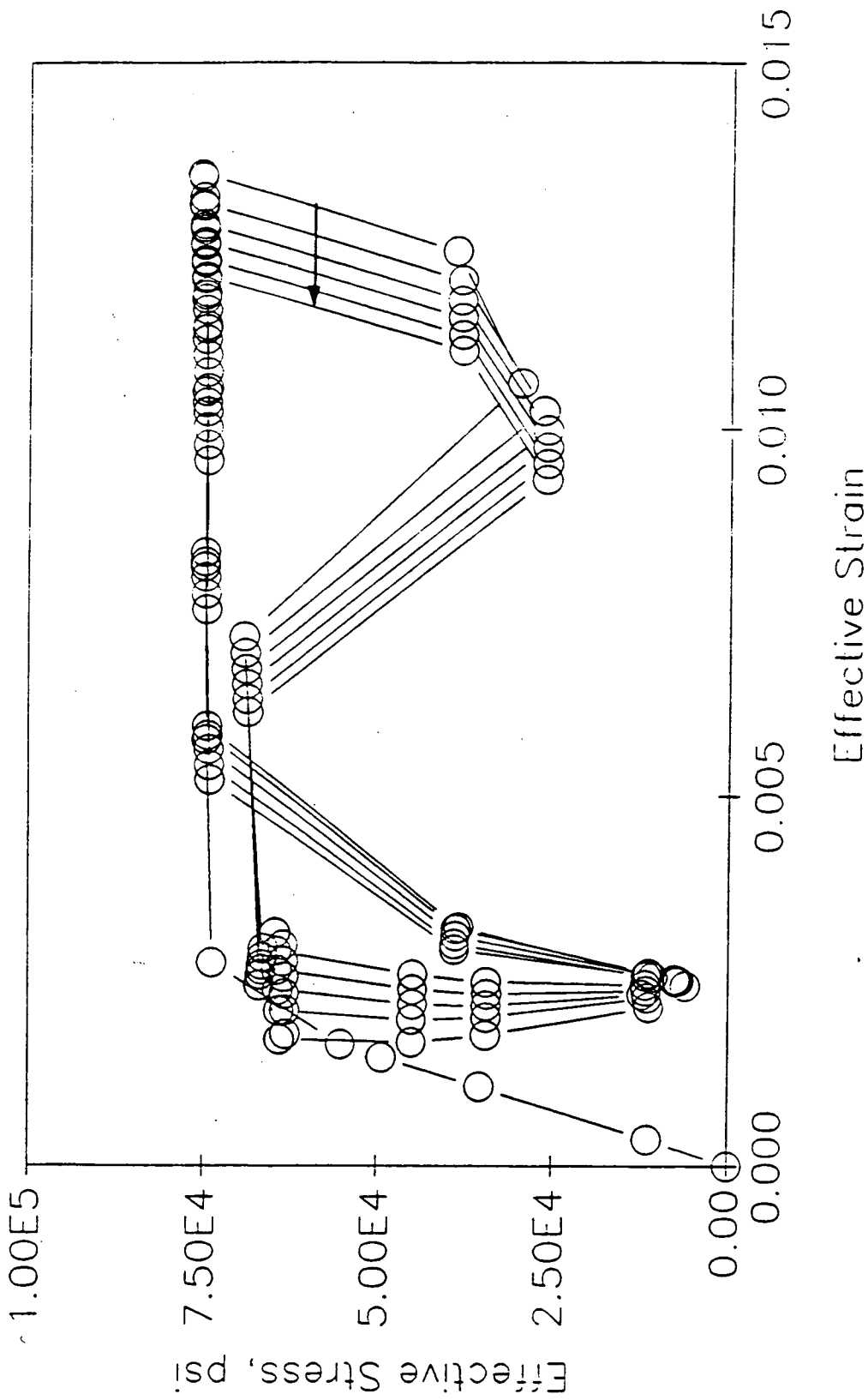


Figure 1.2.23: Effective stress-strain history of node 78 of the LOX post subjected to six duty cycles of the engine.

LOX Post Transient Deterministic Results  
Six Duty Cycles  
Node 78

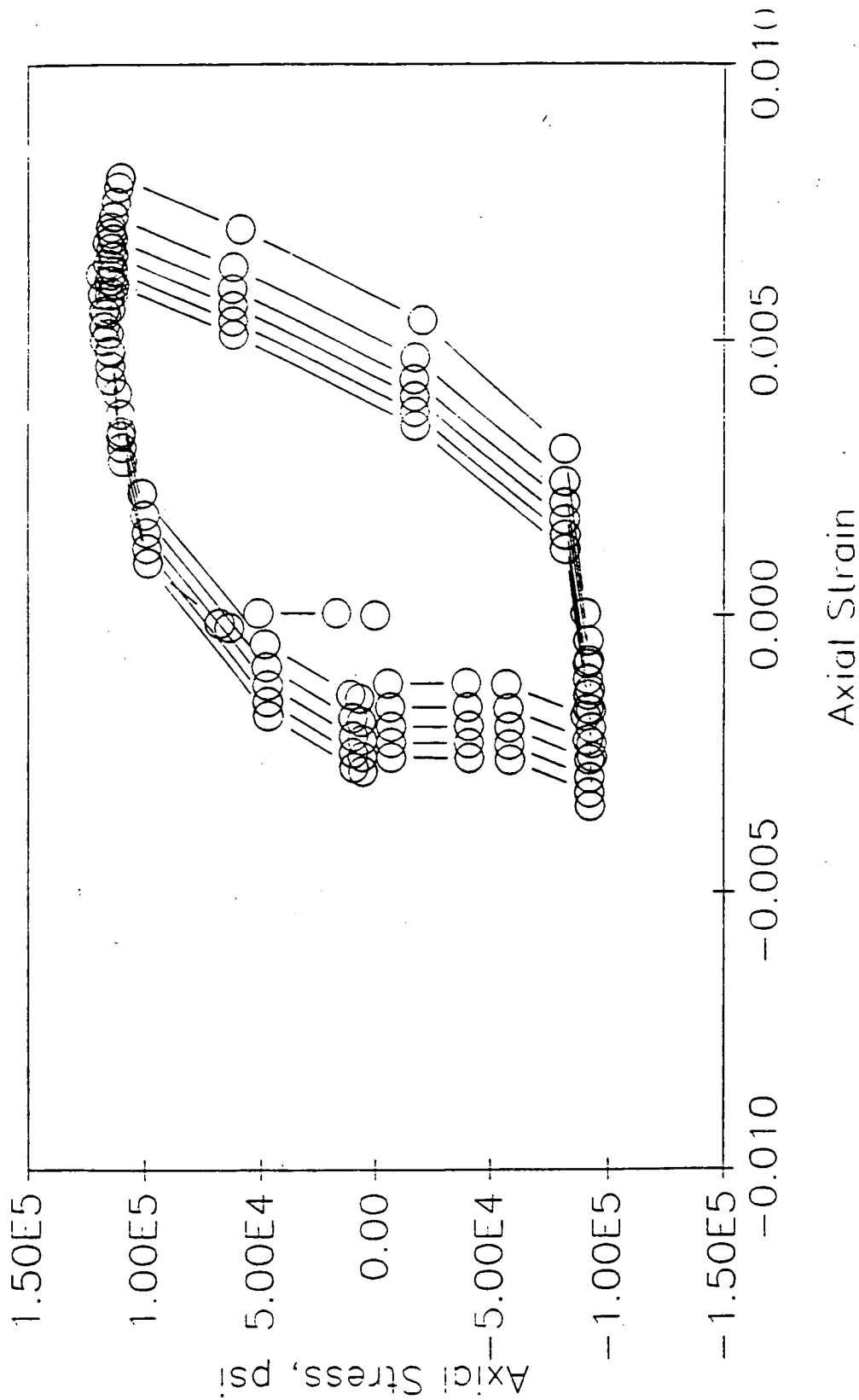


Figure 1.2.24: Axial stress-strain history of node 78 of the LOX post subjected to six duty cycles of the engine.

LOX Post Deterministic Results  
Six Duty Cycles  
Node 84

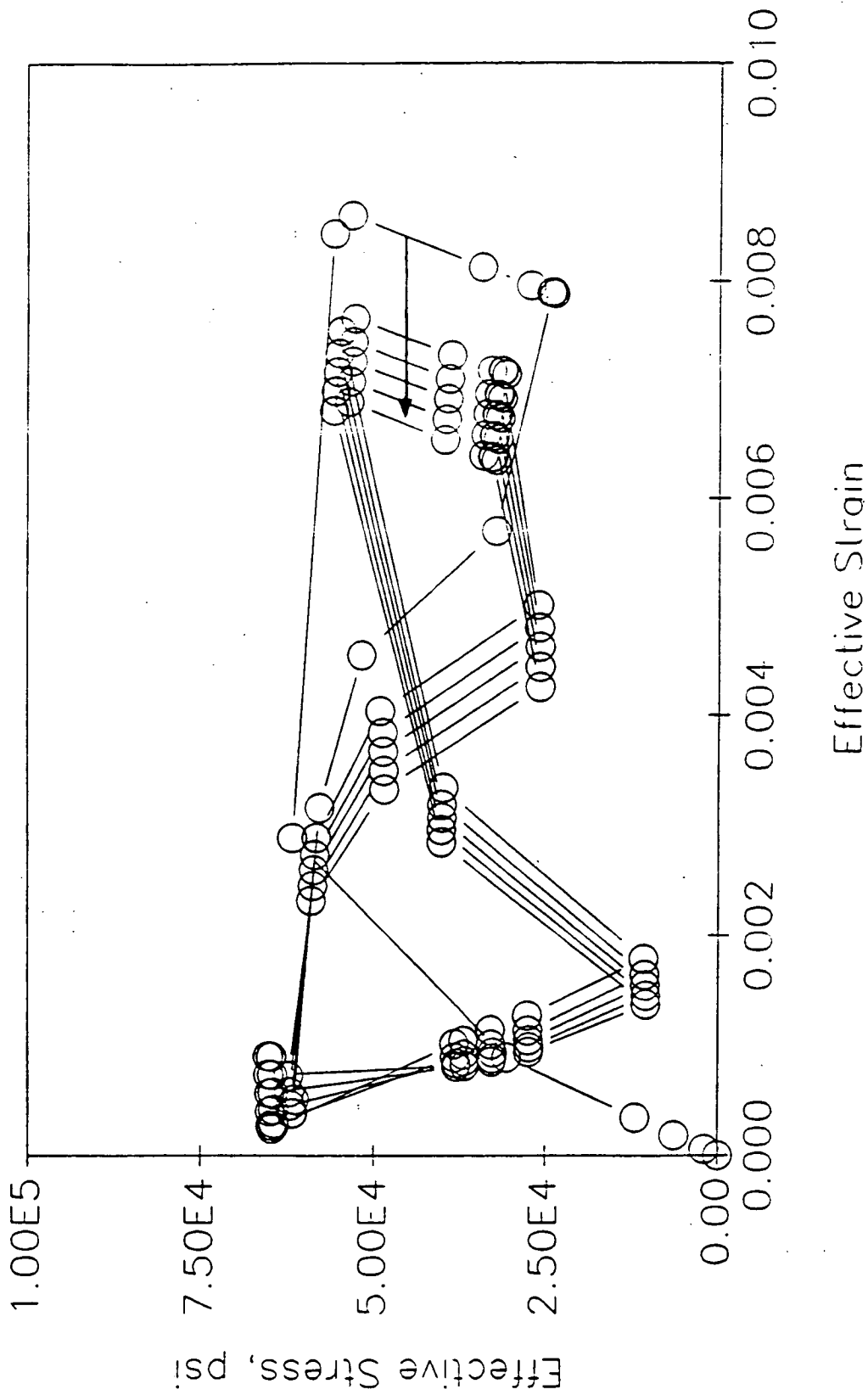


Figure 1.2.25: Effective stress-strain history of node 84 of the LOX post subjected to six duty cycles of the engine.

LOX Post Deterministic Results  
Six Duty Cycles  
Node 84

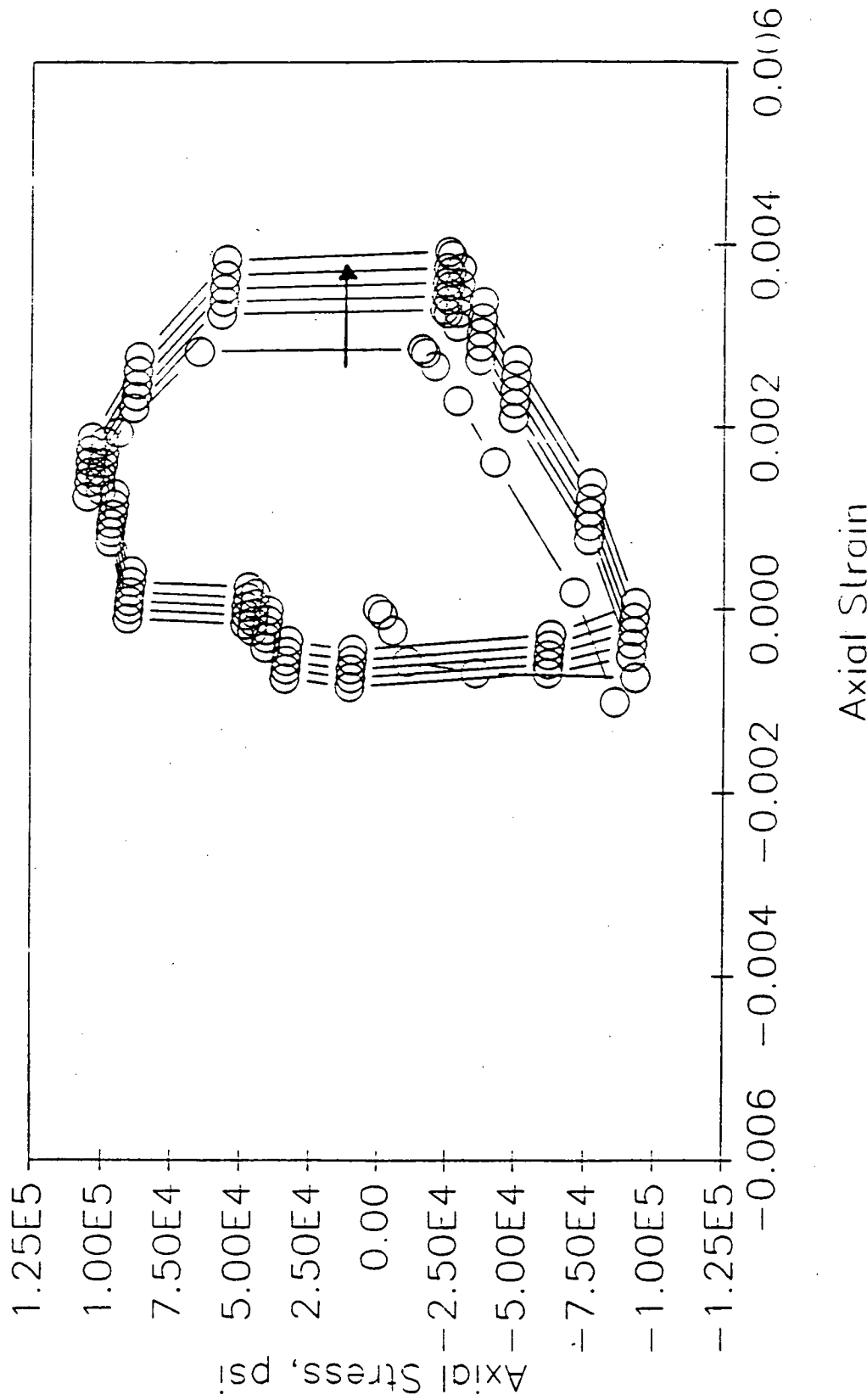


Figure 1.2.26: Axial stress-strain history of node 84 of the LOX post subjected to six duty cycles of the engine.

LOX Post Deterministic Results  
Six Duty Cycles  
Node 117

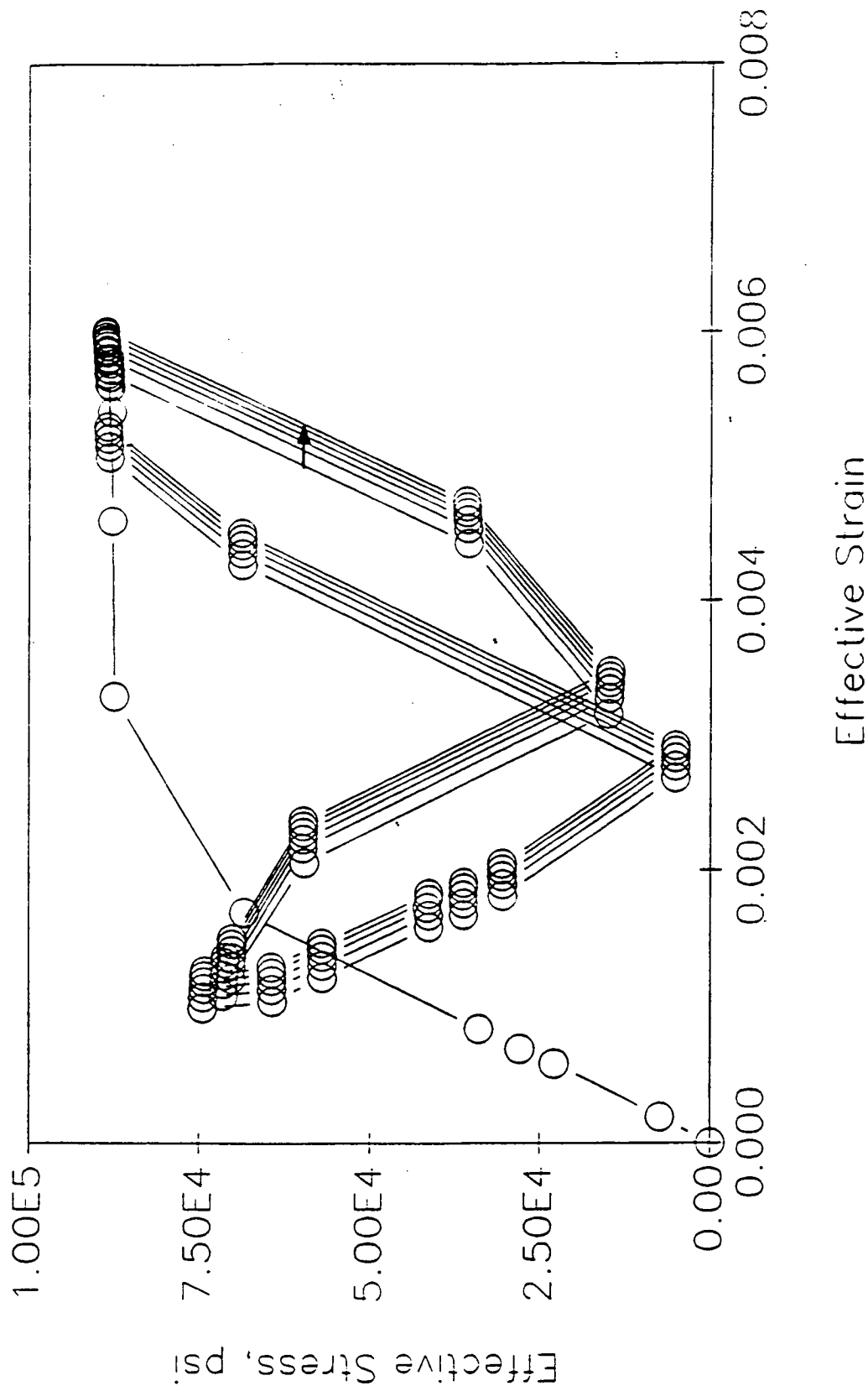


Figure 1.2.27: Effective stress-strain history of node 117 of the LOX post subjected to six duty cycles of the engine.

LOX Post Deterministic Results  
Six Duty Cycles  
Node 117

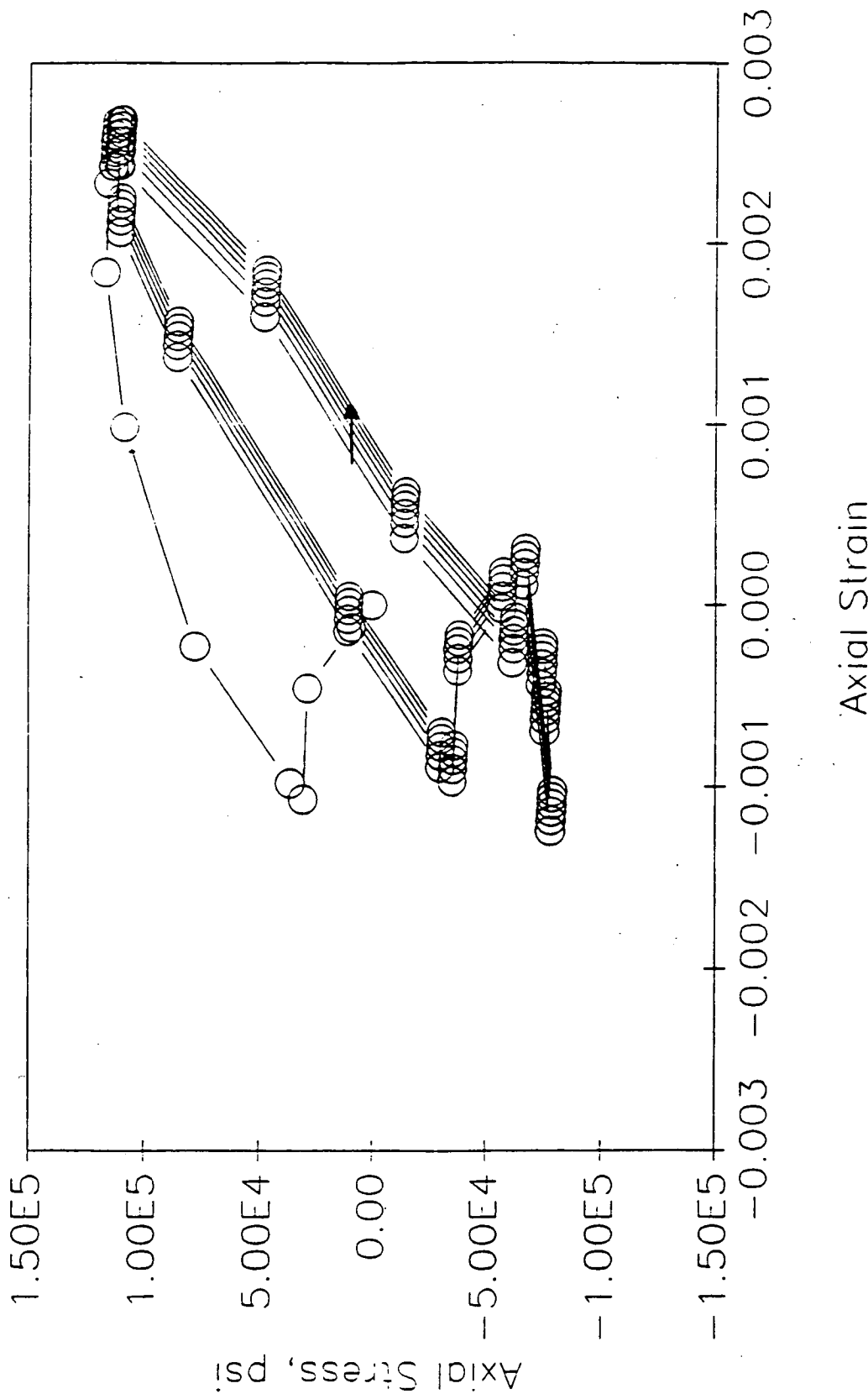


Figure 1.2.28: Axial stress-strain history of node 117 of the LOX post subjected to six duty cycles of the engine.

LOX Post Deterministic Results  
Six Duty Cycles  
Node 122

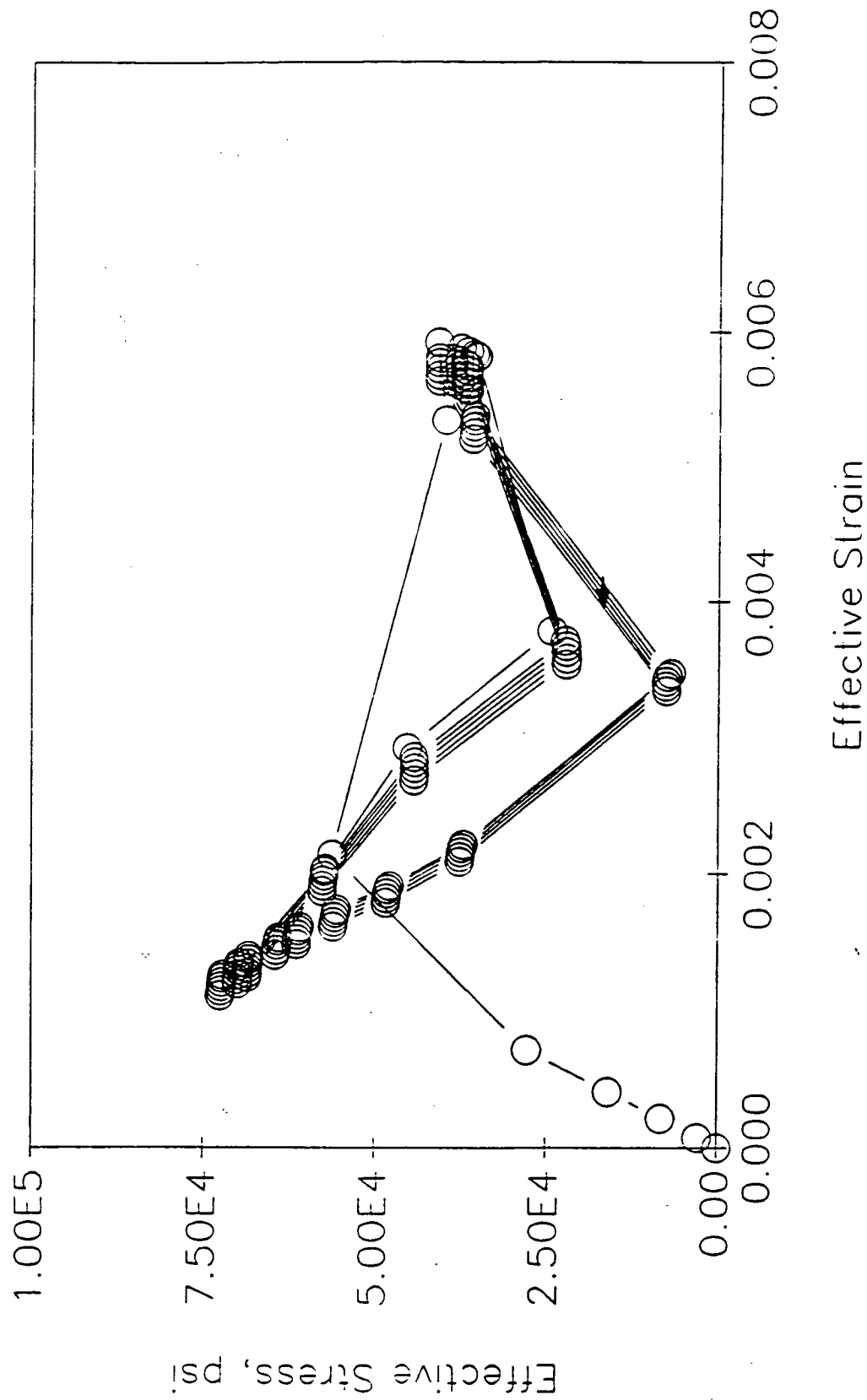


Figure 1.2.29: Effective stress-strain history of node 122 of the LOX post subjected to six duty cycles of the engine.

LOX Post Deterministic Results  
Six Duty Cycles  
Node 122

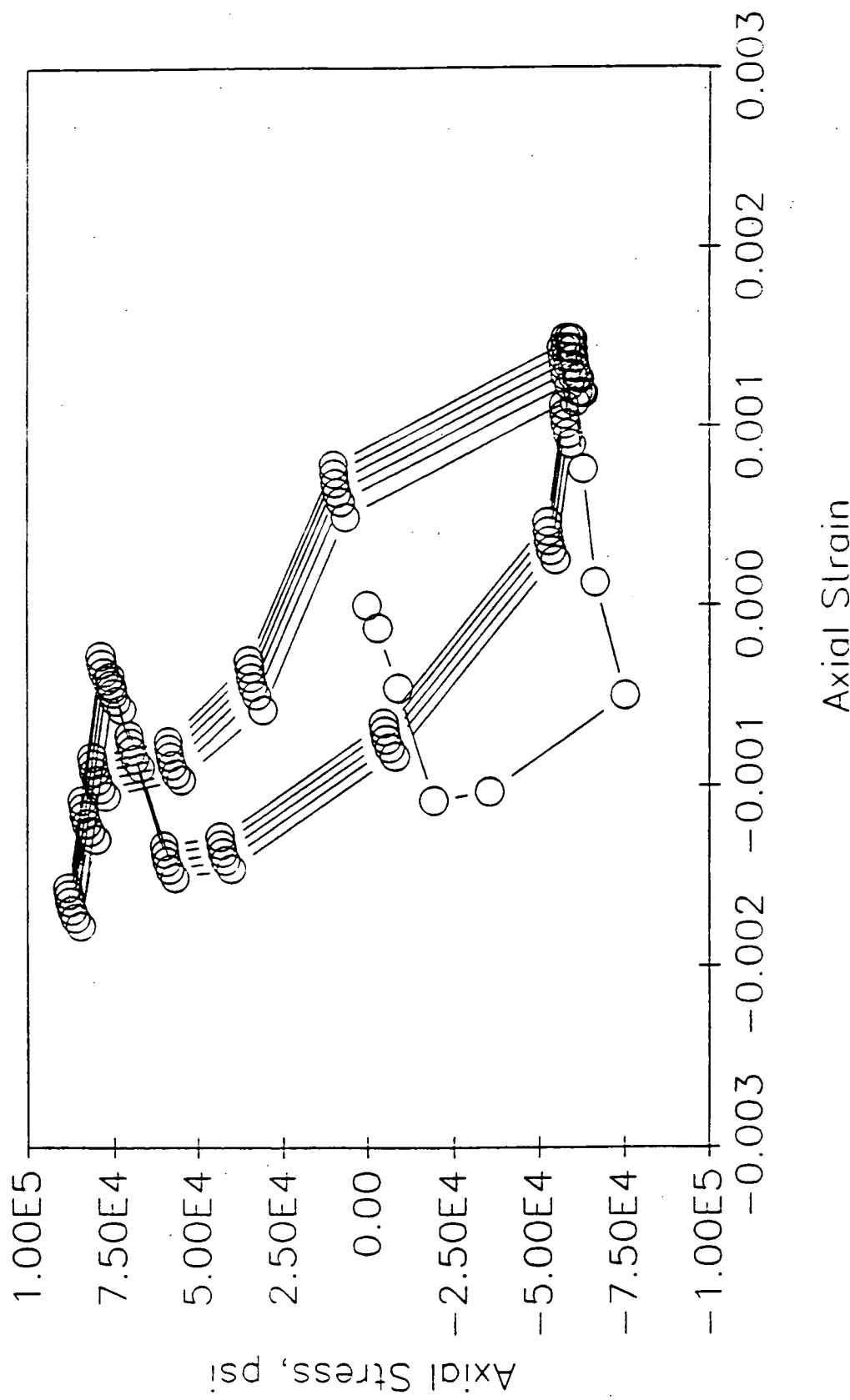


Figure 1.2.30: Axial stress-strain history of node 122 of the LOX post subjected to six duty cycles of the engine.

# LOX Post Deterministic Transient AP SAC Results

Element 61

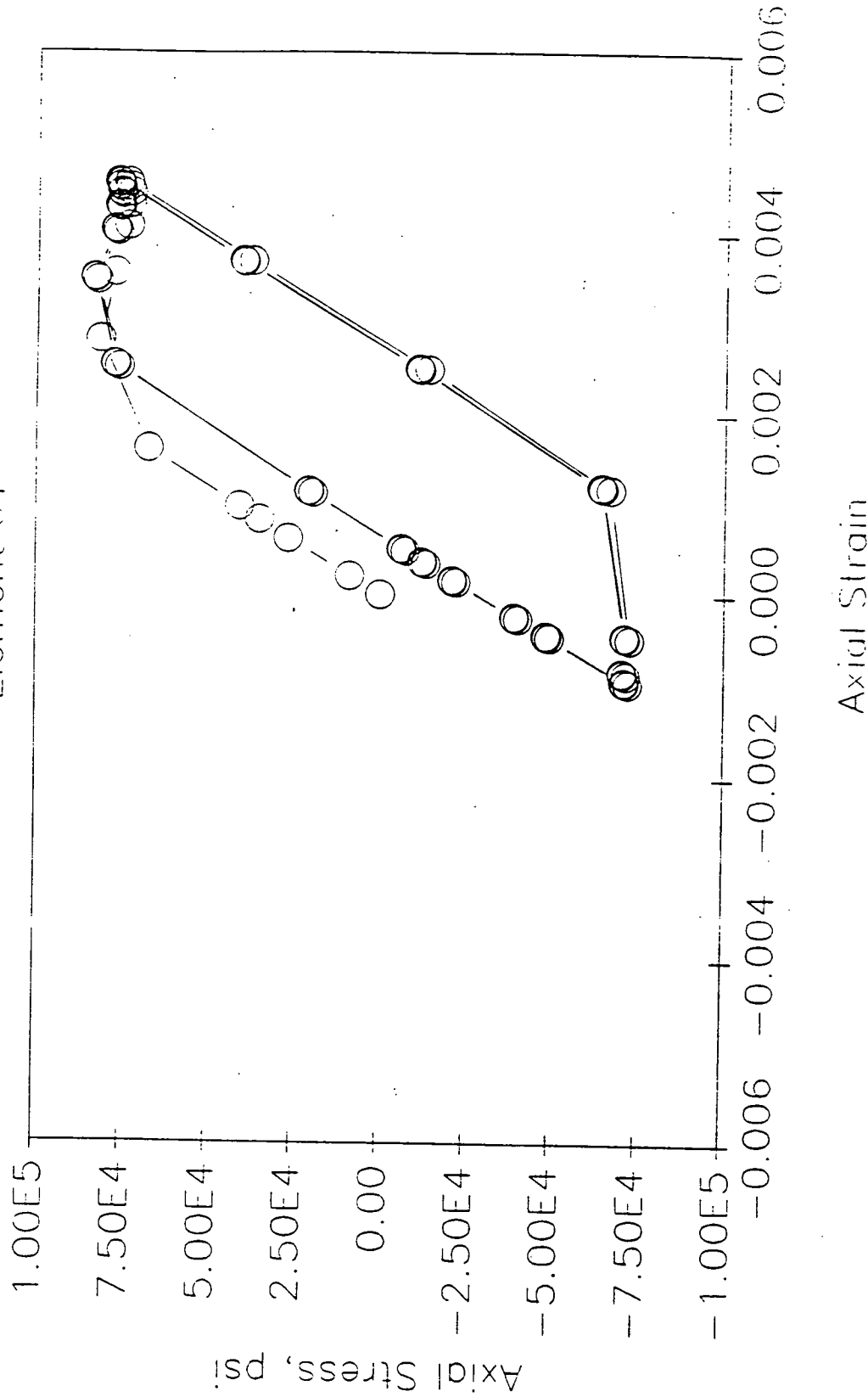


Figure 1.2.31: Axial stress-strain history of element 61 of the APSA solution subjected to six duty cycles of the engine.

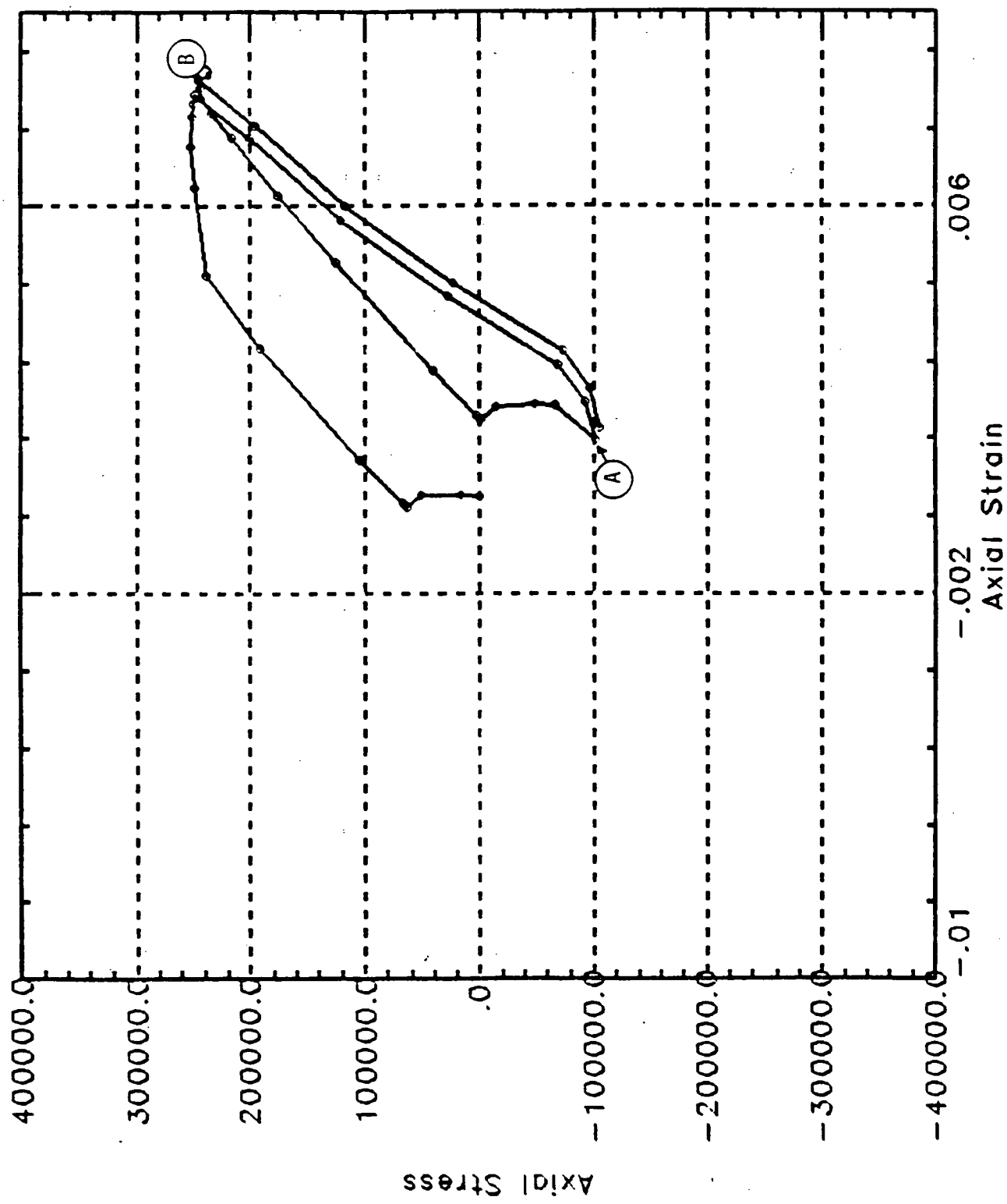


Figure 1.2.32: Axial stress-strain history of node 78 of the LOX post subjected to two duty cycles of the engine.

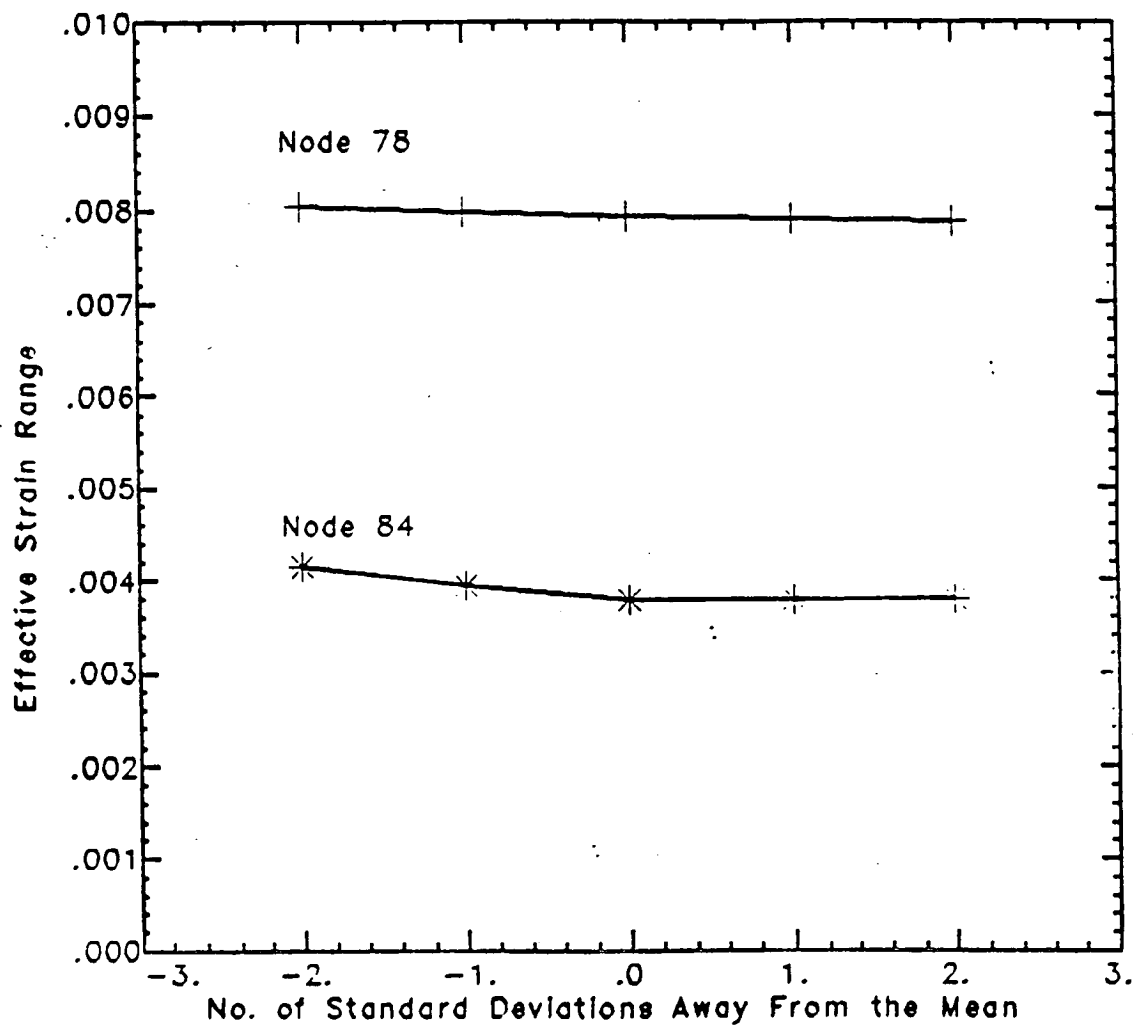


Figure 1.2.33: Effective strain range of the LOX post at nodes 78 and 84 as a function of variation in the yield stress of Inconel 718.

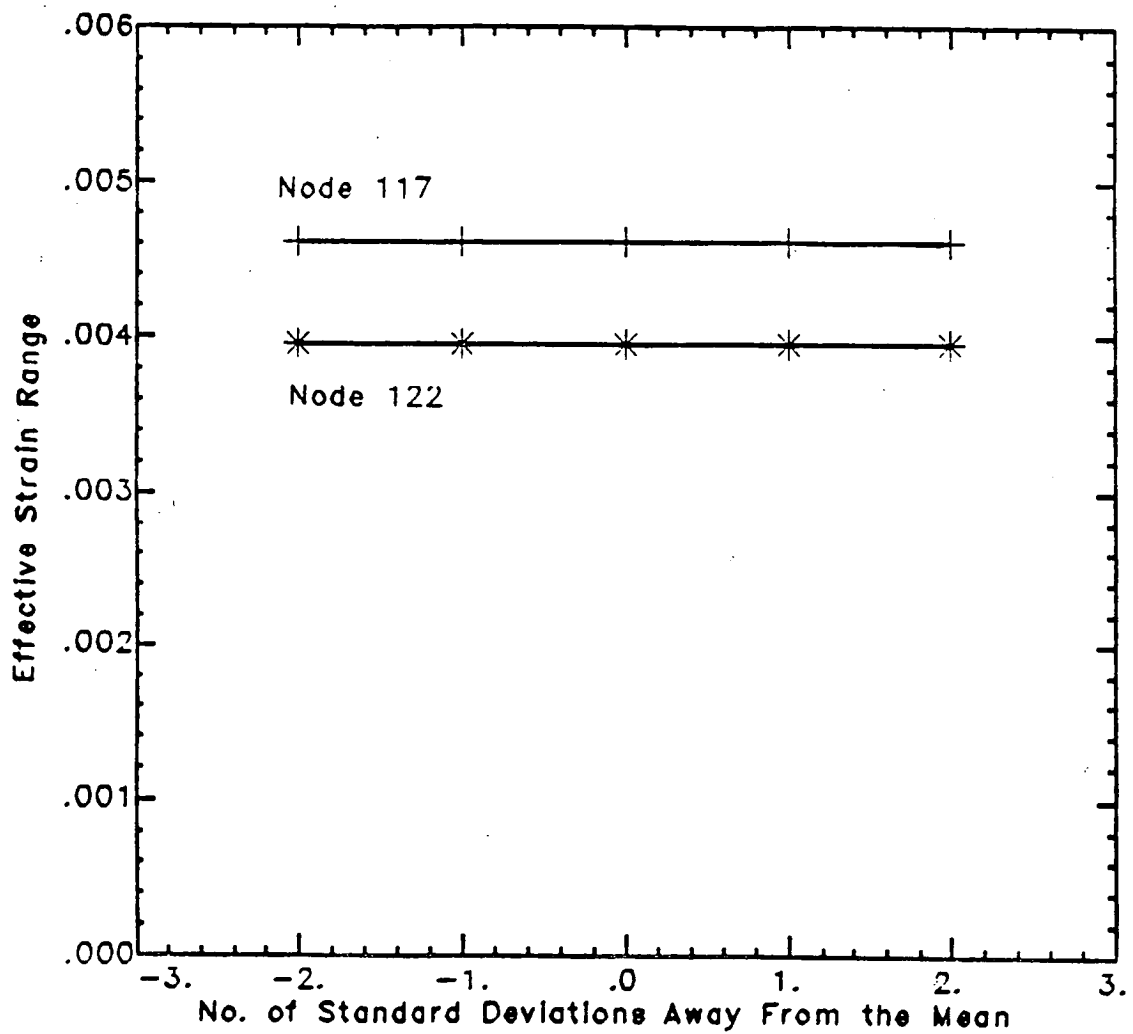


Figure 1.2.34: Effective strain range of the LOX post at nodes 117 and 122 as a function of variation in the yield stress of Inconel 718.

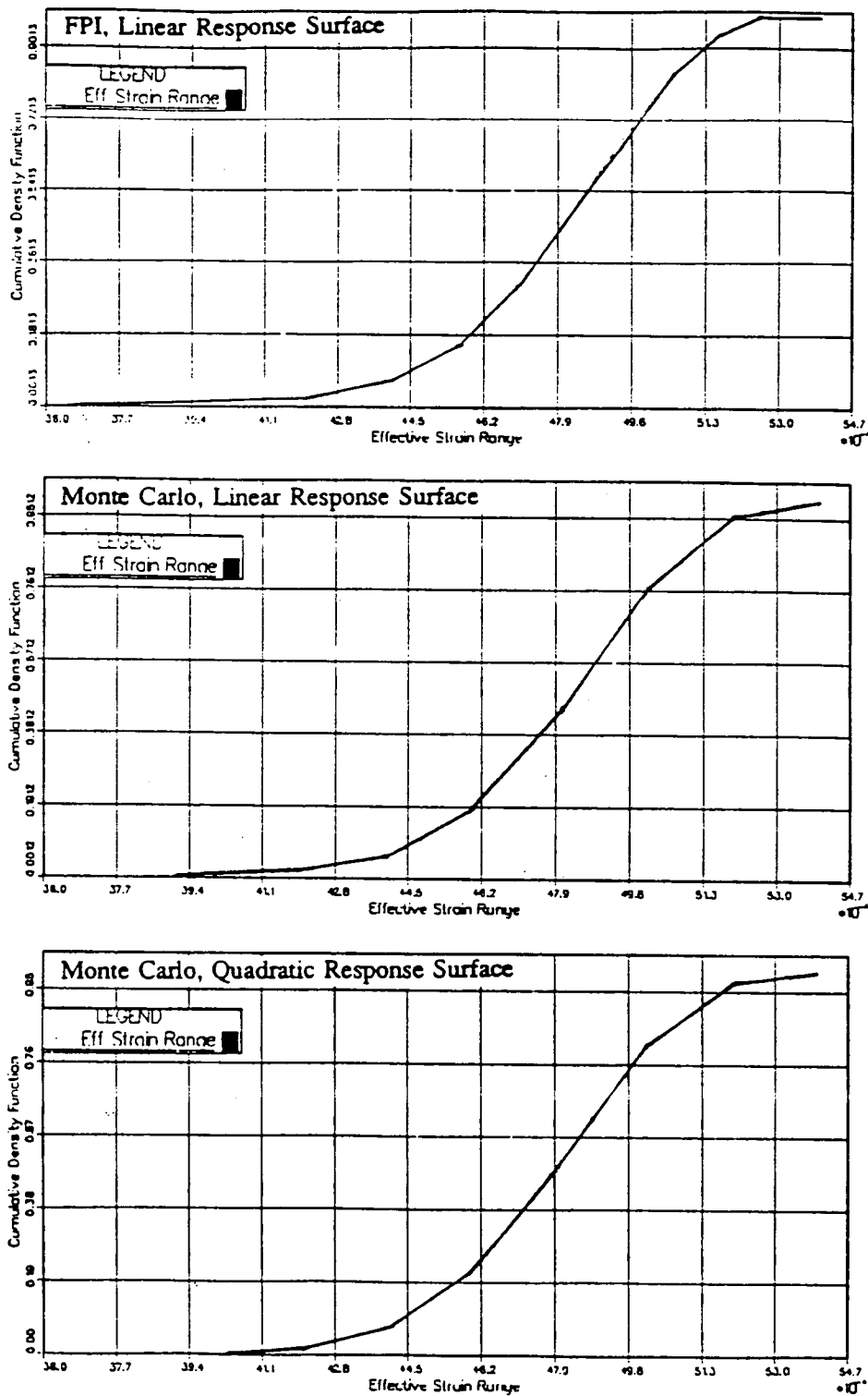
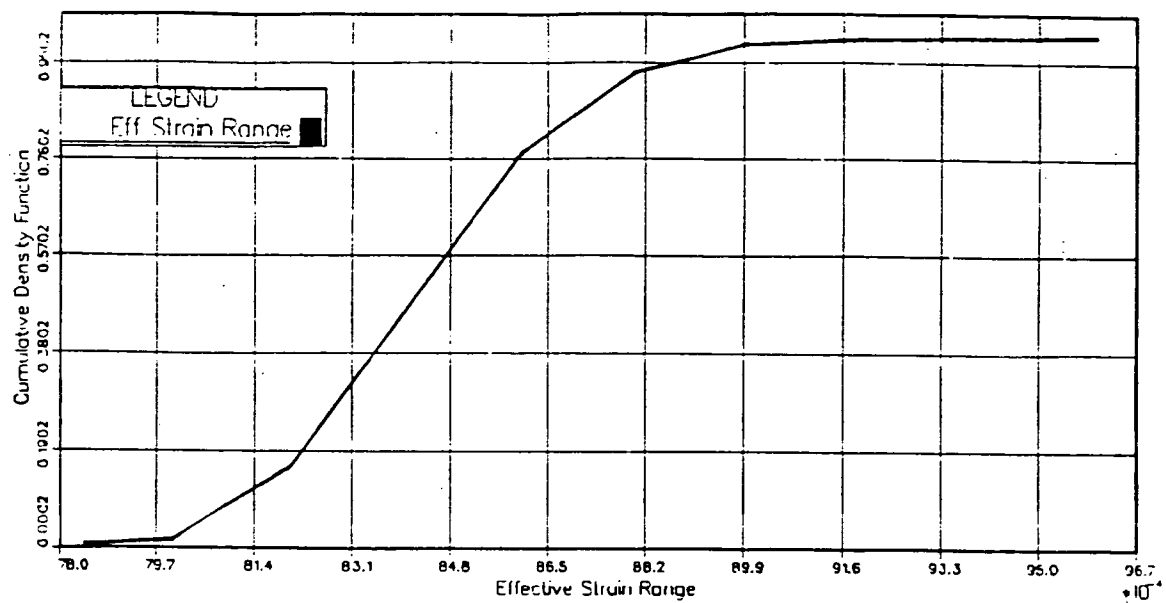


Figure 1.2.35: Cumulative density function of the effective strain range of the LOX post at node 56 calculated using the fast-probability-integration algorithm with a linear response surface (top) and the Monte Carlo simulation algorithm with a linear response surface (middle) and a quadratic response surface (bottom).

### Node 78



### Node 84

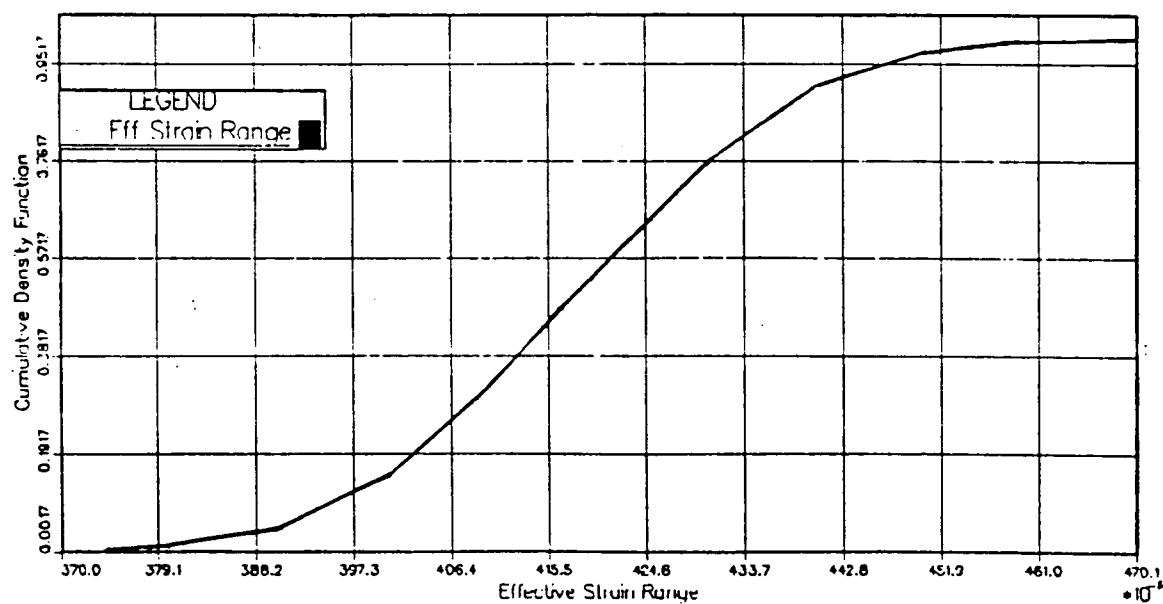
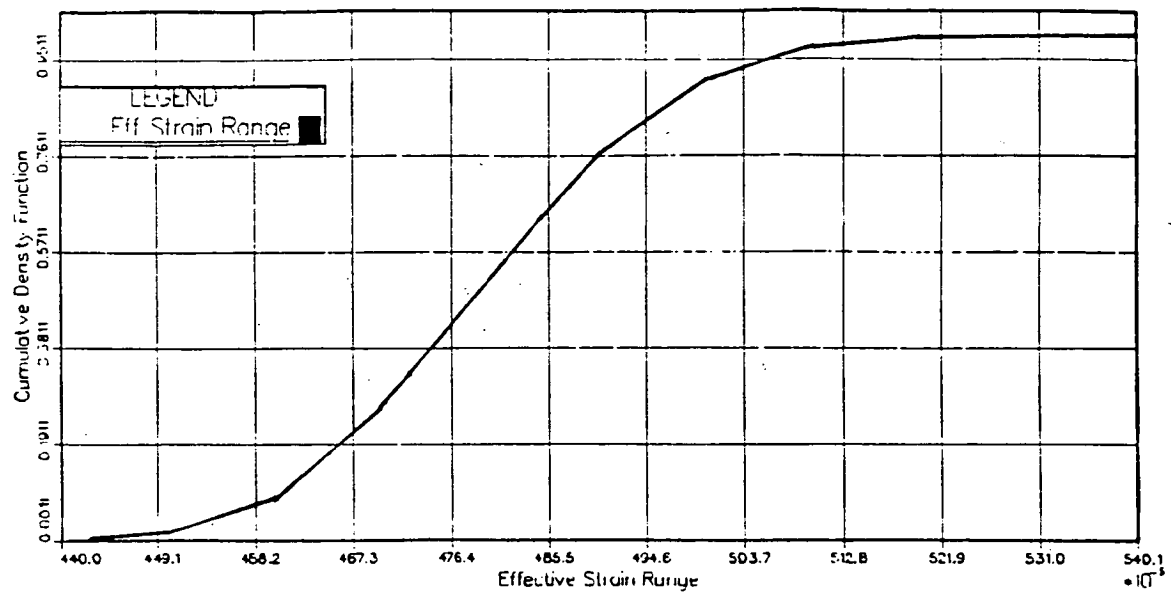


Figure 1.2.36: Cumulative density functions of the effective strain range of the LOX post at nodes 78 (top) and 84 (bottom) calculated using a Monte Carlo simulation with a quadratic response surface.

Node 117



Node 122

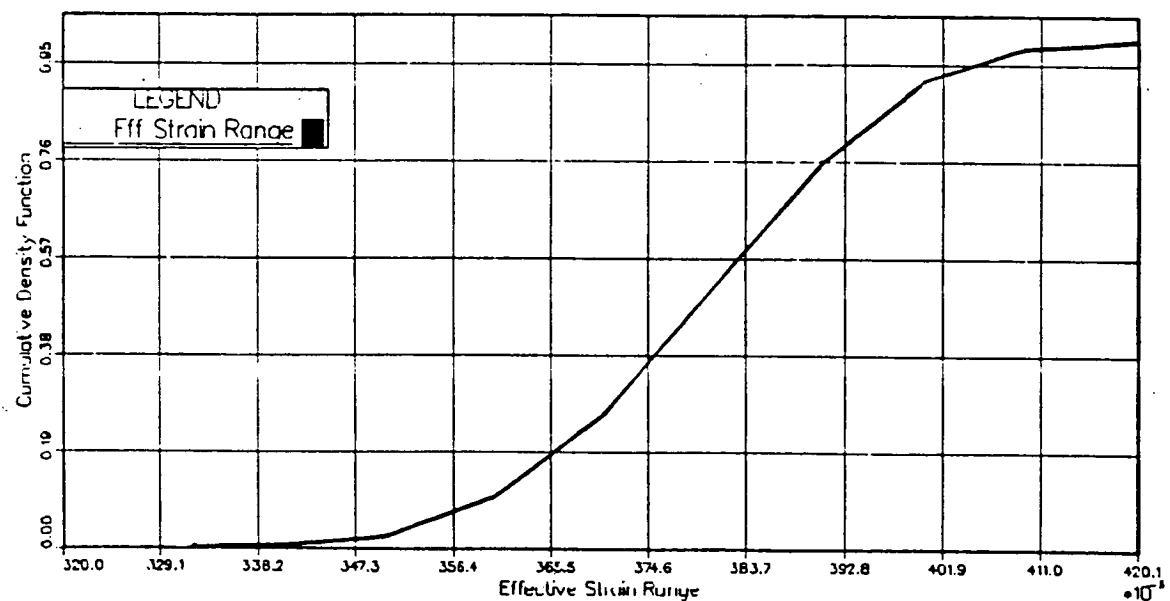
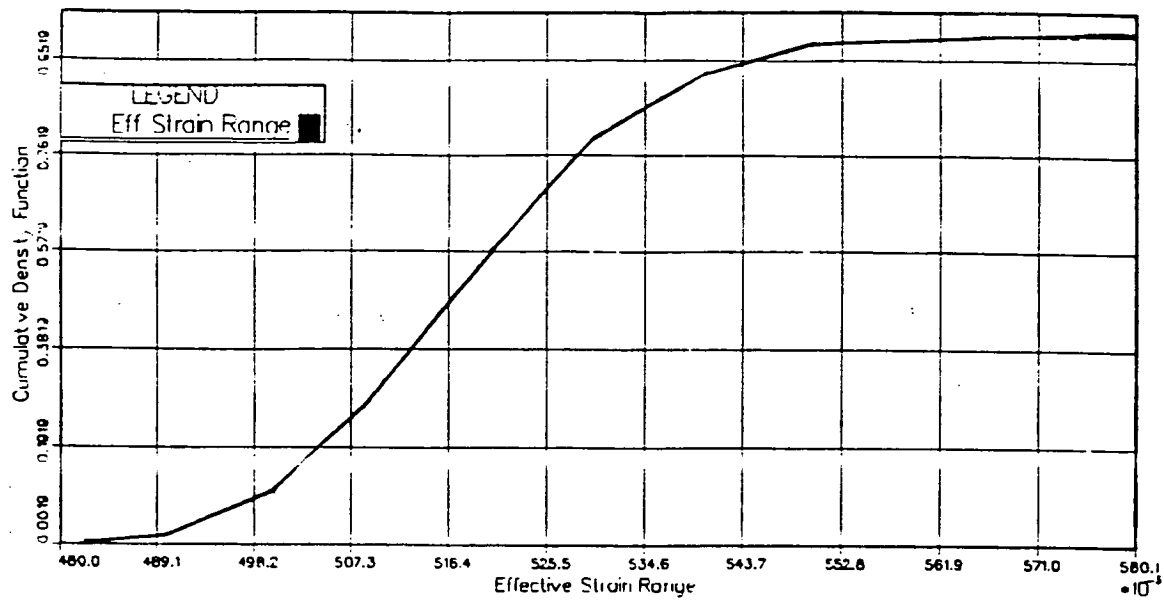


Figure 1.2.37: Cumulative density functions of the effective strain range of the LOX post at nodes 117 (top) and 122 (bottom) calculated using a Monte Carlo simulation with a quadratic response surface.

### Node 175



### Node 181

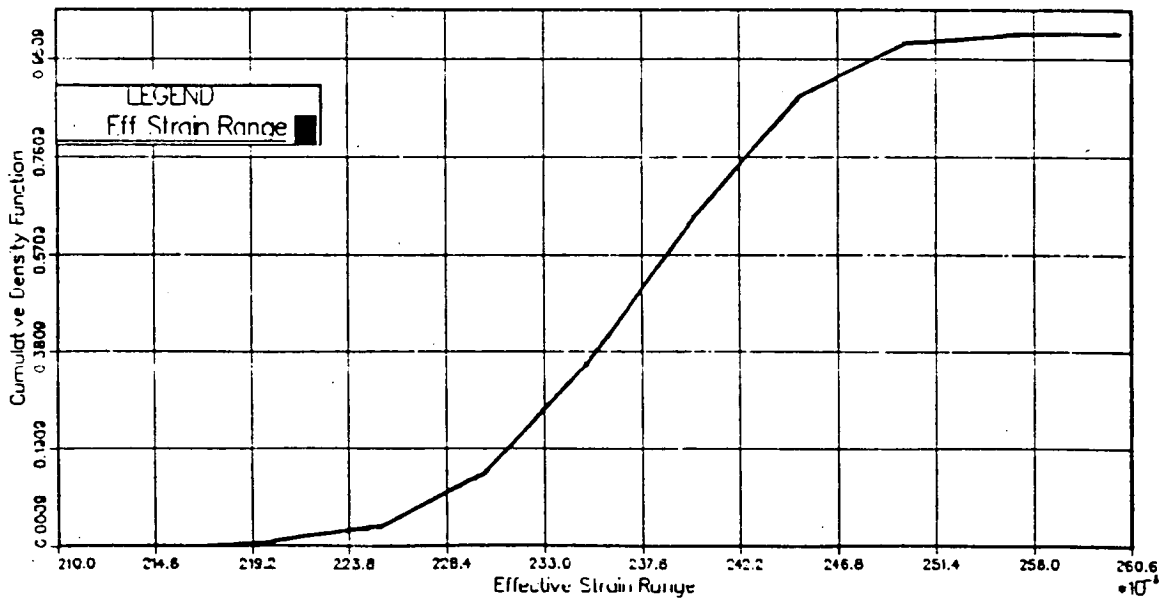


Figure 1.2.38: Cumulative density functions of the effective strain range of the LOX post at nodes 175 (top) and 181 (bottom) calculated using a Monte Carlo simulation with a quadratic response surface.

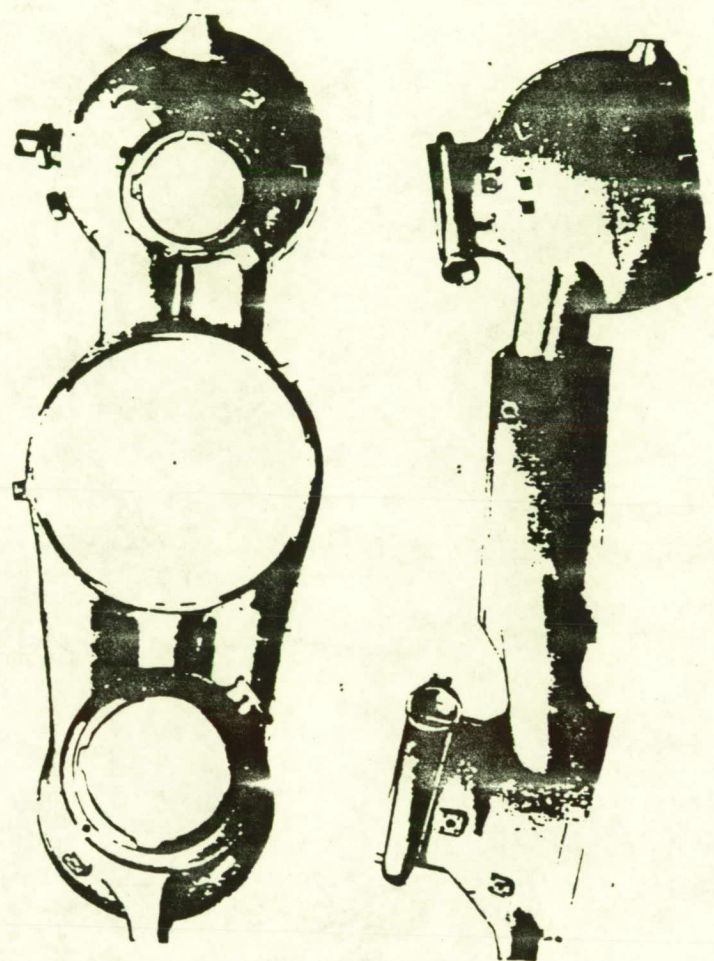


FIG. 1.3.1 SSME Hot Gas Manifold

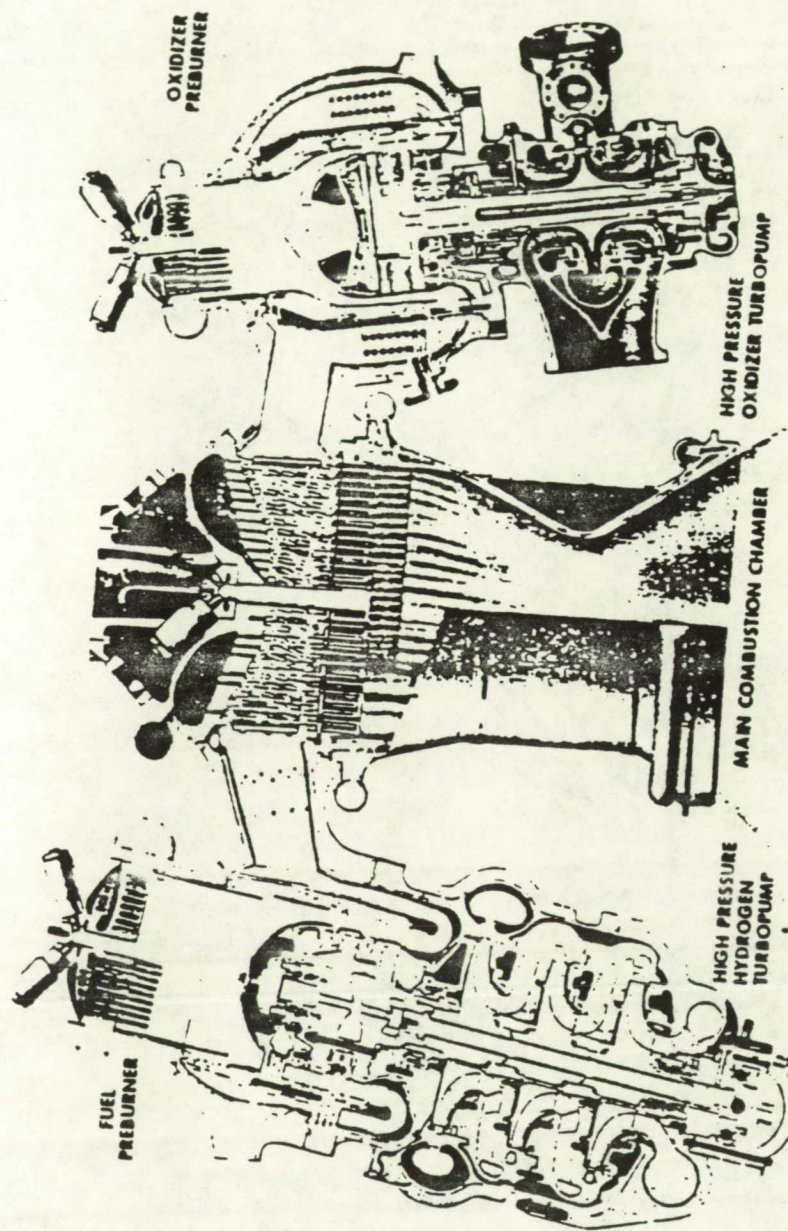
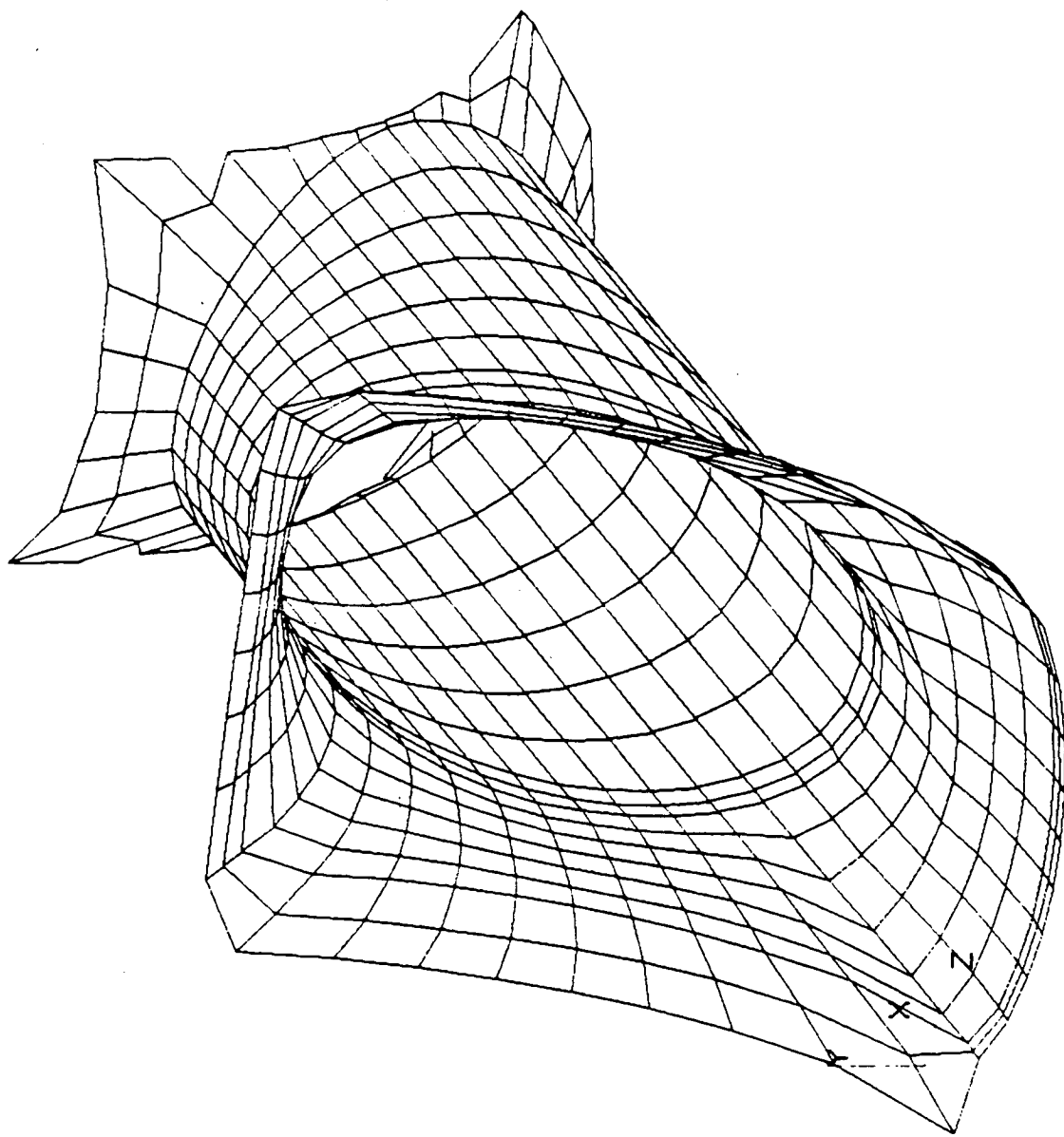


FIG. 1.3.2 SSME Powerhead Component Arrangement

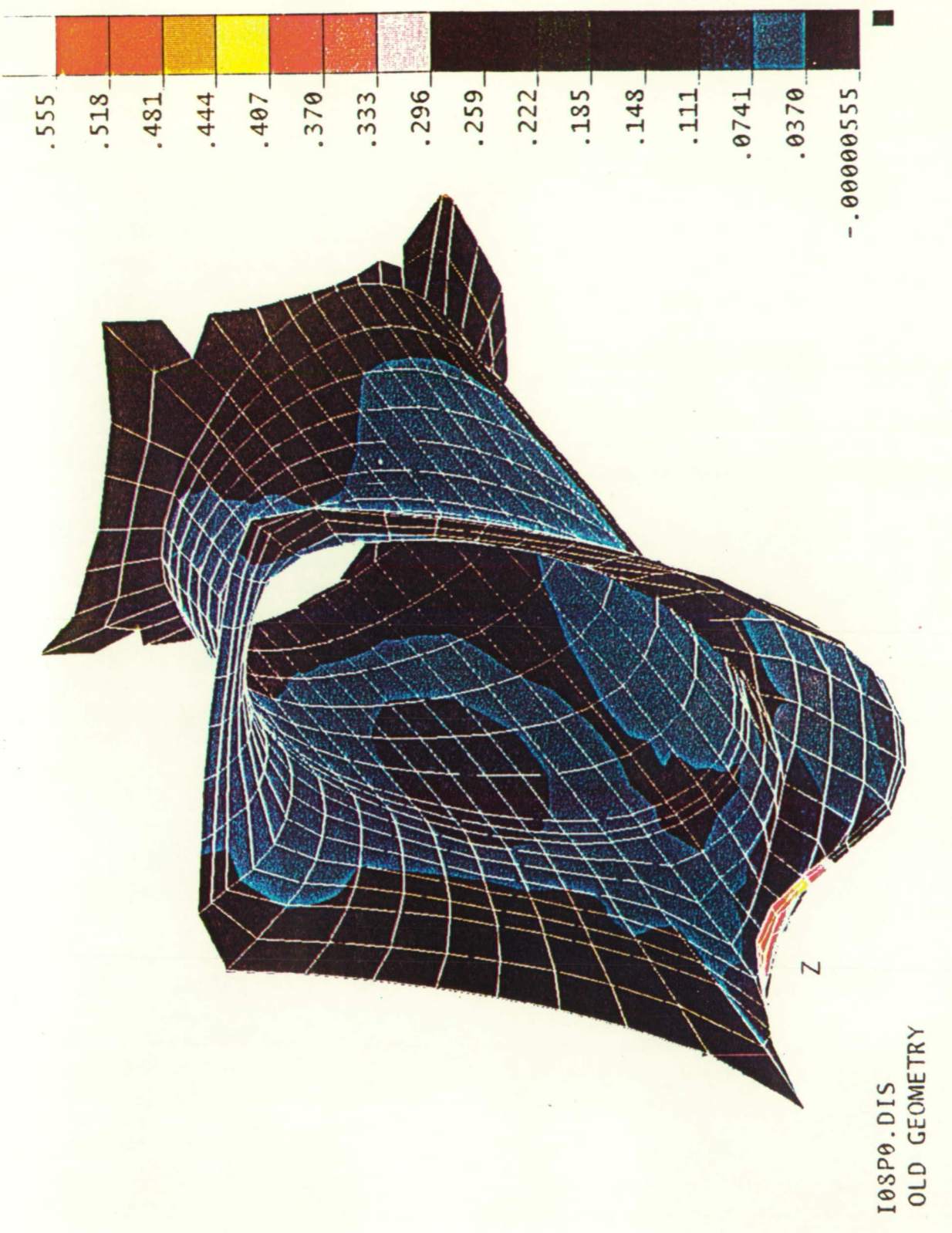
MODEL STATISTICS

Number of Active Nodes	6,70
Number of Duplicate Nodes	254
Maximum Node Number	1875
Number of Elements	652
Number of DOF	4020
Number of Boundary Conditions	511
Maximum Profile Height	4.25
Average Profile Height	2.86



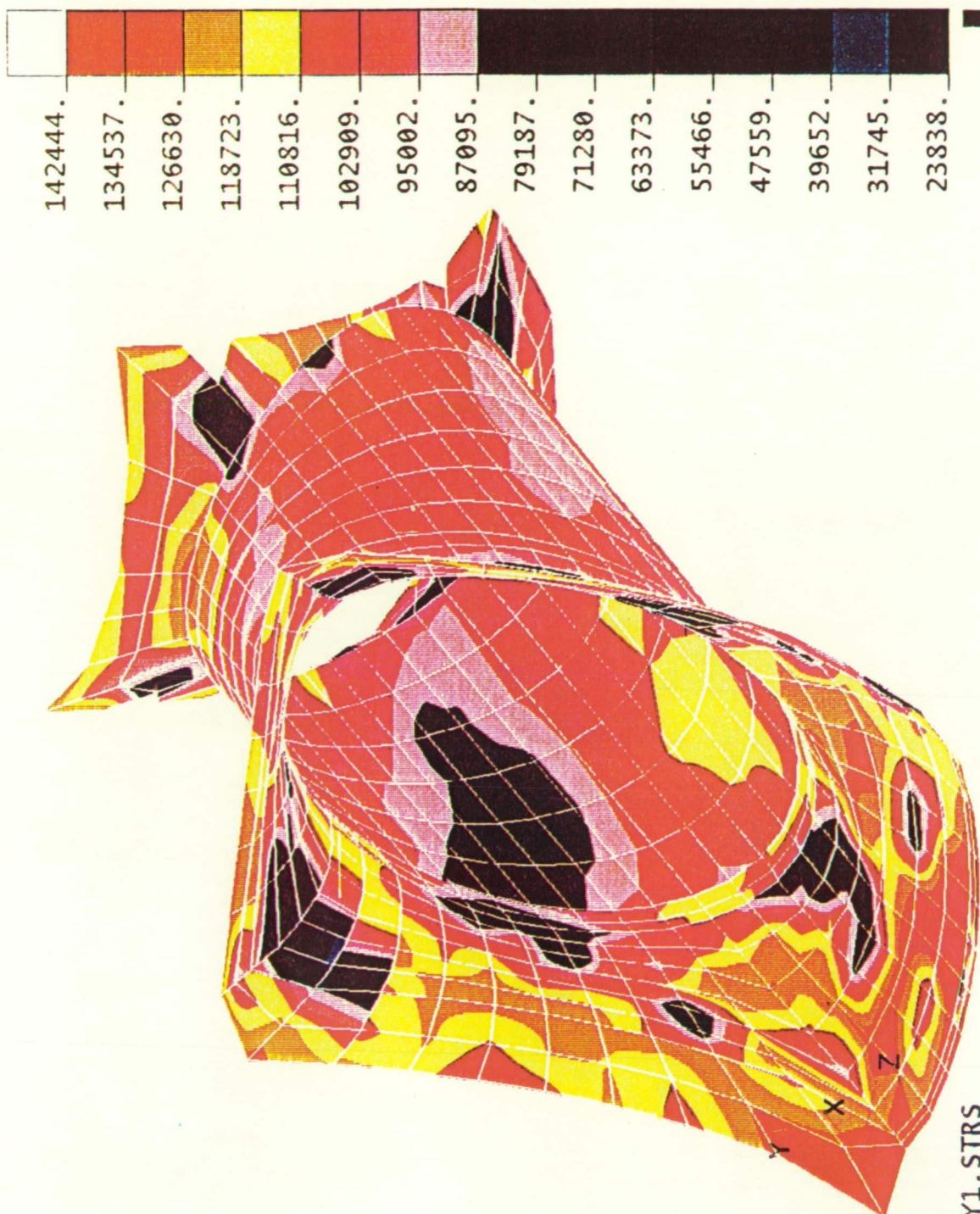
TRANSFER TUBE LINER - UNDEFORMED GEOMETRY

Fig. 1.3.3 NESSUS/FEM Model of the Structural Transfer Tube Liner



ORIGINAL PAGE  
COLOR PHOTOGRAPH

Fig. 1.3.4 Deformed Geometry of the Shell Near Collapse Load



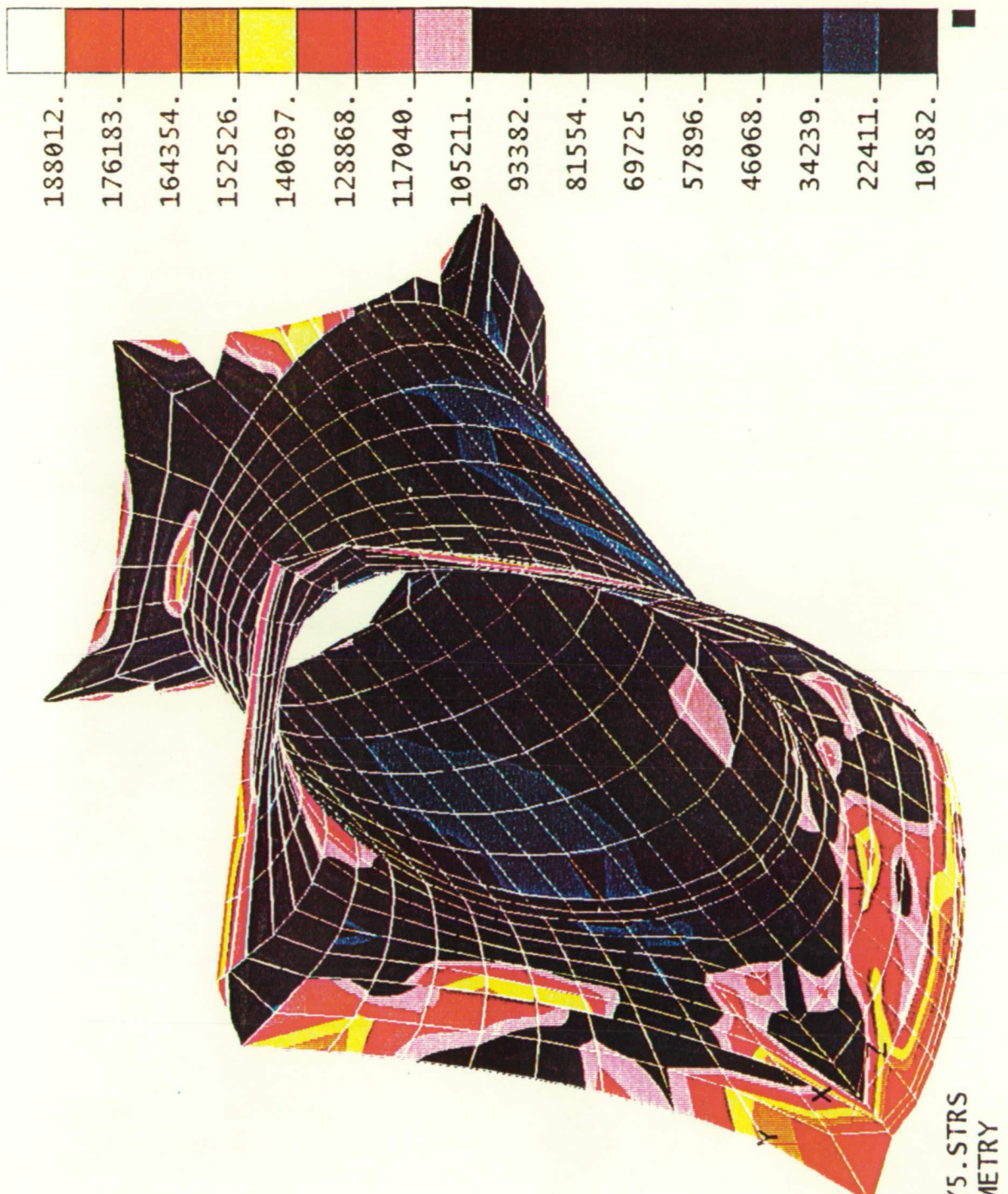
I08P0LAY1.STRS  
 OLD GEOMETRY

INNER FACE - EFFECTIVE STRESS

Fig. 1.3.5 Effective Stress Contours on the Inner Face Near Collapse Load



Fig. 1.3.6 Effective Strain Contours on the Inner Face Near Collapse Load



ORIGINAL PAGE  
COLOR PHOTOGRAPH

ORIGINAL PAGE IS  
OF POOR QUALITY

OUTER FACE - EFFECTIVE STRESS

Fig. 1.3.7 Effective Stress Contours on the Outer Face Near Collapse Load

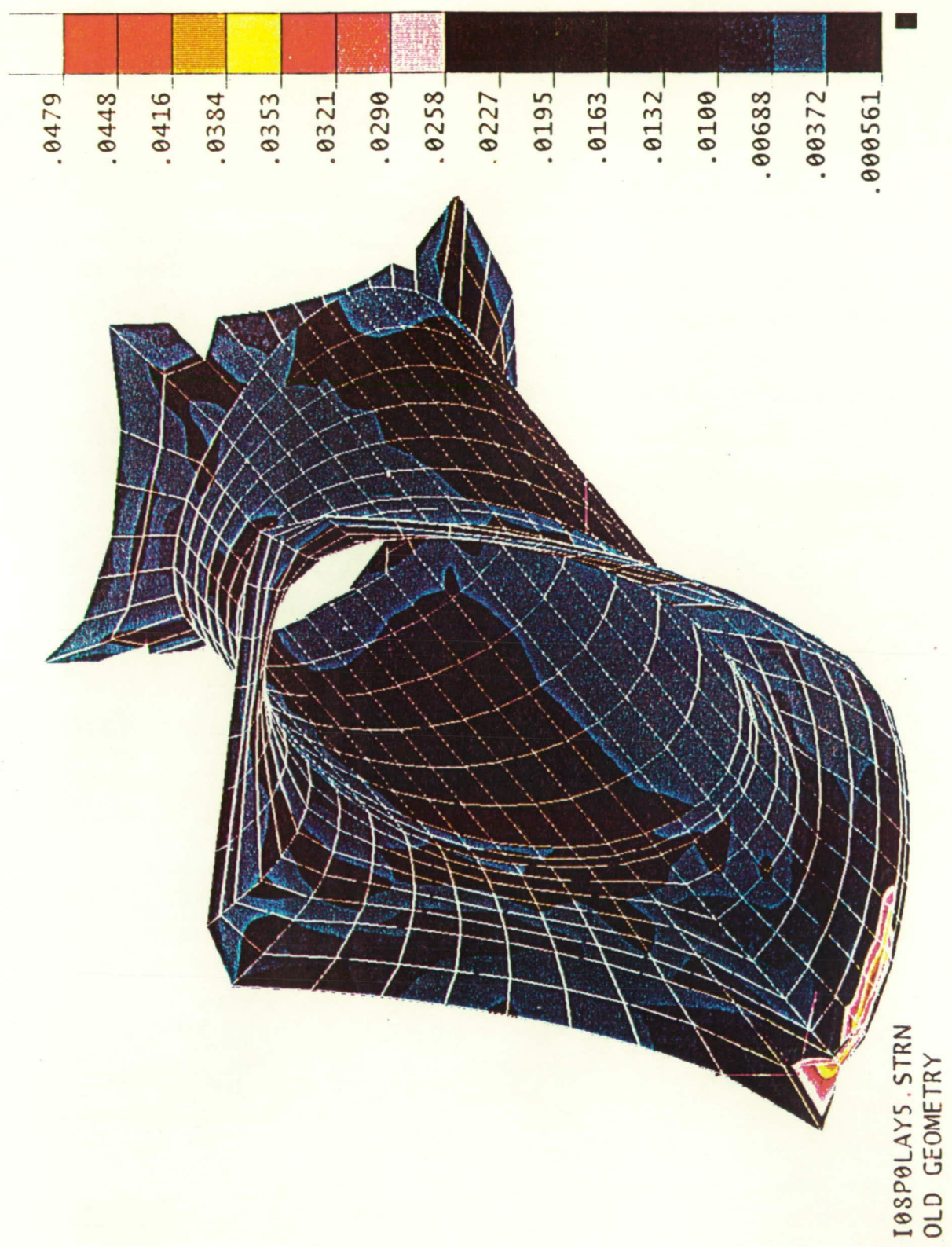
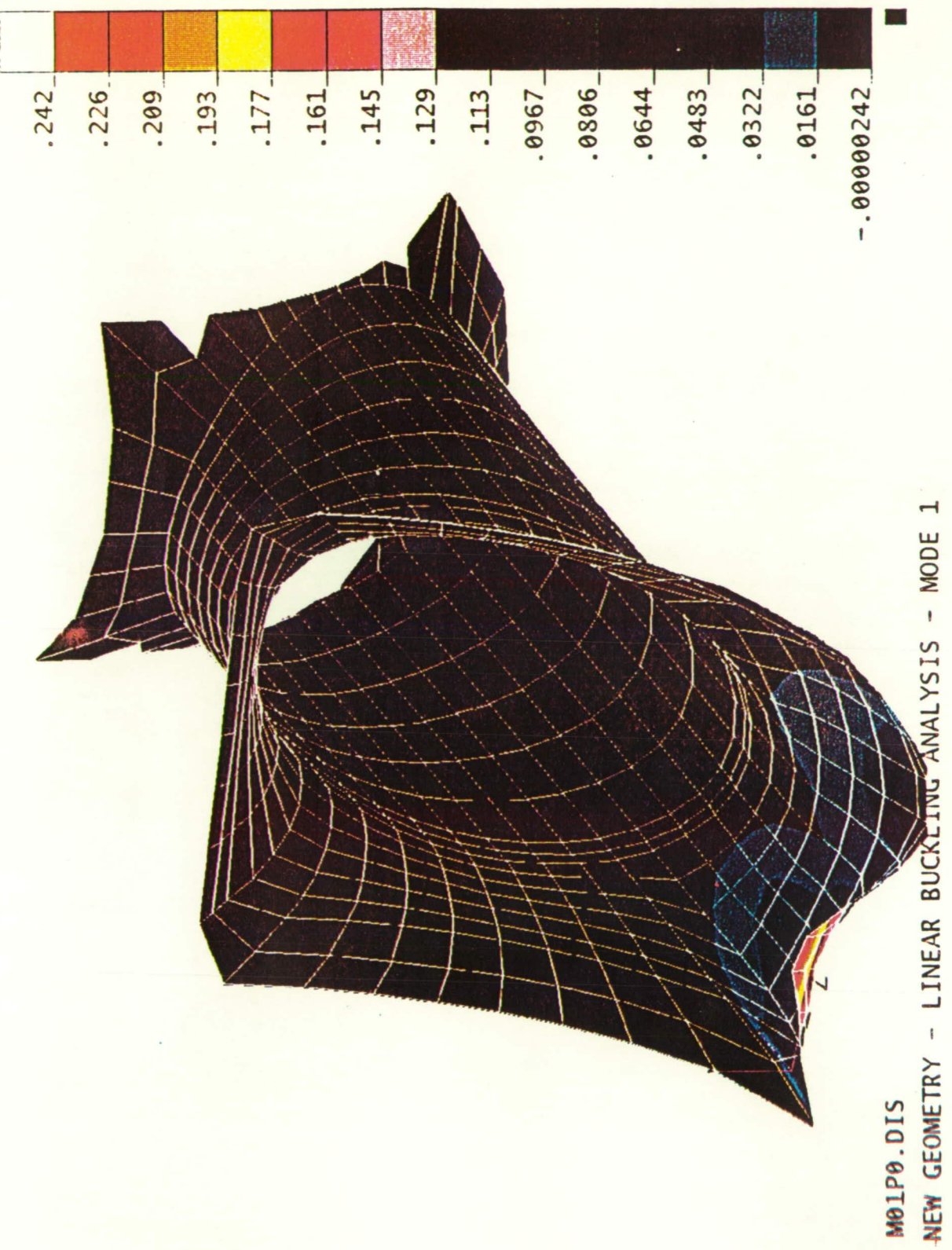
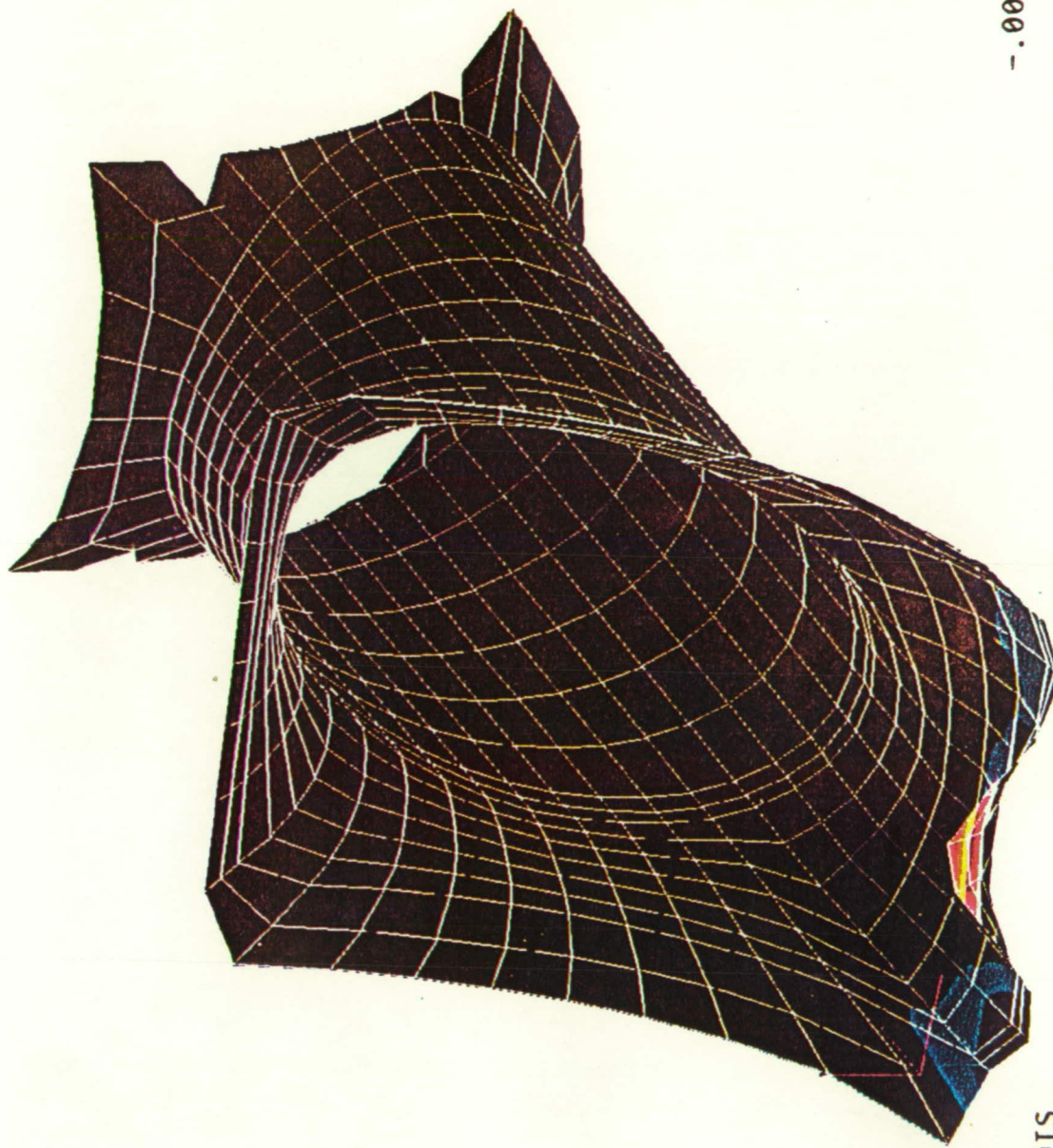
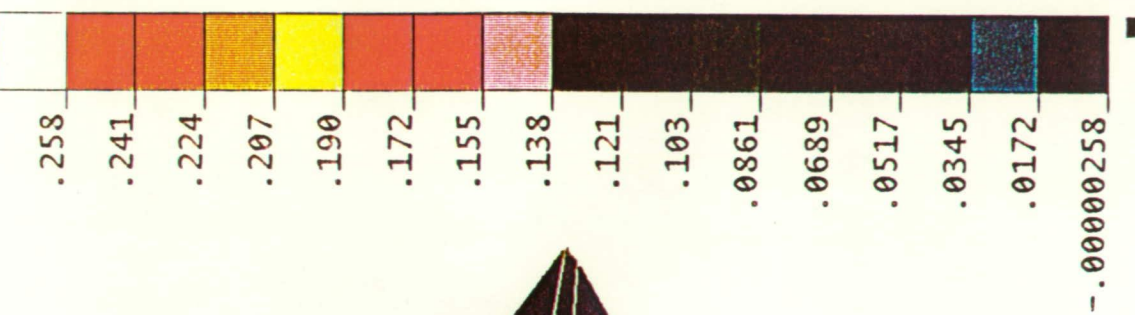


Fig. 1.3.8 Effective Strain Contours on the Outer Face Near Collapse Load



ORIGINAL PAGE  
COLOR PHOTOGRAPH

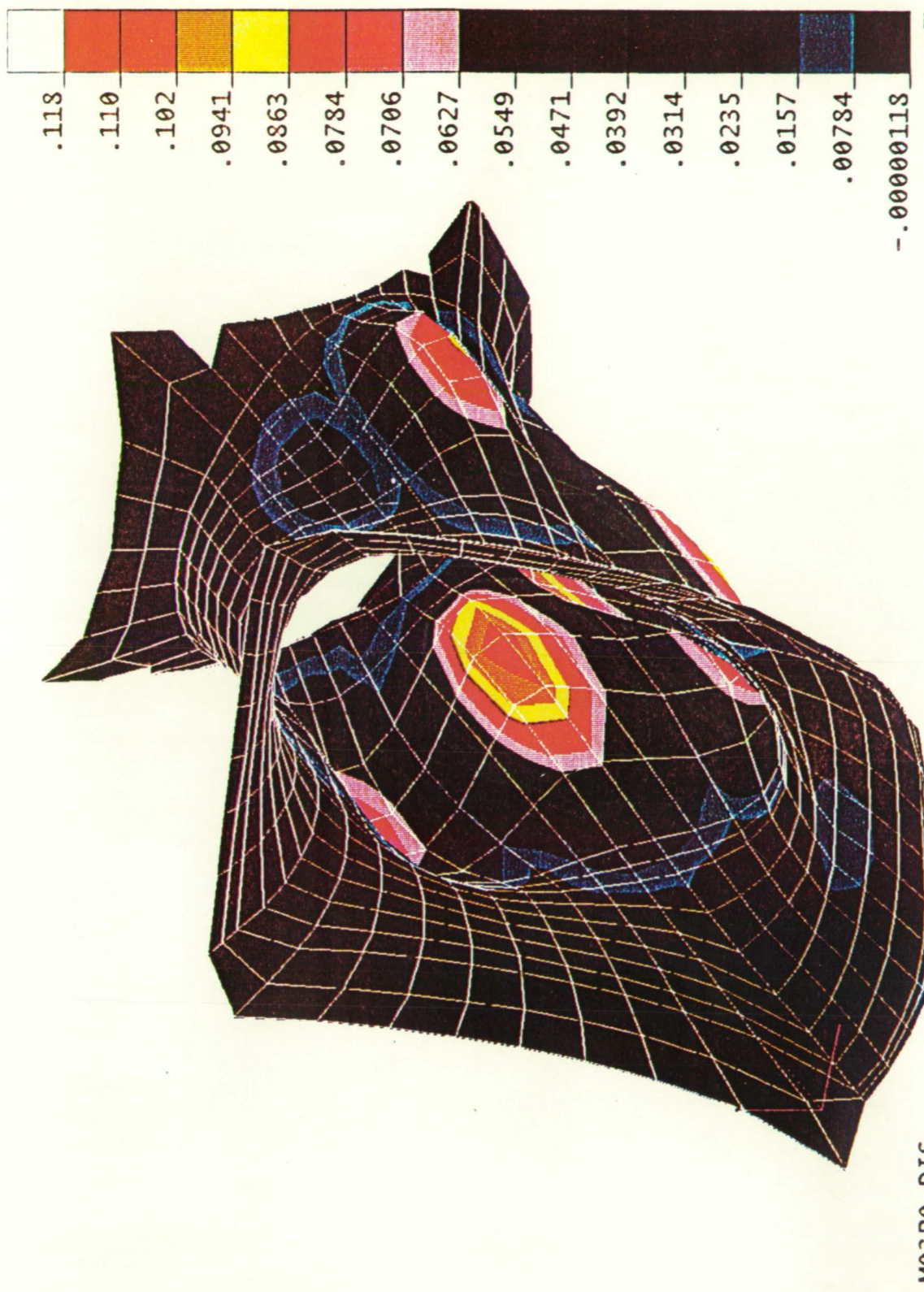
Fig. 1.3.9 First Buckling Mode of the Shell



M02P0.DIS

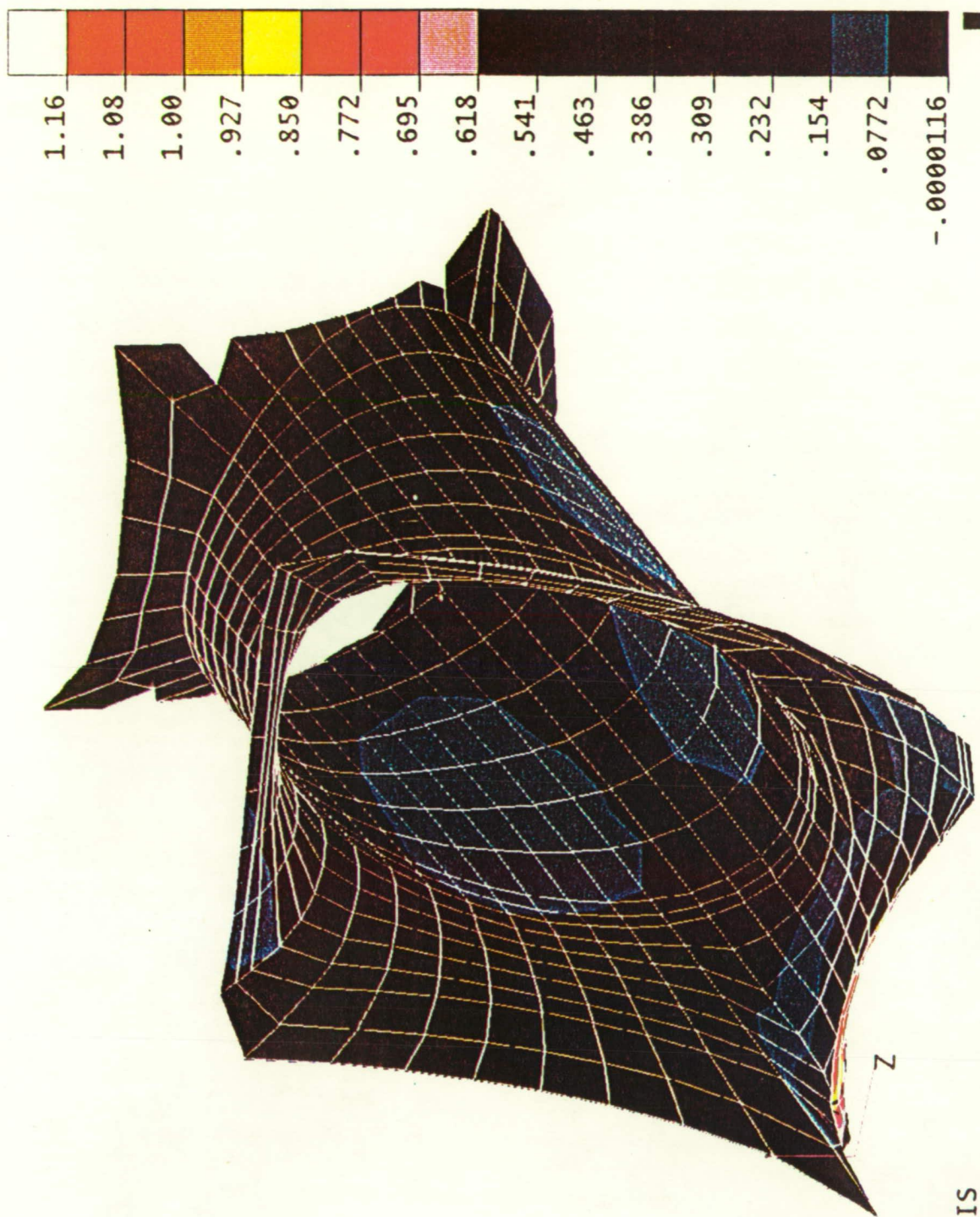
NEW GEOMETRY - LINEAR BUCKLING ANALYSIS - MODE 2

Fig. 1.3.10 Second Buckling Mode of the Shell



ORIGINAL PAGE  
COLOR PHOTOGRAPH

FIG. 1.3.11 Third Buckling Mode of the Shell

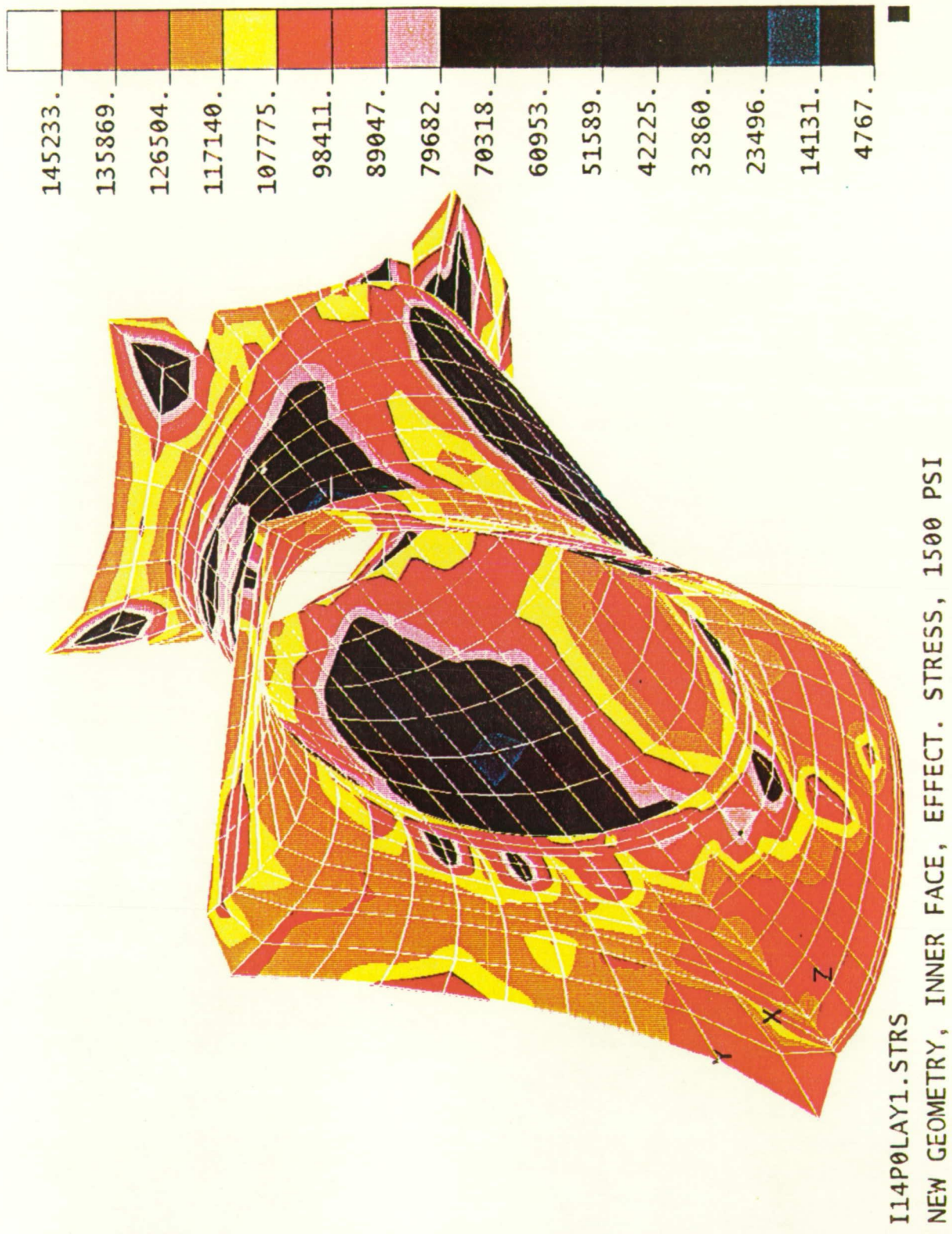


I14P0.DIS  
NEW GEOMETRY, TOTAL DISPLACEMENTS, DEFORMED PLOT, 1500 PSI

ORIGINAL PAGE  
COLOR PHOTOGRAPH

ORIGINAL PAGE IS  
OF POOR QUALITY

FIG. 1.3.12 Deformed State of the Shell Near Collapse Load



ORIGINAL PAGE  
COLOR PHOTOGRAPH

ORIGINAL PAGE IS  
OF POOR QUALITY

FIG. 1.3.13 Effective Stress on the Inner Face of the Shell Near Collapse Load

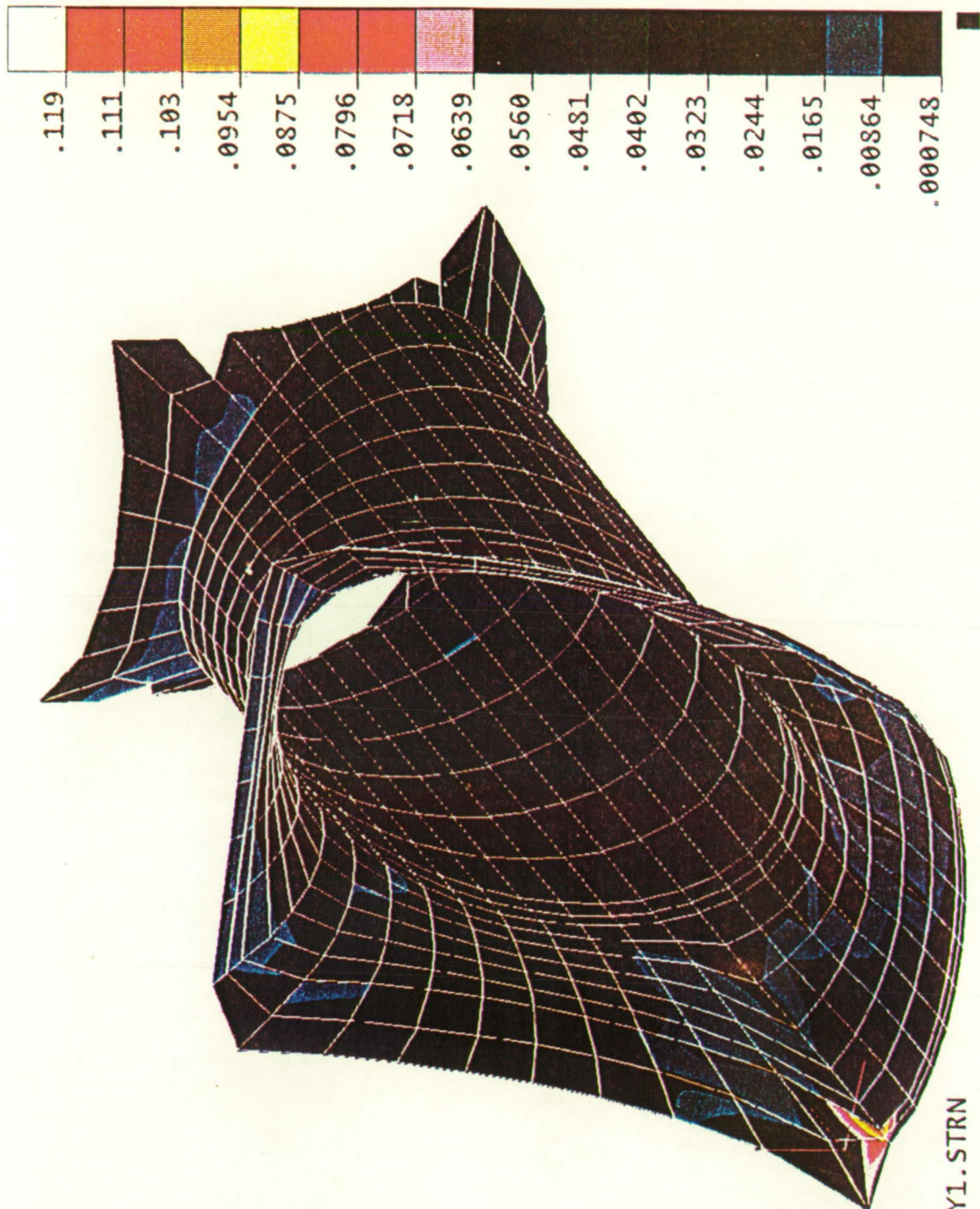


FIG. 1.3.14 Effective Strain on the Inner Surface Near Collapse Load



ORIGINAL PAGE  
COLOR PHOTOGRAPH

FIG. 1.3.15 Effective Stress on the Outer Surface Near Collapse Load

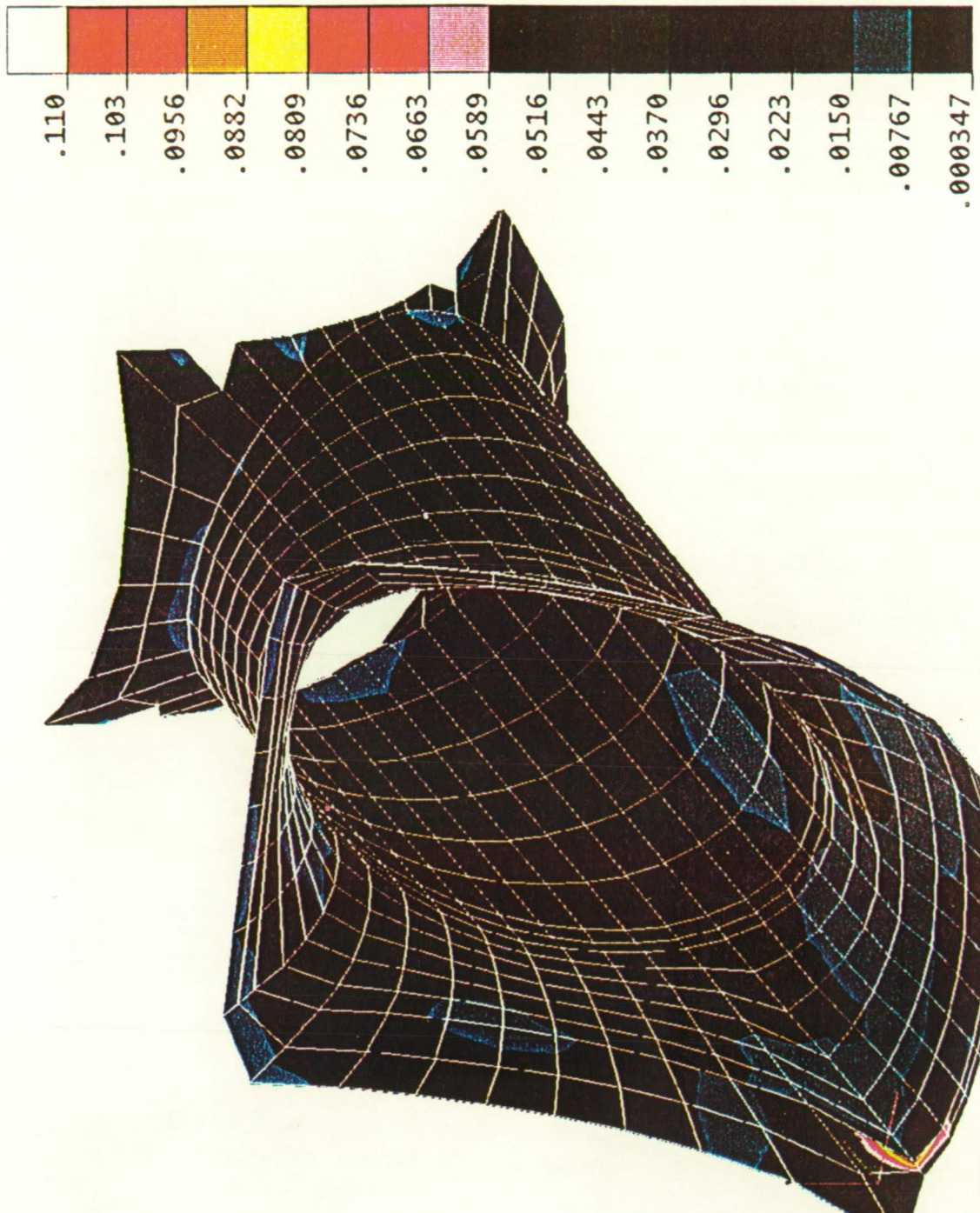


FIG. 1.3.16 Effective Strain on the Outer Surface Near Collapse Load

ORIGINAL PAGE  
COLOR PHOTOGRAPH

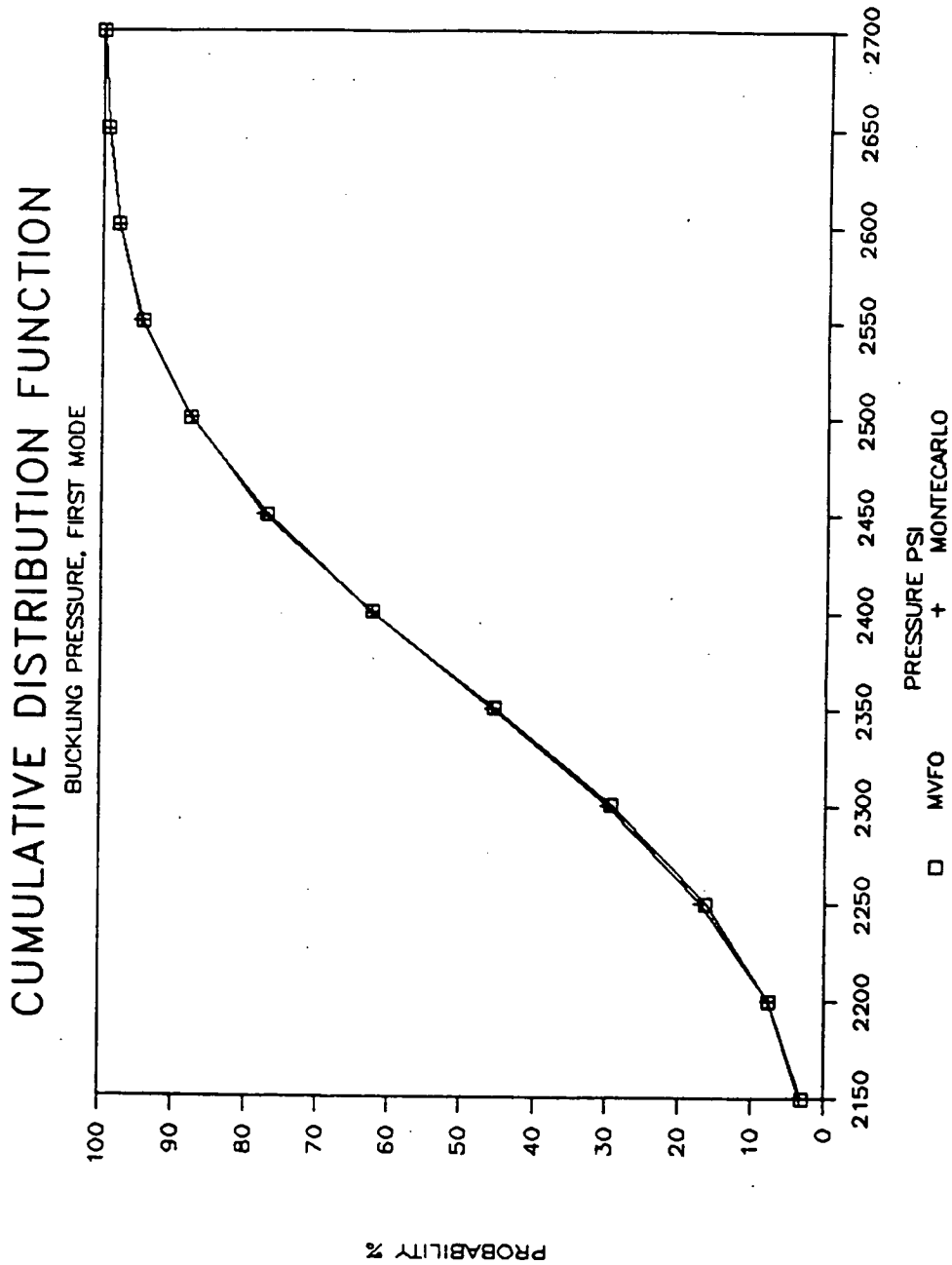


Fig. 1.3.17 CDF for the First Buckling Mode Pressure Obtained From NESSUS

# REPORT DOCUMENTATION PAGE

Form Approved  
OMB No. 0704-0188

Public reporting burden for this collection of information is estimated to average 1 hour per response, including the time for reviewing instructions, searching existing data sources, gathering and maintaining the data needed, and completing and reviewing the collection of information. Send comments regarding this burden estimate or any other aspect of this collection of information, including suggestions for reducing this burden, to Washington Headquarters Services, Directorate for Information Operations and Reports, 1215 Jefferson Davis Highway, Suite 1204, Arlington, VA 22202-4302, and to the Office of Management and Budget, Paperwork Reduction Project (0704-0188), Washington, DC 20503.

1. AGENCY USE ONLY (Leave blank)			2. REPORT DATE November 1991		3. REPORT TYPE AND DATES COVERED 5th Annual Contractor Report - Oct. 89		
4. TITLE AND SUBTITLE Probabilistic Structural Analysis Methods (PSAM) for Select Space Propulsion Systems Components (5th Annual Report)			5. FUNDING NUMBERS  WU-553-13-00 C-NAS3-24389				
6. AUTHOR(S)							
7. PERFORMING ORGANIZATION NAME(S) AND ADDRESS(ES)  Southwest Research Institute 6220 Culebra Road San Antonio, Texas 78228-0510			8. PERFORMING ORGANIZATION REPORT NUMBER  None				
9. SPONSORING/MONITORING AGENCY NAMES(S) AND ADDRESS(ES)  National Aeronautics and Space Administration Lewis Research Center Cleveland, Ohio 44135-3191			10. SPONSORING/MONITORING AGENCY REPORT NUMBER  NASA CR-187199				
11. SUPPLEMENTARY NOTES  Project Manager, C.C. Chamis, Structures Division, NASA Lewis Research Center, (216) 433-3252.							
12a. DISTRIBUTION/AVAILABILITY STATEMENT  Unclassified - Unlimited Subject Category 39				12b. DISTRIBUTION CODE			
13. ABSTRACT (Maximum 200 words)  This fifth annual report summarizes the technical effort and computer code developed during the five year duration of the program for probabilistic structural analysis methods. The summary includes (1) a brief description of the computer code manuals and (2) detailed description of code validation demonstration cases for random vibrations of a discharge duct, probabilistic material nonlinearities of a LOX post, and probabilistic buckling of a transfer tube liner.							
14. SUBJECT TERMS  Finite element; Random excitation; Probability spectra; Correlated; Uncorrelated; Damping; Accelerations; Harmonics; Shafts; Turbopumps; Ducts					15. NUMBER OF PAGES 94		
					16. PRICE CODE A05		
17. SECURITY CLASSIFICATION OF REPORT Unclassified		18. SECURITY CLASSIFICATION OF THIS PAGE Unclassified		19. SECURITY CLASSIFICATION OF ABSTRACT Unclassified		20. LIMITATION OF ABSTRACT	